

Development of Robust Multimodal Imaging Biomarkers of the Non-viable Tumour Component for Cancer Drug Development

*A thesis submitted to the University of Manchester for the degree of Master of
Philosophy in the Faculty of Medical and Human Sciences*

2013

Daniel Peter Burke

Centre for Imaging Sciences

School of Medicine

Contents

Chapter Number. Title of Chapter .. Page Number

1. Introduction .. 17

1.1 Measurement of the Non-Viable Cell Volume Fraction in Oncology .. 17

1.2 What are the components of the Extravascular Extracellular Space ? .. 18

1.3 Cell Death and the Extravascular Extracellular Space .. 22

1.3.1 Apoptosis .. 22

1.3.2 Necrosis .. 22

1.4 Where does “ v_e ” come from and what does it purport to measure ? .. 24

1.5 Non-MRI methods of measuring the Extravascular Extracellular Space .. 26

1.6 How can we model the Extravascular Extracellular Space ? .. 27

1.6.1 Pharmacokinetic Extravascular Extracellular Space ..27

1.6.1.1 Thermodynamic Confounds ..27

1.6.1.2 Mathematical Confounds ..27

1.6.1.3 Physiological Confounds .. 30

1.6.1.4 Imaging Confounds .. 30

1.6.2 Physiologic Extravascular Extracellular Space .. 30

1.7 Do “Shutter-Speed” Effects explain the disagreement between ADC and v_e ? .. 31

1.8 What scientific value exists in exploring the temporal evolution of v_e ? .. 32

1.9 Accurate modelling of the tumour microenvironment .. 34

1.10 Computational methods for determining a value for v_e from pharmacokinetic models .. 37

1.10.1 What can we consider to be physiologic parameter values and under what conditions are they produced ? .. 38

1.11 Diffusion MRI as a biomarker of the non-viable cell fraction .. 38

2. Validation of Experimental Methodology .. 40

2.1 Introduction .. 40

2.2 The Apparent Diffusion Coefficient (ADC) .. 41

2.2.1 Introduction .. 41

2.2.2 Materials and Methods .. 41

2.2.2.1 Stejskal-Tanner Diffusion Sensitised Spin Echo Pulse Sequence .. 42

2.2.2.2 Filling K Space in the Stejskal-Tanner Diffusion Sensitised Spin Echo Sequence .. 42

2.2.2.3 Temperature Dependence of Diffusion .. 43

2.2.2.4 Ice Water Phantom .. 43

2.2.2.5 Diffusion Sequence Details .. 44

2.2.2.6 Simulation of Diffusion Encoding Experiment .. 44

2.2.2.7 Bruker Scaling Factors .. 44

2.2.2.8 Experimental Protocol .. 44

2.2.2.9 Post processing of data .. 45

2.2.3 Results .. 46

2.2.3.1 Simulation of Diffusion Encoding Experiment .. 46

2.2.3.2 7T Phantom Data Compared to International Centres .. 47

2.2.3.3 Temperature Dependence of the Diffusion Coefficient of Water .. 48

2.2.4 Discussion .. 48

2.3 Measuring the Longitudinal Relaxation Time (T_1) .. 50

2.3.1 Introduction .. 50

2.3.2 Nuclear Spin Relaxation Mechanisms .. 52

2.3.3 Materials and Methods ..	55
2.3.3.1 PRESS Sequence Details ..	55
2.3.3.2 K Space Filling for the PRESS Sequence ..	55
2.3.3.3 Simulation of Saturation Recovery Curve for Spectroscopic Saturation Recovery Experiment ..	55
2.3.3.4 PRESS Saturation Recovery Experiment 1 ..	55
2.3.3.5 Saturation Recovery Imaging Sequence ..	55
2.3.3.6 Stimulated Echoes in a CPMG Sequence ..	57
2.3.3.7 K Space Filling for the RARE-VTR Sequence ..	57
2.3.3.8 Simulation of Saturation Recovery Curve for Imaging Saturation Recovery Experiment ..	58
2.3.3.9 RARE-VTR Experiment 1 ..	58
2.3.3.10 RARE-VTR Experiment 2 ..	58
2.3.3.11 FLASH (Fast Low Angle Shot)Imaging Sequence ..	58
2.3.3.12 K Space Filling for the FLASH Sequence ..	60
2.3.3.13 FLASH Experiment 1 ..	60
2.3.3.14 FLASH Experiment 2 ..	61
2.3.3.15 Calculating Contrast Agent Concentration ..	61
2.3.3.16 Combination of Errors ..	61
2.3.3.17 Additional Sources of Error ..	62
2.3.4 Results ..	63
2.3.4.1 PRESS Spectroscopic Saturation Recovery Simulation ..	63
2.3.4.2 PRESS Spectroscopic Saturation Recovery Experiment 1 ..	63
2.3.4.3 Bland-Altman Analysis ..	64
2.3.4.4 RARE-VTR Saturation Recovery Simulation ..	66

2.3.4.5 RARE-VTR Saturation Recovery Experiment 1 .. 67

2.3.4.6 Bland-Altman Analysis .. 68

2.3.4.7 RARE-VTR Experiment 2 .. 69

2.3.4.8 FLASH Variable Flip Angle Experiment 1 .. 70

2.3.4.9 FLASH Variable Flip Angle Experiment 2 .. 70

2.3.4.10 Bland-Altman Analysis .. 71

2.3.4.11 Validation of Imaging Sequences Table .. 72

2.3.4.12 Validation of Imaging Sequences Graph .. 74

2.3.5 Discussion .. 75

2.4 Inductively Coupled Plasma Mass Spectrometry (ICP-MS) .. 76

2.4.1 Introduction .. 76

2.4.2 Materials and Methods .. 76

2.4.2.1 Experimental Protocol .. 76

2.4.2.2 Calculation of Gadolinium in Whole Tumour Volume .. 76

2.4.3 Results .. 78

2.4.4 Discussion .. 78

3. The Effect of Radiotherapy upon the Apparent Diffusion Coefficient in a Preclinical Cancer Model .. 79

3.1 Introduction .. 79

3.1.1 Experimental Hypothesis .. 79

3.2 Materials and Methods .. 80

3.2.1 Study Design .. 80

3.2.2 Image Acquisition and Analysis .. 80

3.2.3 Animal Monitoring and Setup .. 80

3.2.4 Histological Analysis .. 81

3.2.5 Statistical Analysis .. 82

3.3 Results .. 84

3.3.1 Fictitious Threshold .. 84

3.3.2 Summary Table .. 84

3.3.2.1 ADC Maps .. 84

3.3.2.2 Fictitious Threshold Analysis .. 85

3.3.3 Regression Analysis .. 85

3.3.4 Histological Analysis .. 86

3.3.4.1 Quantification of the Percentage Necrosis .. 86

3.3.4.2 Quantification of the Percentage Apoptosis .. 86

3.3.4.3 Quantification of the Perfused and Total Vessel Densities .. 87

3.3.5 Results of Histopathology and Histochemical Analysis .. 88

3.3.5.1 Percentage Necrosis .. 88

3.3.5.1.1 Statistical Analysis for the Percentage Necrosis .. 88

3.3.5.2 Percentage Apoptosis .. 89

3.3.5.2.1 Statistical Analysis for the Percentage Apoptosis .. 89

3.3.5.3 Total Vessel Density .. 90

3.3.5.3.1 Statistical Analysis for the Total Vessel Density .. 90

3.3.5.4 Perfused Vessel Density .. 91

3.3.5.4.1 Statistical Analysis for the Perfused Vessel Density .. 91

3.3.6 Discussion .. 92

4. The Effect of 5-FU chemotherapy upon the Apparent Diffusion Coefficient in a Preclinical Cancer Model .. 94

4.1 Introduction .. 94

4.1.1 Experimental Hypothesis .. 94

4.2 Materials and Methods .. 94

4.2.1 Study Design .. 94

4.2.2. Imaging Acquisition and Data Analysis .. 94

4.2.3 Animal Monitoring and Setup .. 95

4.2.4 Histological Analysis .. 95

4.2.5 Statistical Analysis .. 95

4.3 Results .. 96

4.3.1 ADC Results .. 96

4.3.1.1 Summary Table of Results .. 96

4.3.1.2 ADC Maps .. 97

4.3.2 Histological Results .. 98

4.3.2.1 Percentage Necrosis .. 98

4.3.2.1.1 Statistical Analysis for the Percentage Necrosis .. 98

4.3.2.2 Percentage Apoptosis .. 99

4.3.2.2.1 Statistical Analysis for the Percentage Apoptosis .. 99

4.3.3 Statistical Results .. 100

4.4 Discussion .. 101

5.Future Work .. 103

5.1 Mapping of the B1 field .. 103

5.2 Probabilistic Model for DCE-MRI data analysis .. 103

6. Bibliography .. 104

List of Tables

Table Number. Table Description – Chapter .. Page

Table 1. Degrees of freedom in pharmacokinetic models - Chapter 1.4 .. 25

Table 2. R_1 values of phantoms obtained with PRESS sequence - Chapter 2.3.4.2 .. 64

Table 3. R_1 values of phantoms obtained with RARE-VTR sequence - Chapter 2.3.4.5 .. 67

Table 4. R_1 values of phantoms obtained with FLASH sequence - Chapter 2.3.4.9 .. 70

Table 5. Validation of imaging sequences table - Chapter 2.3.4.11 .. 73

Table 6. Summary table of results for radiotherapy study - Chapter 3.3.2 .. 84

Table 7. Table of results from regression analysis - Chapter 3.3.3 .. 85

Table 8. Table of results for percentage necrosis - Chapter 3.3.5.1 .. 88

Table 9. Table of results for percentage apoptosis - Chapter 3.3.5.2 .. 89

Table 10. Table of results for total vessel density - Chapter 3.3.5.3 .. 90

Table 11. Table of results for perfused vessel density - Chapter 3.3.5.4 .. 91

Table 12. Table of ADC results for chemotherapy study - Chapter 4.3.1 .. 96

Table 13. Summar table of results - Chapter 4.3.1.1 .. 96

Table 14. Table of results for percentage necrosis - Chapter 4.3.2.1 .. 98

Table 15. Table of results for percentage apoptosis - Chapter 4.3.2.2 . 99

Table 16. Pearson's rho correlation between ADC change and histopathology - Chapter 4.3.3 .. 100

List of Figures

Figure Number. Figure description – Chapter .. Page

Figure 1. The tumour microenvironment - Chapter 1.2 .. 19

Figure 2. The extracellular matrix - Chapter 1.2 .. 20

Figure 3. The necrotic and apoptotic cell death pathways - Chapter 1.3.2 .. 23

Figure 4. Arterial input function taken from the literature - Chapter 1.8 .. 33

Figure 5. Impulse response function with literature values for v_e and K_{trans} - Chapter 1.8 .. 33

Figure 6. Contrast agent in tissue over a time period of 6000 seconds - Chapter 1.8 .. 33

Figure 7. Contrast agent in tissue over a time period of 600 seconds - Chapter 1.8 .. 34

Figure 8. Arterial input function taken from the literature - Chapter 1.9 .. 35

Figure 9. Impulse response function for constant K_{trans} and variable v_e - Chapter 1.9 .. 36

Figure 10. Tissue concentration time curve for constant K_{trans} and variable v_e - Chapter 1.9 .. 36

Figure 11. Tissue concentration time curve for constant v_e and variable K_{trans} - Chapter 1.9 .. 37

Figure 12. Stejskal-Tanner diffusion-weighted spin echo pulse sequence diagram - Chapter 2.2.2.1 .. 42

Figure 13. K Space Filling for the Stejskal-Tanner diffusion-weighted spin echo pulse sequence -
Chapter 2.2.2.2 .. 42

Figure 14. Ice water phantom schematic diagram - Chapter 2.2.2.4 .. 43

Figure 15. Linear fit with three b values to obtain ADC - Chapter 2.2.3.1 .. 46

Figure 16. Non-linear fit with three b values to obtain ADC - Chapter 2.2.3.1 .. 46

Figure 17. ADC values from ice water phantom experiment on a 7T Bruker preclinical scanner -
Chapter 2.2.3.1 .. 47

Figure 18. ADC values from 7T Bruker preclinical scanner compared to international centres - Chapter
2.2.3.2 .. 47

Figure 19. Temperature dependence of the diffusion coefficient of water - Chapter 2.2.3.3 .. 48

Figure 20. Interaction between paramagnetic complex and water protons - Chapter 2.3.2 .. 53

Figure 21. Pulse sequence diagram for PRESS sequence - Chapter 2.3.3.1 .. 55

Figure 22. Pulse sequence diagram for the RARE-VTR sequence - Chapter 2.3.3.5 .. 56

Figure 23. K space filling in the RARE-VTR sequence - Chapter 2.3.3.7 .. 57

Figure 24. Pulse sequence diagram for the FLASH sequence - Chapter 2.3.3.11 .. 60

Figure 25. K space filling in the FLASH sequence - Chapter 2.3.3.12 .. 60

Figure 26. Simulation of saturation recovery experiment for a T_1 of 1 sec - Chapter 2.3.4.1 .. 63

Figure 27. Saturation recovery experiment for a phantom doped to a T_1 of approximately 1 sec - Chapter 2.3.4.2 .. 63

Figure 28. Bland-Altman analysis of the PRESS measurements made before and after two RARE-VTR experiments - Chapter 2.3.4.3 .. 64

Figure 29. Bland-Altman analysis of the PRESS measurements after two RARE-VTR experiments against second RARE-VTR experiment -Chapter 2.3.4.3 .. 65

Figure 30. Bland-Altman analysis of PRESS against FLASH - Chapter 2.3.4.3 .. 65

Figure 31. Bland-Altman analysis of PRESS against dynamic FLASH - Chapter 2.3.4.3 .. 66

Figure 32. Simulation of saturation recovery experiment with four TR's assuming a T_1 of 1 sec - Chapter 2.3.4.4 .. 66

Figure 33. RARE-VTR saturation recovery experiment on a phantom with a T_1 of approximately 1 sec - Chapter 2.3.4.5 .. 67

Figure 34. Bland-Altman of RARE-VTR against FLASH - Chapter 2.3.4.6 .. 68

Figure 35. Bland-Altman of RARE-VTR against dynamic FLASH - Chapter 2.3.4.6 .. 68

Figure 36. RARE-VTR 15 repetitions for a phantom doped to a T_1 of approximately 1 sec - Chapter 2.3.4.7 .. 69

Figure 37. Simulation of FLASH signal intensity as a function of time for a TR of 6.7msec and a T_1 of 1 sec - Chapter 2.3.4.8 .. 70

Figure 38. Bland-Altman of FLASH against Dynamic FLASH - Chapter 2.3.4.10 .. 71

Figure 39. Measurement of T_1 using four phantoms and four sequences - Chapter 2.3.4.12 .. 74

Figure 40. ADC maps for control and treated groups at 1 hour pre and 72 hours post radiotherapy - Chapter 3.3.2.1 .. 84

Figure 41. Threshold analysis applied to ADC maps shown in figure 52 - Chapter 3.3.2.2 .. 85

Figure 42. H&E stained tissue section with viable and non-viable areas indicated - Chapter 3.3.4.1 .. 86

Figure 43. DAPI stained section - Chapter 3.3.4.2 .. 87

Figure 44. TUNEL stained section - Chapter 3.3.4.2 .. 87

Figure 45. CD31 stained section - Chapter 3.3.4.3 .. 87

Figure 46. Hoechst 3342 stained section - Chapter 3.3.4.3 .. 87

Figure 47. ADC maps for median animals from treated and control groups at 1 hour pre and 72 hours post chemotherapy - Chapter 4.3.1.2 .. 97

Abstract

This project was initiated with the objective of obtaining a magnetic resonance imaging (MRI) derived measure of the non-viable cell fraction of a tumour. The word “biomarker” pervades much of the quantitative imaging literature. There exist a variety of imaging parameters which purport to convey information about the underlying pathophysiology. These are generically labelled as “biomarkers”, although a review of the literature indicates that there is little, (or often contradictory) evidence to support this assertion. Indeed, the absence of robust validation is in evidence across the broad spectrum of imaging modalities. As the development of novel chemotherapeutic agents progresses from in vitro studies performed in a Petri dish to in vivo animal experiments, treatment efficacy can be gauged by a number of methods, one of which is imaging. Translational imaging offers the opportunity of developing and validating imaging techniques in the preclinical setting, with potential for their adoption into a clinical trial. The Apparent Diffusion Coefficient (ADC) of water proton spins has emerged as a potential “biomarker” of cell death.

Two studies were performed to investigate the relationship between ADC and the pathophysiologic changes occurring subsequent to radiotherapy or chemotherapy in preclinical cancer models. Dynamic contrast enhanced magnetic resonance imaging (DCE-MRI) is purported to offer a means of quantifying the non-viable cell fraction through the pharmacokinetic parameter “ v_e ”, the extravascular extracellular space volume per unit volume of tissue. Performing a DCE-MRI experiment requires measurements of T_1 before and after the administration of a contrast agent.

To this end, methods development undertaken included extensive validation experiments to determine the accuracy and reproducibility of the T_1 relaxation time for use in a DCE-MRI study. Validation of ADC measurements was performed through the use of a novel ice water phantom designed for a narrow bore preclinical MRI scanner. A means of determining the quantity of contrast agent within a tumour can be performed through the use of ICP-MS (Inductively Coupled Plasma Mass Spectrometry). A validation experiment was performed through the preparation of a phantom of known quantity of contrast agent and comparison against that returned from ICP-MS analysis. This thesis contends that the development of an MRI derived measure of the non-viable cell fraction does not appear viable within the framework of the present pharmacokinetic models and imaging hardware available. The literature fails to address significant confounds in the scientific method, indeed this is in evidence in the variability of observed imaging parameters.

Institution : The University of Manchester

Candidate : Daniel Peter Burke

Degree Title : Master of Philosophy

Thesis Title : Development of Robust Multimodal Imaging Biomarkers of the Non-viable Tumour Component for Cancer Drug Development

Date : June 2013

Declaration

No portion of the work referred to in the thesis has been submitted in support of an application for another degree or qualification of this or any other university or institute of learning.

Copyright Statement

1. The author of this thesis (including any appendices and/or schedules to this thesis) owns certain copyright or related rights in it (the “Copyright”) and s/he has given the University of Manchester certain rights to use such Copyright, including for administrative purposes.
2. Copies of this thesis either in full or in extracts and whether in hard or electronic copy, may be made **only** in accordance with Copyright, Designs and Patents Act 1988 (as amended) and regulations issued under it or, where appropriate, in accordance with licensing agreements with the University has from time to time. This page must form part of any such copies made.
3. The ownership of certain Copyrights, patents, designs, trade marks and other intellectual property (the “Intellectual Property”) and any reproductions of copyright works in the thesis, for example graphs and tables (“Reproductions”), which may be described in this thesis, may not be owned by the author and may be owned by third parties. Such Intellectual Property and Reproductions cannot and must not be made available for use without the prior written permission of the owner(s) of the relevant Intellectual Property and/or Reproductions.
4. Further information on the conditions under which disclosure, publication and commercialisation of the thesis, the Copyright and any Intellectual Property and/or Reproductions described in it may take place is available in the University IP policy (see <http://documents.manchester.ac.uk/DocuInfo.aspx?DocID=487>), in any relevant Thesis restriction declarations deposited in the University Library, the University Library regulations (see <http://www.manchester.ac.uk/library/aboutus/regulations>) and in the University's policy on Presentation of Theses.

Acknowledgements

I wish to thank my supervisors, John Waterton, James O'Connor and Kaye Williams for giving me the opportunity to work on this project. I also wish to thank the Medical Research Council for providing me with two years of funding.

I wish to acknowledge assistance from Brian Telfer and Muhammad Babur, both of whom performed animal handling and helped prepare tumours for histopathology. I also wish to acknowledge Karen Davies for providing support on the 7T MRI scanner when any problems were encountered.

In particular, I wish to thank Emmanouil Moschidis and Weijuan Zhang for sharing an office with me for two years and also Damien McHugh for discussions on diffusion MRI.

Finally, my greatest thanks is to my family, whom have had to endure an onerous burden for a number of months.

Glossary

ADC – Apparent Diffusion Coefficient

T₁- Longitudinal Relaxation Time

DCE-MRI – Dynamic Contrast Enhanced Magnetic Resonance Imaging

ICP-MS – Inductively Coupled Plasma Mass Spectrometry

RF – Radiofrequency Pulse

PGSE – Pulsed Gradient Spin Echo

RARE – Rapid Acquisition With Relaxation Enhancement

PRESS – Point Resolved Spectroscopy

FLASH – Fast Low Angle Shot

V_e – Extravascular Extracellular Space Volume Fraction Per Unit Volume Of Tissue

K_{trans} – Permeability Surface Area Product Per Unit Volume Of Tissue

EES – Extravascular Extracellular Space

B₁ – Applied Magnetic Field

B₀ – Static Magnetic Field

Gadopentetate – Gadopentetate Dimeglumine (Gd-DTPA)

r – Relaxivity of Contrast Agent (mM⁻¹s⁻¹)

TR – Pulse Sequence Repetition Time

TE – Pulse Sequence Echo Time

1. Introduction

1.1 Measurement of the Non-Viable Cell Volume Fraction in Oncology

The application of magnetic resonance imaging to oncology is a mature field [1] and has enjoyed success in diagnostic radiology. The rich contrast available due to the heterogeneity of the water proton environment in living organisms offers the potential to detect and characterise disease progression through non-invasive and non-ionising means. A more accurate means of quantifying the chemical environment of a tumour has explored changes in the T_1 and T_2 relaxation times ([2], [3]) of nuclear magnetisation. The distribution of water protons in different compartments [4] introduces a spatial variation in these relaxation times. The relative size of the different water compartments and their change in response to treatment has been investigated, in particular that of the extracellular water compartment (extravascular extracellular space, EES) through the administration of a gadolinium based contrast agent [5]. The linear relationship between contrast agent concentration in the extracellular water compartment and reduction in T_1 initiated the development of pharmacokinetic models to extract physiologic information [6]. Such analyses have not been restricted to oncology but through a different methodology have been applied in cardiology [7], with considerable success. A measure of the cell volume fraction (v_e) was introduced as a means of quantifying the volume within a tumour that is accessible to the contrast agent. Predicated upon the assumption that increases in cell volume fraction are proportional to the degree of cell death, v_e would appear a highly valuable measure of treatment efficacy. As will be explored further below, v_e suffers from significant confounds which preclude its application as a valid biomarker of cell death or cellularity in oncology, particularly so in multicenter trials.

Diffusion weighted magnetic resonance imaging has been applied in oncology to assess tumour cellularity [8]. The Apparent Diffusion Coefficient purports to measure the diffusion coefficient of water molecules in tissue. An increase in the extracellular water content resulting from cell lysis would correspond to an increase in the diffusion coefficient of water molecules. ADC is hypothesised to increase in the absence of viable cells due to a reduced number of impeding cell membrane boundaries [9]. Although ADC does not offer a cell volume “fraction” to be computed, establishing a causal relationship between ADC changes and cell death would offer a highly valuable “biomarker” of treatment efficacy, or proxy for cell death to be established. Validation would be in evidence from agreement between both ADC and v_e on a per tumour basis. Such validation is lacking and represents a significant obstacle for the incorporation of MRI biomarkers into multicenter clinical trials or routine clinical usage [10].

1.2 What are the components of the EES ?

The extravascular extracellular space as defined in the DCE-MRI literature and that of physiology differ in a number of aspects as summarised below.

Pharmacokinetic EES

- Compartments representing the intravascular intracellular, intravascular extracellular, extravascular intracellular and extravascular extracellular water proton spins at constant temperature and viscosity.
- Probability distribution of a water proton is equal on a voxelwise basis (if in fast exchange regime).
- Probability distribution of contrast agent is equal on a voxelwise basis (well mixed compartments).

Physiologic EES

- 150mM Sodium (Na), 5mM Potassium (K).
- Extracellular matrix consisting of Collagen, Fibrinogen and Proteoglycans.
- Probability distribution of a water proton is unequal on a voxelwise basis.
- Probability distribution of contrast agent is unequal on a voxelwise basis.

The pharmacokinetic EES is modelled using compartmental analysis, invoking assumptions of a well mixed, constant temperature, constant viscosity, electroneutral environment in which water proton spins and contrast agent molecules are compartmentalised. The physiological EES is a heterogeneous environment, a variety of macromolecules and proteins interact with the rapidly exchanging water proton spins and contrast agent molecules. A number of different biophysical processes contribute to the uptake of therapeutic agents into cells ([11],[12],[13],[14]) through the extravascular extracellular space. The tumour microenvironment consists of a plethora of different cells in addition to cancerous cells. In particular lymphocytes, tumour-associated macrophages, mast cells, mesenchymal stem cells, bone marrow derived cells, neutrophils, pericytes, myeloid derived stem cells, endothelial cells, TIE2-expressing monocytes, non-cancerous epithelial cells (in the case of a carcinoma) and evidently the cancerous cells themselves as illustrated in figure 1.

The relationship between the extravascular extracellular space size and cell density is intuitively inversely proportional. An increase in the density of different cell types will reduce the fraction of the EES available and conversely a decrease in cell density will increase the fraction of the EES ([15], [16]). Such a linear model will not accurately reflect tissue biomechanics where decreasing cell density will result in external pressures exerting an increasing force, leading to compression of the tissue.

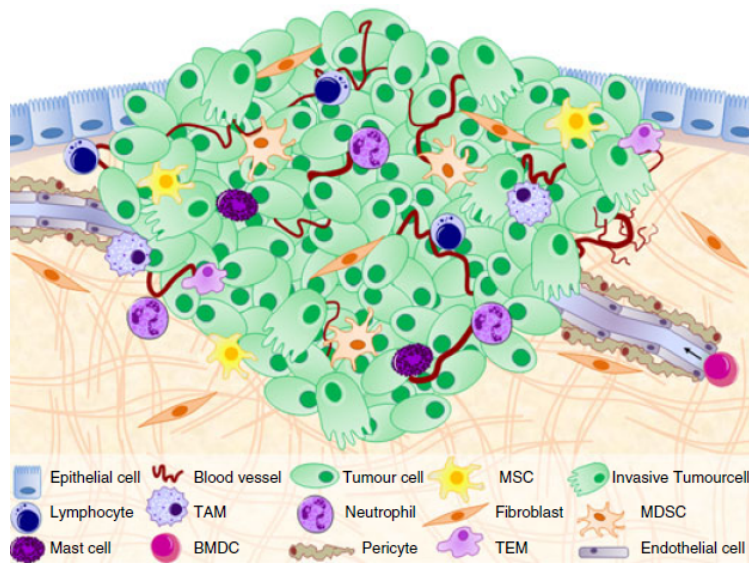


Figure 1:- the above figure is an illustration of the tumour microenvironment [17].

The extracellular matrix provides a supportive structure to cells and consists principally of collagen, fibroblasts, polysaccharides, fibronectin and proteoglycans [17]. The different cells in the tumour microenvironment all interact with the extracellular matrix. There is evidence to suggest that the number of stromal cells in the tumour microenvironment is correlated with increased tumour malignancy [18]. This can be related to the EES by the hypothesised inversely proportional relationship between cell density and extracellular space size. Some ADC literature indicates that a low baseline ADC is associated with an improved response to treatment and prognosis. This appears to contradict results regarding stromal cell density if increases in cell density are concurrent with decreases in ADC. This apparent contradiction serves to illustrate the difficulty in interpreting MRI biomarkers. A comparison between imaging biomarkers and histopathological measures of cell death is seldom observed in clinical studies.

The heterogeneity of the tumour microenvironment results in patient prognosis being dependent upon the particular cell type undergoing a process of cell death. It has been shown that stromal cell apoptosis is correlated with improved patient survival rates when compared to epithelial cell apoptosis [19]. It is challenging to envisage an imaging derived measure capable of deconvolving the different cell types present within a tumour [20]. Separation of the different cell types in vivo using a particular imaging technique would offer significant benefits; the non-specific measures of cell density are a limitation which if overcome could offer far greater insight into the underlying pathophysiological changes taking place. The differing processes of cell death such as apoptosis, necrosis, paraptosis and phagocytosis will all exhibit a complex relationship with the EES. The use of cytotoxic chemotherapeutic drugs and radiation therapy is purported to increase cell death and thus EES size due to the reduced cell density. Indeed, many new chemotherapeutic agents work through interacting with components of the extracellular matrix to selectively target cancerous cells; this matrix is thus a potential target in itself for cancer treatments [21].

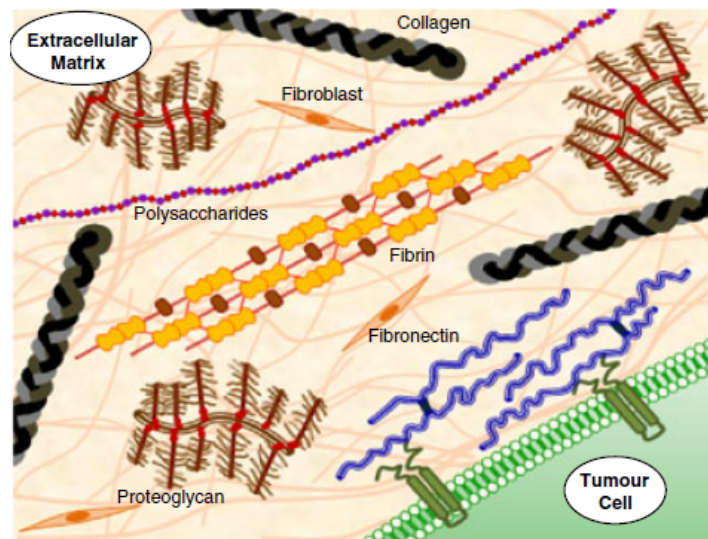


Figure 2:- schematic diagram illustrating how the extracellular matrix provides a supporting structure for cells.

Figure 2 illustrates the different components of the extracellular matrix which are involved in maintaining the structure and environment of the extracellular space. The charge of the different components influences the interactions between the components themselves and also any other media present within the extracellular space.

The properties of the principal components of the extracellular space can be summarised as follows:-

- Fibronectin, a protein which promotes endothelial cell adhesion and has a negative charge within the pH range observed in normal tissues [22].
- Fibrin is produced from fibronectin and possesses a different surface charge density compared to fibronectin and is of opposite polarity. It plays an important role in the clotting of blood.
- Collagen is an important protein structure in providing support for the matrix and enabling the cells to perform their basic function, it has no net charge under physiologic conditions [23].
- Fibroblasts are cells which synthesise the extracellular matrix and collagen thus playing a key role in tumour growth and development.
- The negatively charged proteoglycans play a key role in homeostasis by attracting sodium cations into the extracellular space and thus assisting in the functioning of the sodium/potassium pump. Furthermore the increased concentration of sodium cations attracts water molecules by osmosis down the concentration gradient.
- Glycoproteins such as fibronectin are also present in the extracellular space with functions such as providing support to cells and acting as receptors on cell surfaces [24].

The extracellular space is an oxidizing environment relative to the reducing nature of the intracellular compartment. This helps maintain the disulphide bonds of protein structures within the extracellular matrix [25]. To prevent cellular damage, an extracellular antioxidant system reduces reactive oxygen and nitrogen species, lipid peroxidation and protein oxidation to a tolerable level. Any exogenous chemical introduced into the environment of the extracellular space whether a contrast agent or a cytotoxic chemotherapeutic agent will interact with the matrix, the macromolecular components embedded within it and the chemical environment associated with it. The extracellular environment will potentially have an impact upon the distribution and interaction of molecules introduced exogenously; of key importance in measurements of the extravascular extracellular volume fraction in DCE-MRI.

As cancerous cells begin to proliferate, the development of new vasculature is essential to maintain oxygen and nutrient uptake, in addition to the delivery of immune and red blood cells to the multiplying cancerous cells. The vascular network of a tumour is characterised by being heterogeneous [26], poorly organised and having a “leaky” endothelial cell lining. The highly permeable capillaries within a tumour facilitate perfusion/permeability measurements through the distribution of contrast agent. This enables the concentration of contrast agent as a function of time to be used to infer information about the physiological properties of the tissue on a voxelwise basis. As the distribution of contrast agent throughout a tumour is dependent upon capillary density, capillary permeability and blood flow, DCE-MRI studies have yielded positive correlations between pharmacokinetic parameters and histopathological metrics of perfusion and vessel density.

1.3 Cell Death and the Extravascular Extracellular Space

1.3.1 Apoptosis

Apoptosis is a process of cell death whereby the cell manages its demise through two key pathways (extrinsic and intrinsic). The process is characterised by morphological changes which occur over time, these are: cellular shrinkage, condensation and marginalisation of the nuclear chromatin, DNA fragmentation, cytoplasmic vacuolisation and cell lysis with subsequent phagocytosis by neighbouring cells and macrophages [27]. Apoptosis is essential for the maintenance of homeostasis in multicellular organisms. One of the hallmarks of cancer is the resistance of cancerous cells to apoptosis, enabling them to proliferate [28].

One would anticipate the process of apoptosis to reduce the cancerous cell density. As apoptosis is a time dependent process there will be a time dependent variation in the cell density within a tumour. As apoptotic cells are engulfed by surrounding cells and macrophages the diffusion coefficient of water molecules is purported to increase as phagocytosis and digestion take place. It is evident however, that any immune response by macrophages would increase the local cell density. Macrophages are similar in size to normal cells and as such will impede water diffusion in a fashion akin to that of cancerous cells [14]. Deconvolving the effect that apoptosis will have upon the EES volume fraction is non-trivial due to the complex biochemical pathways involved and indeed the possible non-linearity of the tissue response. There is no clear causal relationship between apoptosis and ADC increases or decreases.

1.3.2 Necrosis

Necrosis is considered to be the post-mortem changes which take place once a cell has died [13]. The intermediate stages before a cell reaches what can be regarded as a necrotic state can be morphologically described by cell swelling (oedema), organelle swelling, “blebbing” of the cell membrane and increased membrane permeability. The remaining cellular material will then be removed by phagocytosis inducing an immune response and thus inflammation. Alternatively cells may proceed through the pathway for apoptosis as described above before ultimately ending what can be described as a state of necrosis.

The two different processes can be summarised in figure 3 below which also details the key morphological changes which take place. As necrosis is associated with the removal of waste by macrophages and inflammation changes in EES volume fraction will be non-trivial to interpret. Cytotoxic oedema would cause a reduction in the EES and an increase in ADC as cells swell (depending upon the parameters of the MRI sequence). Extracting the underlying changes taking place depends upon the imaging time points chosen post treatment. It is non-trivial to infer the exact changes in the EES which may occur from these different mechanisms of cell death. There is no clear causal relationship between necrosis and ADC changes.

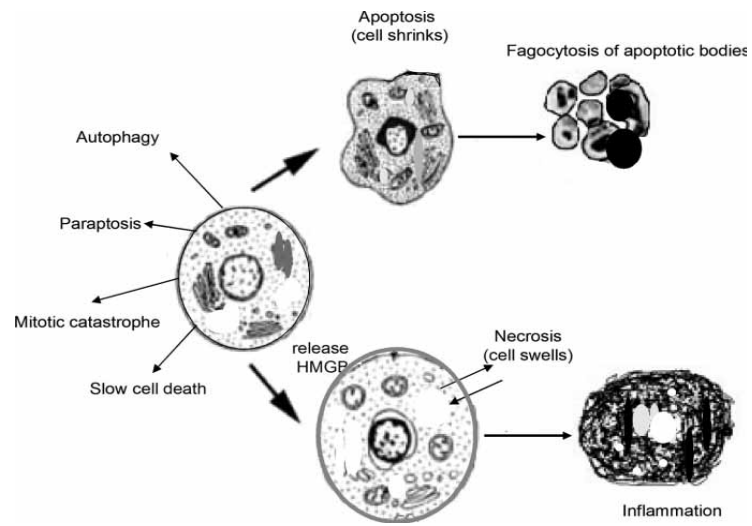


Figure 3: the two dominant mechanisms of cell death (apoptosis and necrosis) are illustrated above [13].

1.4 Where does “ v_e ” come from and what does it purport to measure?

The application of mathematical models to describe the uptake and distribution of a contrast agent in DCE-MRI has its origins in the nuclear medicine literature [29]. Indeed, consistency with the models available from nuclear medicine was an objective of the early pioneers of quantitative DCE-MRI [6]. For explanatory purposes the concentration of contrast agent on a voxel wise basis in tissue is considered as the arithmetic sum of that in the blood plasma and the extravascular extracellular space (for a contrast agent unable to penetrate into the intracellular space).

$$[1] \quad C_t(t) = v_p C_p(t) + v_e C_e(t)$$

The above equation represents a well mixed “two-compartment” model (two separate compartments are accessible to the contrast agent) with the two coefficients v_e and v_p introduced as the volume of extravascular extracellular space per unit volume of tissue (or alternatively the volume of the EES for a specific agent per unit volume of the tumour) and the blood plasma volume per unit volume of tissue. The concentration in tissue as a function of time varies as the contribution from the blood plasma decreases as diffusion and advection result in the transport of contrast into the EES with a concomitant increase in the $C_e(t)$ term in equation 1 above. Conservation of mass implies that contrast in the blood plasma flowing into a tumour (at time $t=0$) must flow out from the tumour at a later time ($t=t'$). The rate of change of contrast agent in tissue as a function of time can be hypothesised to be proportional to the contrast in the blood plasma minus that in the extravascular extracellular space multiplied by some constant. This is formulated below in what is known as a generalised kinetic model [30].

$$[2] \quad \frac{dC_t(t)}{dt} = K_{trans} \cdot C_p(t) - (K_{trans} / v_e) \cdot C_t(t)$$

With initial conditions that $C_p = C_t = C_e = 0$ at $t=0$ (prior to the administration of contrast agent) the solution below is obtained through the use of the Laplace transform for a first order ordinary differential equation with a forcing term.

$$[3] \quad C_t(t) = K_{trans} \int_0^t C_p(u) e^{-(K_{trans}/v_e) \cdot (t-u)} du$$

It can be seen that the concentration of contrast agent in tissue as a function of time is the convolution between the tissue response function and the arterial input function multiplied by K_{trans} (where K_{trans} represents the permeability surface area product per unit volume of tissue with units of min^{-1}).

$$[4] \quad K_{trans} = EF \rho (1 - Hct)$$

In the above equation “E” represents the extraction fraction (unitless), F the perfusion (units of $\text{ml g}^{-1} \text{min}^{-1}$), “Hct” the blood hematocrit (unitless) and ρ the density of the tissue (units of g/ml). There are several models available for DCE-MRI data analysis [31], the most commonly applied are summarised below with their respective degrees of freedom:-

Model	Degrees of Freedom
Tofts [6]	2
Extended Tofts [30]	3
Kety [33]	2
Extended Kety [34]	3
Two Compartment Exchange [35]	4
Patlak [36]	2
Constant Infusion [7]	1
BOLERO [37]	3
BALDERO [32]	5

Table 1: the above table illustrates the variety of different pharmacokinetic models available and the degrees of freedom in the data fitting process.

Degrees of freedom refers to the number of free parameters in the minimisation process. In the constant infusion model, the value for v_e is obtained not through a minimisation process but from linear algebra. The Brix model possesses the same structure as the two compartment exchange model, as such it was not included above. It does however have an alternative physical interpretation [38]. The Brix model makes an assumption that the flow of contrast agent from the vasculature into the EES does not contribute significantly to the relaxation time shortening. This simplification can be corrected by including the flow of contrast from the vasculature into the EES. Increasing the complexity of the model in DCE-MRI is often employed by introducing additional compartments as in the case of the modified Brix model.

This can be a misleading route to follow as obtaining a unique solution requires a minimum number of compartments. This is discussed further in section 1.6. The impact of inaccuracies in the arterial input function used to describe the passage of the contrast agent bolus in the vasculature upon the measurement of v_e has been shown to be relatively small [39]. In the reference region model, two dynamic curves are simultaneously sampled from the target voxel and a nearby reference region which has known values of v_e and K_{trans} . The use of an arterial input function to model the input of contrast in the vasculature is

obviated by jointly solving two pharmacokinetic equations for target voxel and reference region. The application of a particular model will depend upon the pathology under study and the imaging sequences available [40].

1.5 Non-MRI Methods of Measuring the Extravascular Extracellular Space

Obtaining a non-MRI derived measure of EES size has explored both the intrinsic properties of the extravascular extracellular space and the application of a variety of extrinsic contrast agents. An unbiased estimate of the EES requires a non-specific agent. Targeting with molecular agents, such as nanoparticles, does not appear to satisfy this caveat [41]. Imaging of the EES size has been performed using SPECT, optical imaging modalities and also Bromide PET [42]. The use of ^{99m}Tc ligated with DTPA has proven successful in measuring the extracellular volume in rabbit leg muscles [43]. It should be noted however that in this study the authors used DTPA as the ligand for ^{99m}Tc and also for the Gadolinium ion. Without evidence that the distribution of contrast agent into the EES is unbiased, any correlation between the two measures is invalid. The lack of histological validation in this study raises additional confounds as no “gold standard” method of measuring cell density is performed.

The high extracellular concentration of Bromide ions in the extravascular extracellular space has enabled measurements using Bromide PET to be made with exogenously introduced radioactive Bromide (^{76}Br) isotopes. In addition to this, the intravenous administration of stable Bromide isotopes [44] and subsequent sampling of the Bromide washout as a function of time has been explored in anaesthesiology. Confounds of the former methods include that the annihilation energy of photons emitted from ^{76}Br is greater than that of ^{18}F as is used in FDG-PET (3.941 versus 1.12 MeV). The invasive nature of the Bromide, Iohexol and sodium dilution method is a practical confound. Methodological concerns include that the volume of distribution calculated by means of intravenous Bromide sampling is a whole body distribution; not for a particular organ or tissue.

The use of albumin-Evans blue in measuring the EES size has shown promise due to its consistent accumulation in the EES independent of tumour type, as in evidence from a study of different melanoma xenografts [45]. A confound of the latter methodology is that the means of obtaining the amount of albumin-Evans blue in a particular tissue through photometry minimises its translational potential. The distribution of albumin in the extracellular space is impeded by collagen, glycosaminoglycans and proteoglycans, although this can also be said for contrast agents. Inulin has been explored as another biomarker of the EES, this would be another method for preclinical validation [29].

The use of MRS to measure the EES volume has looked at creatine phosphate [11] and phenylphosphonic acid [12] as markers of the EES. The dependence of volume ratios as a means of calculating the EES through the use of phenylphosphonic acid is one possible confound as is the transport of xenobiotic substances such as (PhePo) in the rat liver. The toxicity of phosphonates places a limitation upon their use for in vivo preclinical work and would prevent their use in the clinical setting.

One would anticipate a positive correlation between biomarkers of cell death and EES size respectively if the purported linearity between the two is valid. The use of multi-modal imaging modalities should enable comparison of measurements made on different imaging modalities to assess their sensitivity and specificity compared to a known “gold standard”.

1.6 How can we model the Extravascular Extracellular Space ?

Cancer is a multifaceted disease with the growth and development of a tumour attributed to a number of competing factors [28]. A highly proliferative cell line will undergo a high rate of mitotic division, increasing the number of cancerous cells at an approximately exponential rate. The non-linearity of cellular proliferation results in a net increase in the cell density, where cell density is defined as the number of cells per unit volume of tissue. Tumour growth and its relationship with the extravascular extracellular space is discussed further in section 1.6.2. In particular, physiologic models are compared to their DCE-MRI counterparts. A number of the salient confounds associated with pharmacokinetic modelling in DCE-MRI are summarised below.

1.6.1 Pharmacokinetic Extravascular Extracellular Space

The compartmentalisation of tissue, as applied in the DCE-MRI literature postulates that tissue can be subdivided into separate compartments for different water proton environments. A number of the confounds are presented below:

1.6.1.1 Thermodynamic Confounds

The longitudinal relaxation time is an intensive thermodynamic quantity, it does not vary depending on the size of the sample. This is contrary to that observed in nuclear medicine with signal intensity increases proportional to increases in the tracer concentration. The calculated T_1 is also dependent on temperature (as is the relaxivity of the contrast agent), magnetic field strength and indeed the viscosity of the sample. Variation in these parameters during an experiment will result in a change in the calculated T_1 value, independent of the concentration of contrast agent. In addition, the relaxivity of the contrast agent may vary depending on whether it is in plasma or the interstitial space of a tumour [46]. The linear relationship between ΔR_1 and contrast agent concentration becomes increasingly invalid at high contrast agent concentrations [47]. As a result, well perfused areas of a tumour may have significant non-linearities in signal intensity as a function of contrast agent concentration.

1.6.1.2 Mathematical Confounds

High temporal resolution is required to accurately characterise the impulse response function and arterial input function. It has been shown that numerical algorithms require such high temporal resolution for accurate convolution [48]. The temporal resolution currently available in MRI experiments (of the order of seconds). The PET literature indicates that a (from where methodology for DCE-MRI models originated) much higher temporal resolution can be attained [49]. The use of the Laplace

transform to solve the coupled differential equations in the Laplace domain, before transferring into the time domain introduces the convolution integral into the solution. This method takes advantage of the relationship between the product of two Laplace transforms and the convolution of two functions in the time domain.

Representing a bolus of contrast agent as an impulse by [50]

$$[5] \quad \delta(t)$$

and a tissue response by

$$[6] \quad h(t)$$

enables the relationship between the IRF and convolution to be explored further.

If the impulse is delayed by a time

$$[7] \quad i \Delta T$$

then the corresponding impulse becomes

$$[8] \quad \delta(t - i \Delta T)$$

and the response

$$[9] \quad h(t - i \Delta T)$$

If the impulse has an area

$$[10] \quad A$$

and is delayed by

$$[11] \quad i \Delta T$$

then the the response is given by

$$[12] \quad Ah(t - i \Delta T)$$

The area of the impulse at

$$[13] \quad t = i \Delta T = f(i \Delta T) \Delta T$$

The delayed and shifted impulse response is given by

$$[14] \quad f(i \Delta T) \Delta T h(t - i \Delta T)$$

The response of the system to a series of delayed impulses is given by

$$[15] \quad y(t) = \sum_{i=0}^{\infty} (f(i \Delta T) \Delta T) h(t - i \Delta T)$$

Taking the limit

$$[16] \quad \Delta T \rightarrow 0$$

Implies that

$$[17] \quad i \Delta T = \lambda$$

thus

$$[18] \quad \Delta T = d\lambda$$

and as such the output from the system is the convolution of the impulse response function and the input to the system

$$[19] \quad y(t) = \int_{-\infty}^{+\infty} f(\lambda) h(t - \lambda) d\lambda \quad .$$

The uniqueness of the solution obtained in linear compartment analysis is of concern. Even an exact knowledge of the impulse response is insufficient to determine uniquely the system that produced the impulse response. A different linear model with an identical impulse response can always be found by increasing the number of compartments of the model [51]. Obviating the above methodology has been performed with constant infusion in cardiology for calculation of v_e . The linear relationship between T_1 and contrast agent concentration, in conjunction with the homogeneous T_1 observed in myocardium is the theoretical basis of this method. The simplifying assumptions regarding homogeneity implicit in constant infusion do not appear to be applicable to oncology.

1.6.1.3 Physiological Confounds

Once a malignant tumour reaches a few mm³ in volume, the passive diffusion of metabolites from host tissue vessels is no longer sufficient for continued proliferation. The growth of new capillaries in a tumour through neovascularisation or angiogenesis results in irregularly formed highly permeable vessels. The perfusion of these vessels fluctuates randomly as a function of time [26]. This represents a significant physiologic confound in the analysis of purported measures of permeability and flow. Regions of tumour having a time dependent perfusion will be poorly represented by DCE-MRI models, placing significant constraints upon the interpretation of the parameters produced. Indeed, it makes the analysis of pharmacokinetic parameters longitudinally challenging. There is also evidence to suggest that the chelating ligand of the gadolinium ion interacts with components of the extracellular matrix. As a result, the T_1 distribution would become dependent upon electrostatic interactions between the ligand and ECM components [52]. Standard pharmacokinetic models assume a “well mixed” voxelwise concentration. Such assumptions are maintained with the shutter speed generation of models (discussed further in 1.7).

1.6.1.4 Imaging Confounds

The relationship between contrast agent concentration and ΔR_1 is linear, except at high concentrations of contrast agent where signal saturation occurs. As such, the sequence becomes insensitive to changes in tissue R_1 and thus contrast agent concentration. The contrast concentration can be computed from DCE-MRI images by solving the non-linear relationship between the FLASH signal and the concentration of contrast agent [53]. This non-linear conversion technique minimises the impact of possible underestimation of actual contrast concentration, due to signal saturation at high concentrations. The voxel size of a DCE-MRI sequence has shown sensitivity to the pharmacokinetic model applied. Increasing the voxel size and thus decreasing resolution results in an increasing preference for a simpler model fit, with fewer degrees of freedom. The compartmentalisation of a voxel (if fitting is performed on a voxelwise basis) appears implausible given the number of cellular components and variety of transport processes involved (advection, convection and diffusion). The development of a statistical model to incorporate the probability of contrast agent remaining intravascular or extravascular and indeed the water proton distribution on a voxelwise basis is developed in the future work section.

1.6.2 Physiologic Extravascular Extracellular Space

The mathematical modelling of tissue growth kinetics using biphasic mixture theory indicates that the processes of tumour growth and vascular collapse are non-linear [54]. As the contrast agent exits the capillaries into the interstitial space, complex fluid dynamics results in distribution of the contrast agent. This is contrary to that implied by the linear models derived from indicator dilution theory used in DCE-MRI. Although DCE-MRI models are applied to contrast uptake and washout, the

complex interaction between contrast agent, vascular function and extracellular matrix components would not appear to be accurately modelled by linear compartment analysis.

1.7 Do “Shutter-Speed” effects explain the disagreement between ADC and v_e ?

It has been postulated that the discrepancy which exists between ADC and v_e could potentially be explained by the non-zero intracellular lifetime of a water proton spin (τ_i). As the contrast agent is injected, the concentration gradient between the capillaries and the interstitial space is at its greatest value. It is at high concentrations of contrast agent that shutter speed effects begin to undermine the assumption of infinitely fast water exchange between the intracellular and extravascular extracellular space (EES) ([55], [56]) in comparison to standard models based upon indicator dilution theory which have been widely applied in the analysis of DCE-MRI data as previously discussed (i.e. linear dependence of T_1 on [CR]-contrast agent).

Incorporating the effects of inter-compartmental exchange into a pharmacokinetic model has been observed to produce pharmacokinetic parameters differing from their standard model analogues by parameter underestimation. This is purported to result from the implicit assumption of a zero mean intracellular water molecule lifetime [32]. The current models incorporating shutter speed effects all assume well mixed compartments (i.e. contrast agent entering a compartment is immediately distributed uniformly through the compartment), a confound of many pharmacokinetic analyses ([57], [58]) although alternatives do exist ([59], [60]). Particular to the BOLERO (bolus enhanced relaxation overview) and BALDERO (blood agent level dependent and extravasation relaxation overview) shutter speed models is the assumption that the majority of water is intracellular; something which is a reasonable approximation in viable tissue but not under pathology [61]. Thus, both fast exchange and shutter speed models suffer from methodological confounds which limit the accuracy with which they model underlying pathophysiology. Both ADC and v_e are highly sensitive to the particular sequence parameters, this will impact upon any possible agreement independent of model fitting and pathophysiological variables.

1.8 What scientific value exists in exploring the temporal evolution of v_e ?

Exploring the temporal variation in the concentration of contrast agent and thus the calculated value of v_e , requires a high temporal resolution sequence to enable accurate characterisation of the arterial input function, in addition to requirements for the accurate convolution of the impulse response function with the input function (AIF). It has been reported that a temporal resolution of over 10 seconds is coincident with highly inaccurate parameter values [31]. The validity of pharmacokinetic parameters computed for extended time periods is thus questionable.

The total transit time in tissue for a contrast agent is typically between 2-5 minutes [31]. As such, extending an imaging acquisition time beyond 10 minutes is not necessary for full characterisation of the contrast washout from the EES [31]. Once the tissue time curve reaches a plateau the maximum concentration of contrast agent has been distributed throughout the tissue. Assuming a spherical geometry and using tumour volume data from preclinical studies in conjunction with the mean diffusion coefficient for gadopentetate observed in a preclinical tumour model, the time taken for distribution of contrast agent throughout the tumour can be calculated as 165 seconds (+/-70 secs) [62]. This indicates that distribution of the contrast agent throughout the tumour occurs within a relatively short time period post injection.

The figures below illustrate an example of a tissue concentration time curve obtained using an AIF from the literature [63] and corresponding mean values for v_e and K_{trans} (0.127 and 0.0021 respectively) taken over the duration of the 5 minute scan. This AIF is representative of that available in the literature. Different tumour models and imaging parameters can result in different AIF models. It should be noted that the units for concentration presented in this paper are incorrect (mmol rather than mM). To obtain the concentration time curve this amount in mmol must be divided by the volume of the voxel size used in their study. As such, the data from this paper is used for illustrative purposes only.

The effect of curtailing the experiment at different time points is illustrated. The graphs below were performed in *Mathematica*. Convolution was performed manually.

The AIF is conventionally modelled by a biexponential decay:

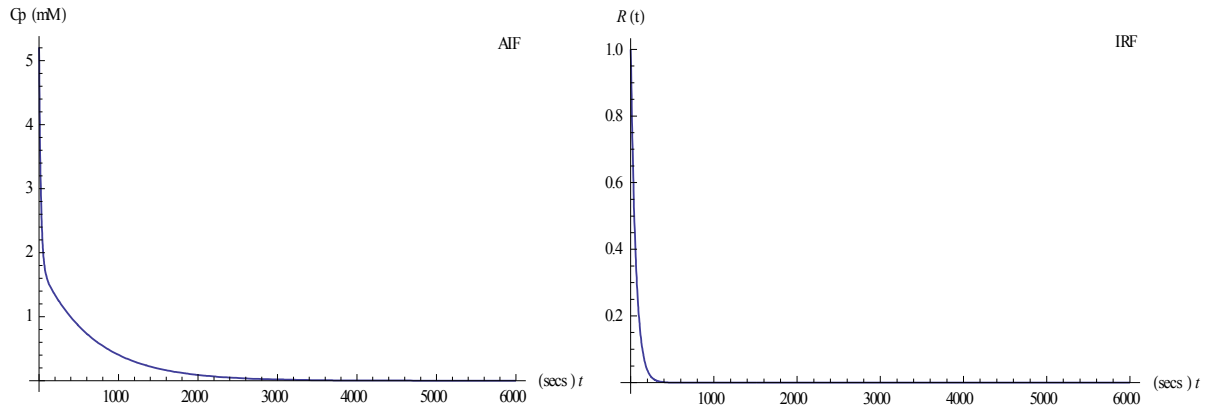
$$[20] \quad C_p(t) = A e^{-m_1 t} + B e^{-m_2 t}$$

where A and B have units of mmol and m_1 and m_2 of s^{-1}

and the IRF by

$$[21] \quad IRF = a e^{-t(\frac{a}{b})}$$

In the equation above a represents K_{trans} and b v_e . The two equations are plotted below:



Figures 4 (left) and 5 (right) :-the above figures display the arterial input function and impulse response function for the stated parameter values.

Convolution of the equations above yields :

$$[22] \quad C_t(t) = aA e^{-t(\frac{a}{b})} \left[\frac{-1}{(m_1 - \frac{a}{b})} e^{-t(m_1 - \frac{a}{b})} + \frac{1}{(m_1 - \frac{a}{b})} \right] + aB e^{-t(\frac{a}{b})} \left[\frac{-1}{(m_2 - \frac{a}{b})} e^{-t(m_2 - \frac{a}{b})} + \frac{1}{(m_2 - \frac{a}{b})} \right]$$

The equation above is plotted for $K_{trans} = 0.0021$ and $v_e = 0.127$ for 0 to 600 seconds and 0 to 6000 seconds to illustrate the effect of truncating an imaging experiment of the tissue concentration curves observed.

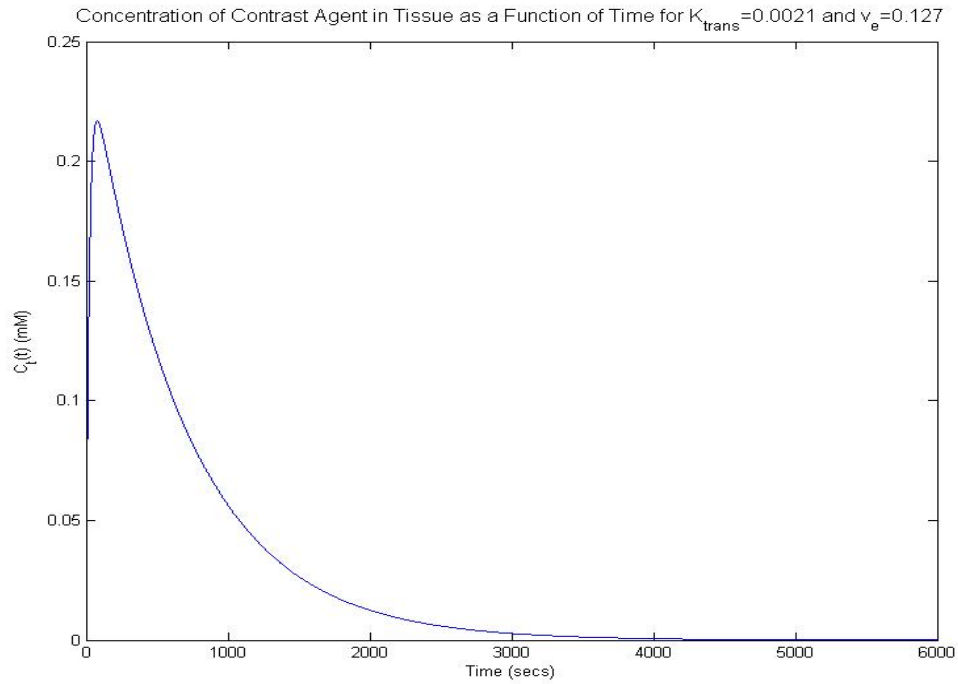


Figure 6: the above figure illustrates the contrast agent concentration in tissue as a function of time over an extended time period (100 minutes).

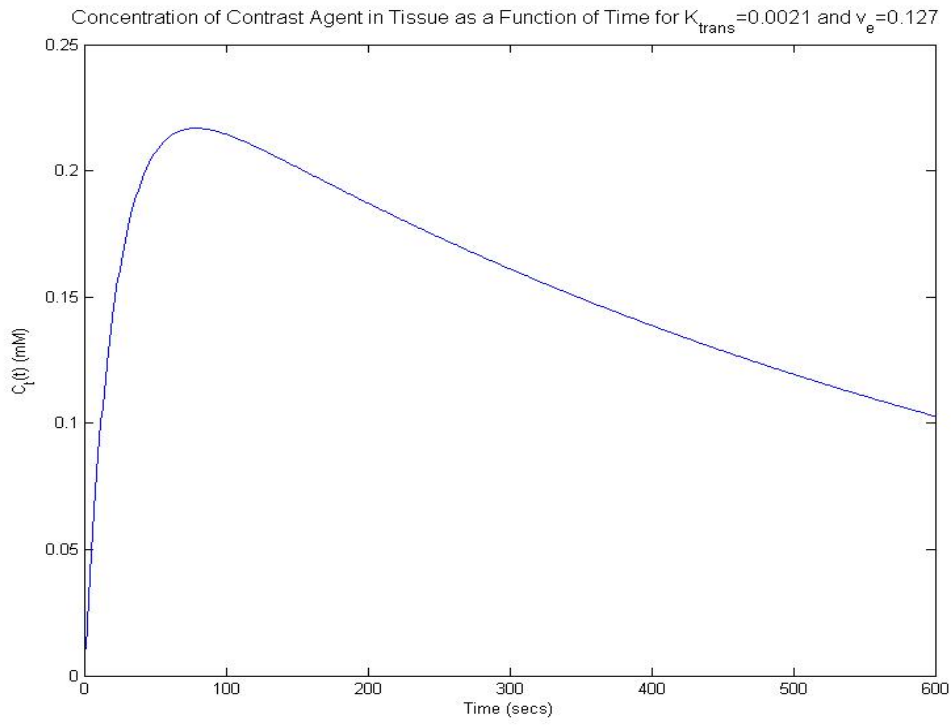


Figure 7: the figure above illustrates the temporal evolution of the concentration of contrast agent in tissue over a shorter time period (10 minutes).

The peak concentration of contrast agent appears to occur at approximately 82 seconds. Following this the contrast is being removed from the voxel as the concentration decreases over time. Models dependent upon a unidirectional flux of contrast agent are invalid at long time periods due to the complex processes of diffusion, convection and advection present on a voxelwise basis. The assertion that an accurate value for v_e (where accuracy is determined by its agreement with histopathological measures of necrosis (%H&E)) may be obtained from imaging at long time periods appears unjustified. Not solely due to the breakdown of the validity of the models but due to the fact that the peak tissue concentrations have already been measured at 82 seconds in the uptake phase of the model. The combined validation of models and algorithms employed in DCE-MRI studies is an area which lacks detailed scrutiny and is ignored in much of the literature [64].

1.9 Accurate Modelling of the Tumour Microenvironment

Convolution of the impulse response function with an arterial input function yields the concentration of contrast agent in tissue as a function of time as detailed previously. The solution obtained with the convolution integral is a zero state response; this implicitly assumes that all the initial conditions are equal to zero at $t=0$. Equivalently a zero state response is the response to an input when the system has zero initial conditions. The assumption of zero initial conditions may not be an accurate assumption to be made when describing the response of a tissue to the arrival of a bolus of contrast agent. A similar zero state response is applied in the analysis of linear time-invariant electronic circuits and indeed the parameters derived from pharmacokinetic analysis can be compared to their electronic analogues. It is of concern that the distribution of contrast agent

as a function of time is measured in absolute terms due to the assumption of well mixed compartments and linearity between T_1 and contrast agent concentration. The heterogeneity of the tumour microenvironment on a voxelwise basis is in evidence by assuming a cell radius of approximately $6 \mu m$ and a spherically shaped cell. A voxel size of $2.4 \times 10^{-10} m^3$ ($0.02 \times 0.02 \times 0.6$ cm) will contain a maximum of approximately 265,252 cells. An example of an arterial input function taken from the literature is shown again below for illustrative purposes, in this case the time period of evolution is for approximately 17 minutes. Simulations were performed in *Matlab*.

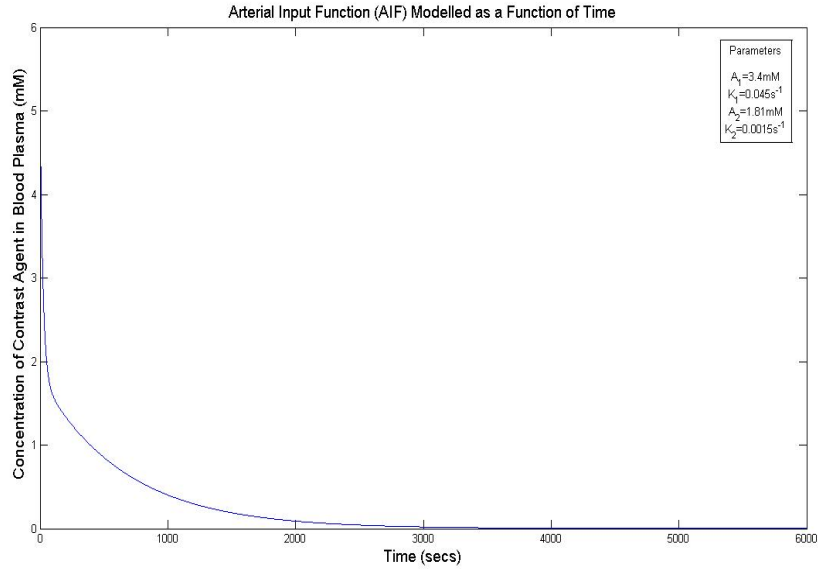


Figure 8: the biexponential decay model for an AIF is simulated above. The panel in the top right hand corner of the figure illustrates the parameters of the biexponential decay.

An impulse response function using a value for K_{trans} obtained from the literature (0.0021 min^{-1}) and with variable v_e is illustrated below:

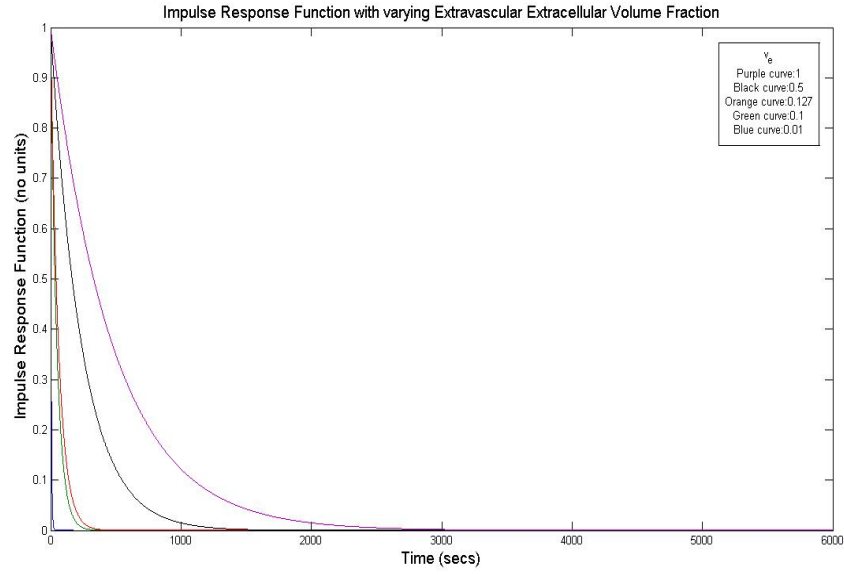


Figure 9: an impulse response function with a constant K_{trans} and variable v_e is illustrated.

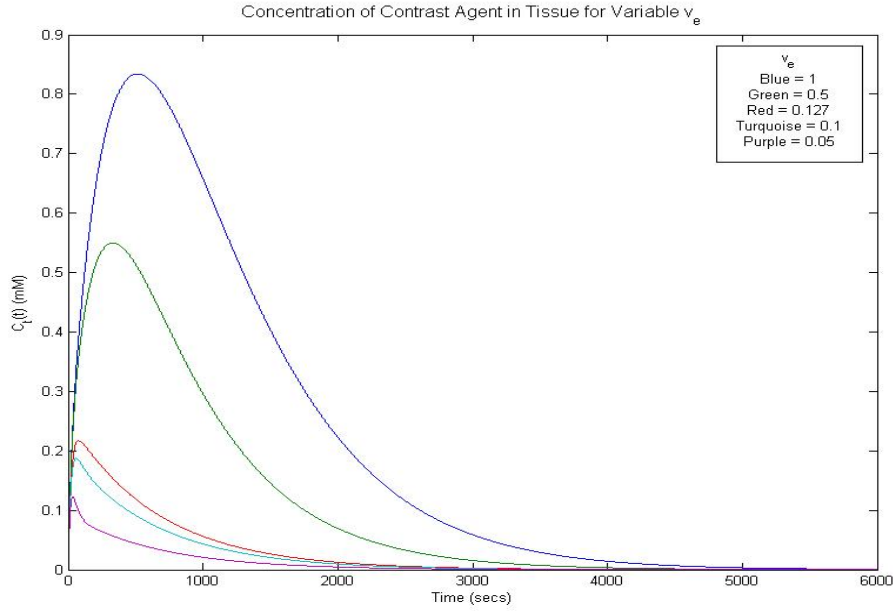


Figure 10: the tissue concentration as a function of time for a constant K_{trans} and variable v_e is simulated above by convolving the respective impulse response functions with the arterial input function.

Increases in the volume fraction of the extravascular extracellular space accessible to the contrast agent results in a non-linear increase in the concentration of contrast agent in tissue on a voxelwise basis for constant K_{trans} . The effect of a variable K_{trans} with a constant v_e on the tissue concentration of contrast agent as a function of time is shown below:

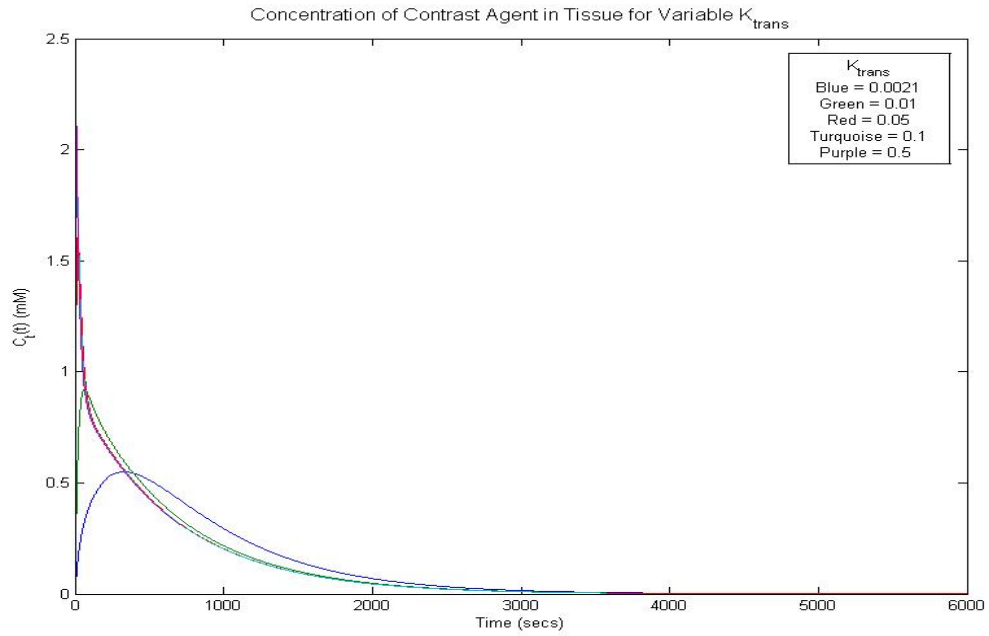


Figure 11: the above figure illustrates the effect that varying the value of K_{trans} for constant $v_e = 0.5$ has upon the concentration of contrast agent in tissue compartment.

The graph with the lowest value for K_{trans} appears to have a greater amount of contrast agent in tissue as a function of time. Thus a region of reduced permeability with a extravascular extracellular volume fraction of size equal to that of other areas in the tumour is associated with a reduced peak concentration of contrast agent present in the tissue compartment. It is of importance to note that an intravascular contribution was not included in the modelling and as such the contribution from contrast agent in the blood plasma was considered to be negligible. The scenarios of increased K_{trans} and v_e result in increases in the peak concentration in the tissue time concentration curve. A model of increased vessel permeability and extravascular extracellular volume fraction as presented can be postulated to result in an increase in diffusion from the capillaries. These simulations offer evidence to support a number of basic assumptions in the Tofts model.

1.10 Computational methods for determining a value for v_e from pharmacokinetic models

The pharmacokinetic model of interest is fitted to a tissue concentration versus time data series conventionally acquired with a high temporal resolution sequence to enable accurate characterisation of the arterial input function. Subsequently, a Levenberg-Marquardt algorithm is used in a non-linear least squares minimisation routine to determine the values of K_{trans} and v_e given the known value for C_p from the AIF and the voxelwise concentration of contrast agent in tissue (C_t). The values of K_{trans} and v_e are iteratively varied until those which minimise the sum of square residuals are obtained. The use of simplex minimisation has been explored as an alternative to the Levenberg-Marquardt algorithm [65]. Of note is that the simplex minimisation is applied to a model which does not appear to be sufficiently poorly scaled to make inferences regarding its accuracy. The possibility of

employing finite element methods in the analysis of DCE-MRI data sets, through the use of Navier-Stokes equation for fluid flow, is one possible area which could be explored in the future. Validation of algorithms in DCE-MRI analysis is an area of importance which requires addressing.

1.10.1 What can we consider to be physiologic parameter values and under what conditions are they produced ?

The choice of starting values for the pharmacokinetic parameters v_e and K_{trans} in the least squares minimisation will influence the final value produced by the optimisation. This is particularly so in poorly scaled problems; a problem in which the values of the objective, constraints or intermediate results differ by orders of magnitude. The units of concentration of the contrast agent on a voxelwise basis is quoted in units of millimolar (mM), starting values of v_e are conventionally require to satisfy the physiologic regime $0 < v_e < 1$. The production of negative parameter values raises important questions regarding the physiologic interpretation of parameters in the DCE-MRI literature [66].

1.11 Diffusion MRI as a biomarker of the non-viable cell fraction

The diffusion of a water proton spin in the tissue micro-environment is purported to depend upon the presence or absence of cell membrane boundaries. If water molecules diffuse unimpeded by any boundaries or structures then the respective diffusion coefficient would be anticipated to be larger than that observed in a highly cellular micro-environment. Water is distributed in both the intravascular intracellular, intravascular extracellular, extravascular extracellular and extravascular intracellular spaces of tissue. The diffusion coefficient of water proton spins is purported to vary between the different compartments due to the variation in density of impeding structures present. The highly structured form of cancerous tissue with an enlarged number of mitoses, irregular cell form and enhanced nucleus/plasma ratio results in the water molecules experiencing a hierarchy of structure that extends to much smaller scales than in the differentiated cells that one would encounter in “normal” tissue [67]. To understand the effect that such a hierarchy of structure would have upon a water proton the concept of an effective diffusion time is of importance in determining the relaxation function form. The fractal scaling of lengths determines the form of the probability density over the range of the evolutionary time scale accessible to the MRI measurement. Three particular function forms depends upon the effective diffusion time and are illustrated below:

$$[23] \quad E = \exp(-Db) \quad (Debye)$$

$$[24] \quad E = \exp(-(Db)^a) \quad (KWW)$$

$$[25] \quad E = (q^2)^{-u} \quad (Power Law)$$

The Debye formalism shown above is applicable when the diffusing proton spins do not have sufficient time to experience impeding local structures and is observed in a water phantom. Short effective diffusion times result in water protons not having sufficient time to experience the local cellular structure and as such it is difficult to distinguish between water protons in different compartments. The resolution available in the diffusion experiment is specified as the minimum root mean square distance that a water proton must move to sense the spatial encoding by the gradient.

There is a significant literature, both clinical and preclinical investigating the potential of ADC to gauge treatment efficacy or provide prognostic information. The relationship between ADC and cell density/cell volume fraction appear to indicate that ADC is a valuable potential biomarker of cell density. What is apparent from both clinical and preclinical studies is that a low initial ADC is a key factor in assessing whether a positive response will be achieved. A low ADC at baseline has been associated with a good response to treatment [68]. Conversely, a high stromal cell density has been associated with a poor response to treatment. This is a good example of the contradictions between imaging and biological studies available in the literature. It appears that a unique correspondence between imaging and pathology is unavailable due to such irreconcilable results. The inability of ADC to determine the effectiveness of therapy can be partly attributed due to the different interventions used in the studies (chemotherapy, radiotherapy or chemoradiation treatment). It is apparent that the particular cancer studied also plays a role in determining treatment response. Preclinical studies of the colon carcinoma HT29 cell line indicated that ADC does not accurately predict therapy effectiveness but that the mean ADC change does. Clinical studies indicating that ADC can accurately determine patient prognosis have included breast cancer patients [69]. The use of diffusion imaging in cancer studies has looked at the effect of both radiation therapy [70], [71] and chemotherapy as interventions to gauge cell death and also to assess the viability of ADC as a predictor of response to treatment. The differing processes of cell death and inflammation will have an influence upon the ADC values obtained in a particular tissue of interest.

1.12 Comparative Studies of ADC and DCE-MRI Pharmacokinetic Parameters

As discussed, studies exploring the relationship between ADC and the pharmacokinetic parameter v_e have hitherto failed to yield any correlation [10]. The electrical conductivity of the EES differs relative to that of the intracellular space. Porous media theory predicts that tissue water ADC should correspond with electrical conductivity and thus the EES. This relationship has been observed experimentally [72].

2. Validation of Experimental Methodology

2.1 Introduction

The validation of experimental methodology in the development of imaging biomarkers should enable the observed imaging parameters to be more closely attributed to underlying pathophysiology, rather than instrumental effects or some other source of bias. Subchapters 2.2-2.3 detail the experimental methodology that was developed to validate imaging sequences for use in diffusion and DCE-MRI experiments respectively. To enable comparison between the DCE-MRI derived gadolinium concentration and a highly accurate analytical measurement, inductively coupled plasma mass spectrometry (ICP-MS) equipment was validated in subchapter 2.4.

2.2 The Apparent Diffusion Coefficient

2.2.1 Introduction

The interaction between an applied linear magnetic field gradient and a precessing water proton spin introduces a displacement dependent phase shift which makes possible measurement of molecular self-diffusion and convection. Observing restricted or spatially dependent diffusion in oncology places a requirement that the precise period of time that diffusion is being observed can be accurately quantified. The pulsed gradient spin echo method, as implemented by Stejskal and Tanner [76] (PGSE) applies a field gradient in short pulses, enabling the time during which the diffusion process is being observed to be precisely defined. Due to the low degree of compartmentalisation present in pure fluids (such as an ice water phantom) the relaxation function of the water molecules can be described by a Debye form. The Stejskal-Tanner pulsed gradient spin echo formalism enables the diffusion coefficient of proton spins to be determined from:

$$[26] \quad S = S_0 e^{-bD}$$

Where S represents the signal intensity in the presence of a diffusion sensitizing gradient with specific b-value represented by b (s/mm²). S₀ represents the signal intensity in the absence of a diffusion sensitising gradient and D the diffusion coefficient of spins (mm²/s). The above methodology allows the diffusion coefficient to be determined in the presence of pulsed gradients with differing b values where b is defined as $b = \gamma^2 G^2 \delta^2 (\Delta - \delta/3)$; γ (a constant) represents the gyromagnetic ratio of the hydrogen nucleus (42.6 MHz T⁻¹), δ the time of application of the diffusion sensitising gradient (ms), Δ the time interval between the application of the first and second gradients (ms) and G the gradient strength (mT/m). Of interest in pulsed gradient experiments is the “effective diffusion time”, purported to measure the time available for proton spins to undertake translational motion.

The impeded motion of a water molecule in the presence of cell membrane boundaries reduces its diffusion coefficient due to complete re-phasing of those spins unmoved at the time of application of the second gradient pulse. Thus, the reduced diffusion coefficient can be used for inference of cell density and membrane permeability [77]. The linear relationship between the root mean square displacement of a proton spin and the “effective diffusion time” is contravened for anomalous diffusion. This would be in evidence in a PGSE experiment from poor fitting to experimental data of the Debye form model. The effects of anomalous diffusion are reported to be evident in intracellular processes such as intracellular water diffusion.

2.2.2 Materials and Methods

Validation of diffusion sequences has been performed with a number of different test phantoms [78] at room temperature. These methods do not account for the temperature dependence of diffusion and as such are inadequate for accurate validation

of diffusion sequences. The validation of diffusion sequences was performed with an ice water phantom. Maintaining the ice water at a temperature of approximately 0°C should negate the confounding effect of temperature upon the diffusion coefficient.

2.2.2.1 Stejskal-Tanner Diffusion Sensitised Spin Echo Pulse Sequence

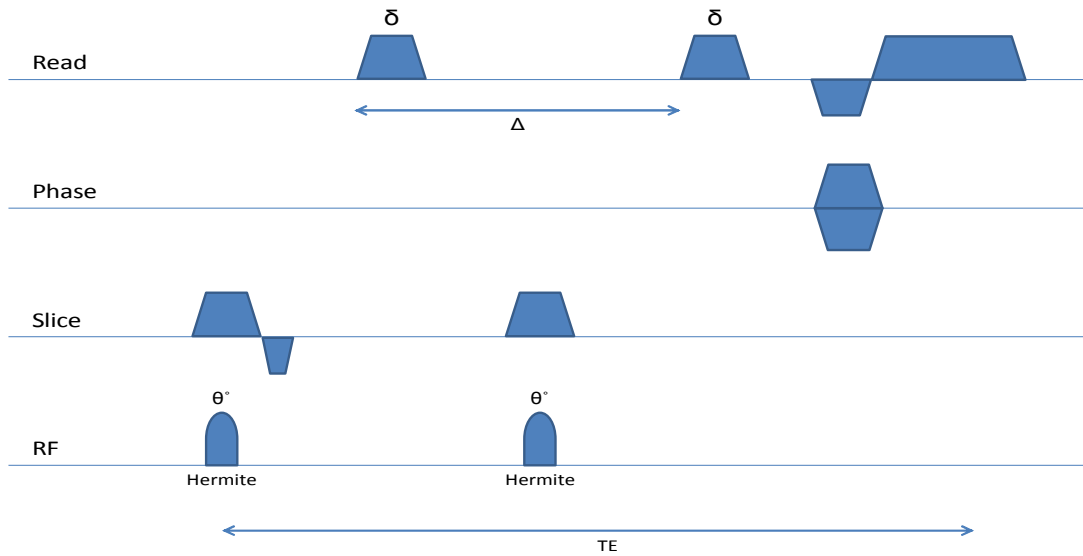


Figure 12: the above figure illustrates the Stejskal-Tanner spin echo pulse sequence.

2.2.2.2 Filling k Space in the Stejskal-Tanner Diffusion sensitised spin echo sequence

The lines of k space are acquired sequentially with a single line acquired per repetition time (TR). After the slice select and 90° Rf pulse the k space vector is at the centre of k space. The strong negative phase encoding gradient moves the trajectory to the lower bound of k space. The positive frequency encoding gradient subsequently applied moves the trajectory to the lower right corner of k space. The 180° pulse and slice select gradient moves the trajectory to the opposite location (in the upper left corner of k space). The positive frequency encoding gradient then moves the k space trajectory to the right through k space. This is illustrated in figure 13 below.

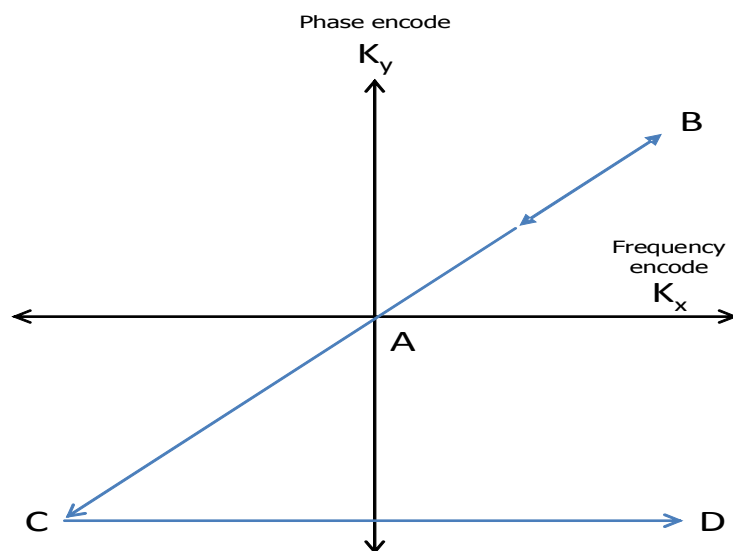


Figure 13: the above figure illustrates the k space trajectory for the diffusion sequence.

2.2.2.3 Temperature Dependence of Diffusion

The diffusion of water molecules is a temperature dependent property which can be modelled by an Arrhenius activation law [78]:

$$[27] \quad D = D_{\infty} e^{-\frac{E_A}{KT}}$$

Where above T represents the absolute temperature (K), E_A the activation energy for translational diffusion of the water molecules (J), K Boltzmann's constant ($1.38 \times 10^{-23} \text{ JK}^{-1}$) and D_{∞} the diffusion coefficient in the limit of infinite temperature. Equation 27 illustrates that increases in temperature will result in concomitant increases in the diffusion coefficient of water molecules. Controlling for temperature changes in a validation experiment is of importance to ensure that diffusion coefficients representative of the solution under study rather than gradient induced temperature changes are measured. Fitting the ADC as a function of temperature to a Speedy-Angell power-law produces the equation shown below [79]:

$$[28] \quad D = D_0 \left[\left(\frac{T}{T_s} \right) - 1 \right]^y$$

A plot of the diffusion coefficient of water as a function of temperature, represented by equation 28, is shown in the results section.

2.2.2.4 Ice Water Phantom

The use of an ice water phantom for ADC validation (*Tom Chenevert private communication*) enables the error associated with the temperature dependence of diffusion to be minimised, as the phantom is maintained at approximately 0°C . This method has been performed in clinical studies [80]. The transfer of this method for use in a preclinical scanner encounters challenges due to the narrow bore size encountered. Validation measurements were performed on the Bruker preclinical 7T magnet on repeated days using the same sequence to determine the diffusion coefficient of ice water. A schematic illustration of the phantom is shown below:

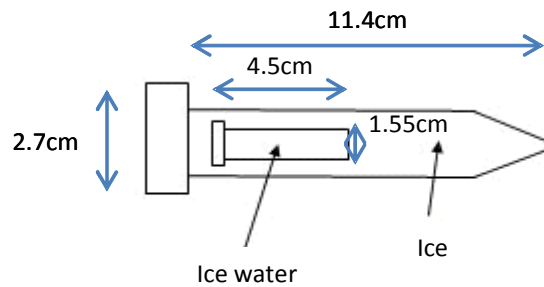


Figure 14:-the ice water phantom consists of an inner capsule of ice water and an outer capsule of ice to maintain the ice water at approximately 0°C ($\pm 0.1^{\circ}\text{C}$). All dimension measurements have an error of $\pm 0.1 \text{ cm}$.

The temperature of the ice water was recorded before and after each scan with a mercury thermometer to determine any temperature changes occurring inside the bore of the magnet.

2.2.2.5 Diffusion Sequence Details

The sequence employed (as shown in figure 12) utilised a 2.56 x 2.56 cm FOV with a 128 x 128 matrix size and 15 slices of 0.6cm slice thickness (0.2 mm x 0.2 mm x 6 mm voxel size). The TR/TE was 2250/20 ms with b values of 150,500 and 1000s/mm² ($\delta=4$ ms and $\Delta=9$ msec); total scan time = 14mins 24secs. Diffusion encoding gradients were applied along the frequency encoding direction. This sequence acquires a line in k space sequentially with one line acquired per repetition time with increasing phase encoding gradient strength for each line acquired (negative to positive intensity) as discussed.

2.2.2.6 Simulation of Diffusion Encoding Experiment

The mono exponential decay of the signal in the presence of increasing b values can be simulated using synthetic data. To obtain a starting value for the subsequent optimisation a linear fit to the data can be obtained by taking the logarithm and transposing the equation such that the diffusion coefficient is interpreted as the gradient of the straight line plot. To generate synthetic data an S_0 of 1 was used with b values of 150,500 and 1000 s/mm².

2.2.2.7 Bruker Scaling Factors

To achieve the maximum dynamic range on a display window the data files produced by *Paravision 5.0* are each scaled. The values for the scaling are available in the supplementary files contained within a particular scan folder. These scaling factors are applied to the data to enable computations to be performed.

2.2.2.8 Experimental Protocol

The experimental protocol for the ice water phantom experiment is as follows:-

1. Preparation of ice water phantom by placing crushed ice into a plastic capsule and allowing ice in a smaller capsule to melt until all is in a liquid state.
2. Measure the temperature of the water in the smaller capsule with a mercury thermometer and insert this into the larger capsule and cover with ice. Any ice water phantoms which returned a temperature greater than $0^{\circ}\text{C} \pm 0.5^{\circ}\text{C}$, measured using a mercury thermometer, were excluded from further analysis.
3. Place capsule into the magnet.
4. T_2 sequence to localise the phantom in the magnet.
5. The diffusion sequence is run as detailed above.

6. Once sequence has run remove the capsule.
7. Data is transferred from the desktop computer to an offline workstation where it is analysed in Matlab.
8. A region of interest (ROI) is placed in the lowest b value diffusion weighted image (b=150mm²/s) avoiding any ice and an ADC map is calculated based upon this ROI. Regions of interest were drawn over all slices containing ice water. The mean value is computed by summing ADC values on a voxelwise basis and dividing by the total number of voxels.

This experiment was performed on different dates over a period of three months and the mean ADC value determined for each phantom on each date. The whole experiment takes approximately 45 minutes to perform.

2.2.2.9 Post processing of data

A starting value for the ADC on a voxelwise basis is determined by taking the log of equation 26 to produce

$$[29] \quad D = \frac{1}{b} \ln\left(\frac{S_0}{S}\right)$$

A linear fit of a vector of ln(S) (y axis) against a vector of b values (x axis) allows D (mm²/s) to be calculated.

$$[30] \quad D = -m$$

Where m represents the gradient of the straight line fit. This value can in turn be used as a starting value for the D in the subsequent non-linear curve fitting. In the non-linear curve fitting process the vector of signal intensity, vector of b values and starting values for the ADC as obtained from the linear fit are introduced into a non-linear least squares fitting algorithm (Levenberg-Marquardt) in Matlab (*lsqcurvefit*). R² values are computed on a voxelwise basis for both the linear and non-linear fitting routines. The effect of Rician noise upon magnitude data acquired in diffusion imaging is well documented [81]. To obviate the effect of Rician noise a signal to noise ratio (SNR) threshold was determined from the experimental data with those voxels falling below the threshold of 3 x SNR omitted from the subsequent analysis.

2.2.3 Results

2.2.3.1 Simulation of Diffusion Encoding Experiment

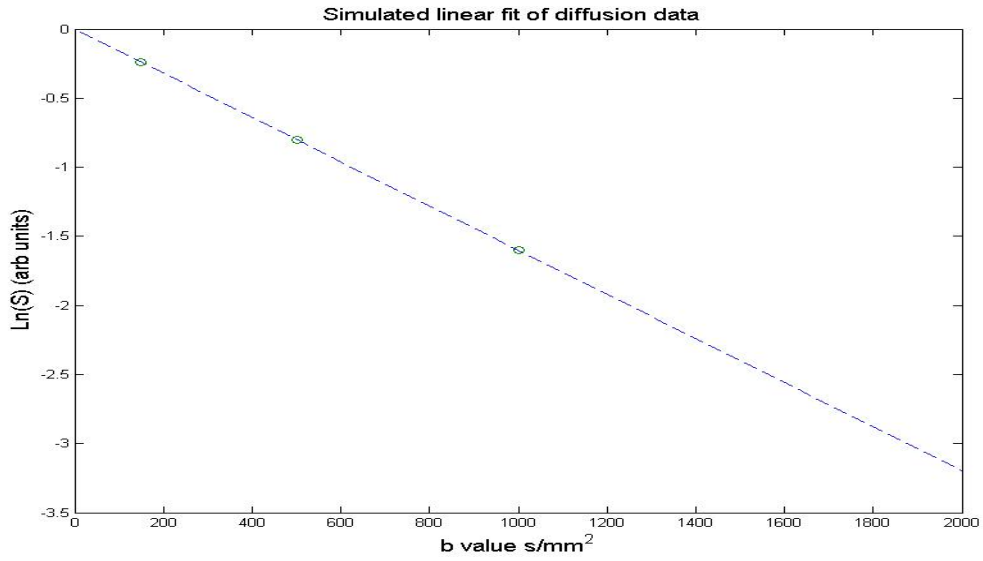


Figure 15: the simulated data above illustrates the straight line fit from which a starting estimate for the diffusion coefficient can be obtained.

The data points are indicated by circles. S_0 was set equal to 1 in the simulation.

The subsequent non-linear least squares curve fitting fits the monoexponential decay as presented in equation 26. This is simulated below:

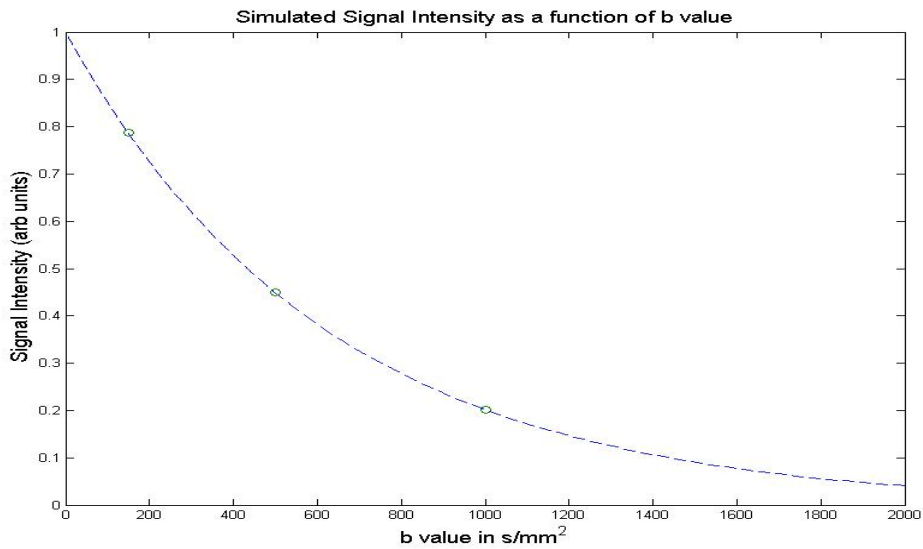


Figure 16: the mono exponential decay obtained as a function of b value is presented with the data points illustrated by circles.

The experimental results obtained were compared against those obtained with a similar methodology at different sites to determine their agreement. The figure below illustrates the results obtained on the Manchester preclinical Bruker 7T with horizontal lines indicating the maximum and minimum values found in the literature for an ice water phantom experiment.

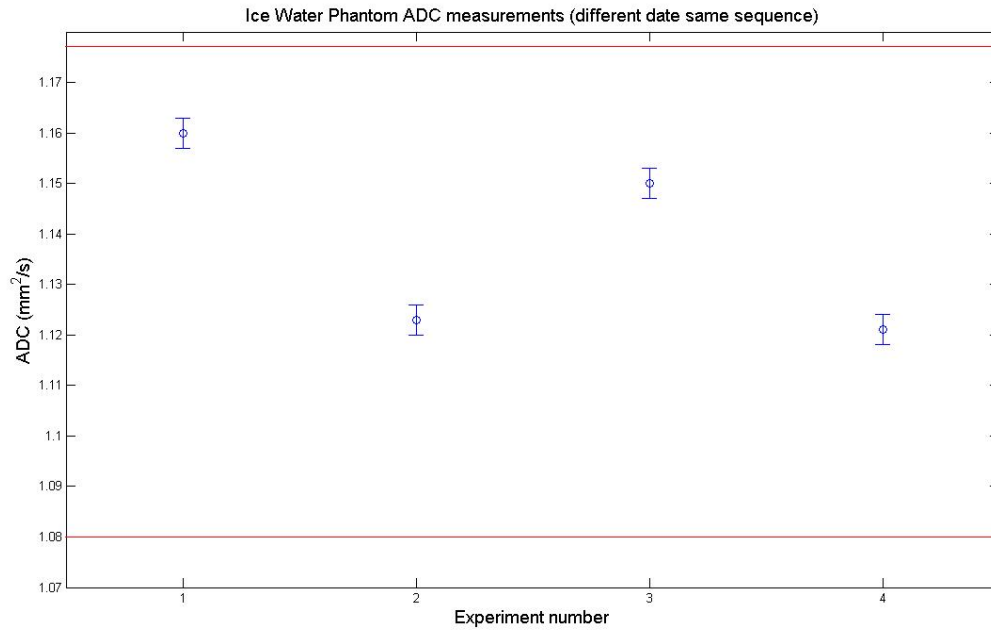


Figure 17: the ice water phantom ADC measurements obtained across four different dates are plotted as blue circles with the maximum and minimum values obtained from the literature plotted as red lines. Error bars represent standard deviations taken over all voxels of each scan.

The volume of the cylinder containing the ice water is approximately 8.49cm^3 which implies that there are a maximum of approximately 353 imaging voxels inside the cylinder from which ADC measurements can be made.

2.2.3.2 7T Phantom Data Compared to International Centres

The comparison of the values for the diffusion coefficient of ice water against those obtained at different imaging centres is presented below.

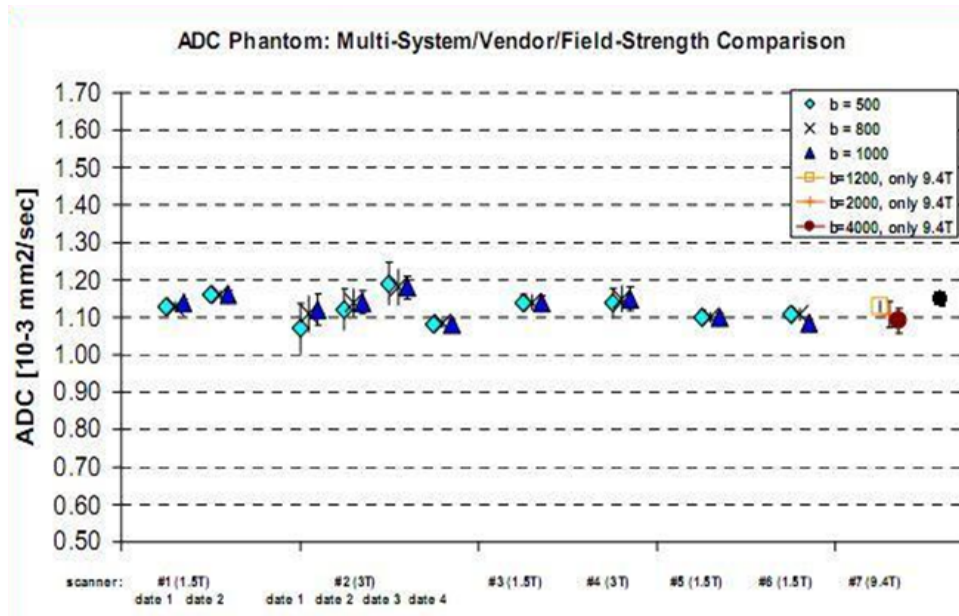


Figure 18: the figure above illustrates the 7T Preclinical scanner ADC values obtained, compared against other imaging centres (black point at far right). It is important to note that the other values were obtained from clinical scanners [82]. The abscissa represents ice water phantom experiments performed at different field strengths, with different b values and on repeated dates.

2.2.3.3 Temperature Dependence of the Diffusion Coefficient of Water

Inserting the constants D_0 ($1.635\text{mm}^2/\text{s}$) and T_s (215.05K) and for a γ of 2.063 into equation 28, the diffusion coefficient of water at 273.15K is approximately $1.1\text{mm}^2/\text{s}$. The figure below illustrates the temperature dependence of diffusion from zero to thirty degrees.

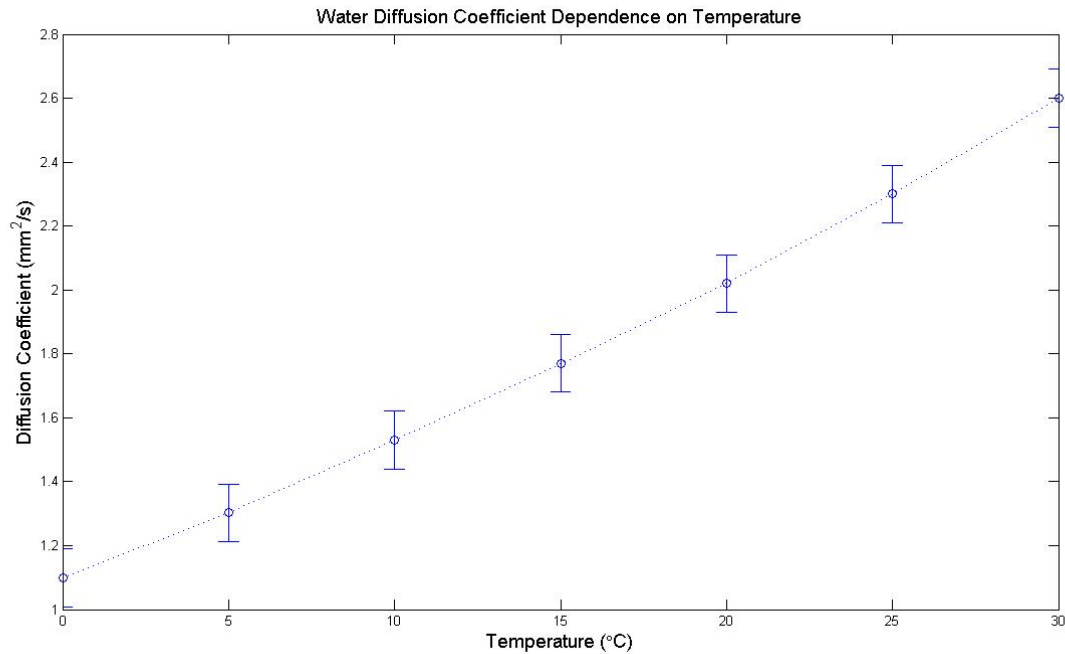


Figure 19:- the diffusion coefficient of water as a function of temperature is plotted with error bars representing the propagation of error due to the uncertainty in the model parameters.

2.2.4 Discussion

The results presented indicate that the ice water phantom enables the temperature dependent effects of diffusion to be largely reduced in a preclinical MRI scanner, producing ADC values in agreement with that one would anticipate from theory. As discussed, the impact of gradient induced temperature changes upon the diffusion coefficient of water is a confounding factor in the validation of diffusion sequences. The driving of currents through the gradient coils results in ohmic heating (the gradient strengths required to produce b values of 1000, 500 and 150 s/mm^2 are 303mT/m, 214.5mT/m and 117.48mT/m respectively). The dissipated power typically produced by the switching of a gradient coil is of the order of 10 kilowatts. If all of the thermal energy generated is converted into heating the water sample, then thermodynamics indicates a temperature change of approximately 0.04°C for a single gradient switching process (assuming the specific heat capacity of water at 25°C to be $4.19 \text{ Jg}^{-1}\text{K}^{-1}$ and a switching speed of $122\mu\text{s}$). As the gradients are cooled by a water cooling system the thermal energy generated will be largely negated. The large currents required (circa 200A) to generate magnetic field gradients may result in small but undesirable temperature increases in the bore of the magnet throughout the duration of a scan.

There are additional confounding factors which can impact upon the diffusion experiment such as magnetic field gradient inhomogeneity. Such variations can result in a spatial dependency in the b value calculated over the imaging volume. Correction for effects of field inhomogeneity can occur if the ADC of a sample is known to high accuracy. Subsequent post processing can determine the effective b value experienced by the spins in the phantom and the gradient strength which would produce such a b value corrected for to determine the extent of magnetic field inhomogeneity. The Gibbs phase rule indicates that there is one degree of freedom for this system (2 phases, 1 component); that of the temperature. At constant pressure in a two phase system temperature is constant. However, convective effects at the interface between ice water and external air may impinge upon the measured ADC values. In addition to this, small pieces of ice present in the ice water represents a source of error which will impinge upon the measured diffusion coefficient, if not removed from the analysis. Obviating this error was achieved by ensuring no ice crystals are present in the ice water on the T_2 weighted image in addition to drawing regions of interest for ice water exclusively on the lowest b value image.

2.3 Measuring the Longitudinal Relaxation Time (T_1)

2.3.1 Introduction

The interaction of hydrogen nuclei with an applied magnetic field is the fundamental physical phenomenon responsible for the generation of an observable signal in the NMR experiment. To fully describe the NMR experiment, a combination of both classical and quantum physics is employed with certain aspects of the theory better explained by the former or the latter [83]. A fundamental review of the theory can be found in numerous journals and textbooks [84]. In brief, all elementary particles have an intrinsic spin quantum number s , which can have values of $n/2$ for any non-negative integer n . In ^1H NMR we are interested in the proton which has a spin of $1/2$. The spin angular momentum is defined as:

$$[31] \quad p = \hbar \sqrt{s(s+1)}$$

This for a proton is equal to

$$[32] \quad p = \hbar \sqrt{3/4}$$

The z component of the spin angular momentum is defined as

$$[33] \quad p_z = \hbar s_z \text{ for } s_z = -s, -s+1, \dots, s-1, s$$

Or in our case for a proton

$$[34] \quad p_z = \pm \hbar/2$$

This results in a magnetic moment

$$[35] \quad \mu = \gamma p_z = \pm \gamma \frac{\hbar}{2}$$

In the absence of an applied magnetic field the two possible states of a protons spin angular momentum have equal energies (degenerate). However, when the proton is placed in a static external magnetic field B_0 , the z component of the spin magnetic moment has eigenstates which are parallel or anti-parallel to the external magnetic field (Zeeman splitting). These two states acquire different energies:

$$[36] \quad E = -\mu B_0 = \frac{\pm \hbar}{2} \gamma B_0$$

An excess of spins in the low energy level aligned with the magnetic field is responsible for the NMR signal.

As a simplification the magnetic moment associated with each proton spin can be combined to produce one net magnetisation vector M . Perturbation of this vector from its equilibrium value parallel to the static B_0 field is achieved with a 90° radiofrequency (rf) pulse obtained by applying an effective field B_1 orientated perpendicular to the B_0 field. The frequency of the applied rf pulse is related to the energy difference between the low and high energy states of the proton by the Larmor frequency:

$$[37] \quad \omega_0 = \Delta E / \hbar = \gamma B_0$$

Absorption of the rf energy stimulates transitions between the low and high energy states. This can be classically interpreted as the M vector tilting away from the B_0 vector while precessing with frequency ω_0 . The M vector can now be decomposed into a component parallel to B_0 and two components perpendicular (M_x and M_y). Continued application of the rf pulse such that the M vector is rotated by 90° results in an equal spin population in the two energy states. The M vector will return to its equilibrium value parallel to the B_0 field by a process known as relaxation. The parallel and perpendicular components of M relax by different processes with the perpendicular component relaxing by spin-spin or T_2 relaxation, whilst the parallel component relaxes by spin lattice or T_1 relaxation [85].

The application of a 90° rf pulse rotates the net magnetisation vector into the transverse plane. The system will return to its lowest energy state (M_0 parallel to B_0) through the dissipation of energy to the surrounding environment or “lattice”. To release energy to the lattice the proton must encounter a magnetic field which fluctuates at ω_1 to enable coherent spontaneous emission to occur [86]. The random motion of nearby particles will create local magnetic field fluctuations [84]. This energy release is termed T_1 , the enthalpic or spin lattice relaxation time. The rate at which this relaxation occurs is determined by the local distribution of frequencies due to magnetic field fluctuations. Protons move at different rates in differing chemical environments affecting the local magnetic field distribution. As an example, water molecules translate and rotate in liquid generating a magnetic field that fluctuates at a higher frequency than the Larmor frequency. Within tissue however, protons move at a slower rate producing fluctuations closer to the Larmor frequency allowing them to release energy at a faster rate. The T_1 of a substance is the time required for the M_z component to return to 63% ($1 - e^{-1}$) of its equilibrium value. Bound molecules as are present in solids tumble at much lower frequencies; both free water and solids have slow T_1 relaxation rates and high T_1 values. The relaxation of M_z towards its thermal equilibrium value M_0 can be phenomenologically modelled by the first Bloch equation:

$$[38] \quad \frac{dM_z}{dt} = \frac{M_0 - M_z}{T_1}$$

With solution

$$[39] \quad M_z(t) = M_0(1 - e^{-t/T_1})$$

Once can verify from these equations that the time taken for the magnetisation to return to 63% of its equilibrium value is T_1 . Accurate validation of the techniques used for measuring T_1 is of fundamental importance due to its temperature and field strength dependence. Robust validation was performed to ensure that the sequences employed were able to calculate T_1 to a high accuracy. The longitudinal relaxation time can be measured by different methods which are reviewed in the literature. The improved temporal resolution available with the saturation recovery experiment is an advantage over inversion recovery. This however occurs at a cost as the dynamic range is reduced by one half, resulting in a decrease in the signal to noise ratio.

A single voxel spectroscopic measurement is performed by spatially constraining the origin of the signal by gradient selection of three orthogonal slices. The reduced gradient strength minimises any possible effects on T_1 due to spin dephasing. A “gold-standard” for T_1 measurement would be a spectroscopic measurement (no imaging gradients). To obtain voxelwise T_1 measurements of tumour an imaging experiment is performed. This was performed by means of saturation recovery. Performing accurate volumetric measurements of T_1 in an in vivo study with contrast enhancement enables contrast concentration to be gauged on a voxelwise basis longitudinally through time due to its impact upon the relaxation time of water proton spins.

2.3.2 Nuclear Spin Relaxation Mechanisms

DCE-MRI exploits the decrease in the spin-lattice relaxation time induced by contrast media. An increase in the relaxation rate is termed “positive enhancement”, as the signal intensity is increased (short TE/TR of sequence; signal fully detected) by dipole-dipole interactions between contrast media and hydrogen nuclei. Similarly the relaxation rate can be decreased and “negative enhancement” whereby the signal intensity decreases (long TE/TR; signal not detected) due to “spin-spin” interactions between nuclei achieved.

Contrast in MRI is dependent upon both intrinsic and extrinsic factors [87]. Intrinsic factors such as the nuclear (T_1 and T_2) relaxation times and respectively, proton density, flow, diffusion and perfusion, will all affect image contrast. Extrinsic factors include the pulse sequence (spin echo or gradient echo), timing parameters of the pulse sequence and the strength of the magnetic field. Paramagnetic contrast media interact with hydrogen nuclei causing relaxation from a high to a low energy state, through interactions between neighbouring magnetic dipoles. This dipole-dipole interaction can be explained by two mechanisms, an inner and an outer sphere contribution.

Inner sphere relaxation depends upon chemical exchange between water molecules and electronic spins, where a water molecule in contact with the spins leaves a coordination sphere of the paramagnetic centre and is replaced by another

molecule. This process of exchange results in the transfer of the paramagnetic effect to the totality of the solvent as the water molecules exchange between two sites (the paramagnetic centre and the rest of the water reservoir). The time for which the water molecule is in the first coordination sphere of the paramagnetic centre is known as the residence time τ_M . The relaxation time of protons which are located in the first coordination sphere of the metal is known as T_{1M} . The overall contribution of the inner sphere mechanism to the relaxation time of the water molecules is given by :-

$$[40] \quad R_1^{IS} = fq \frac{1}{T_{1M} + \tau_M}$$

In the equation shown above, f represents the relative concentration of the paramagnetic complex and of the water molecules; q equals the number of water molecules in the first coordination sphere of the complex. In figure 20 below τ_R represents the rotational correlation time (which characterises the reorientation of the vector between Gd^{3+} and the water molecule protons), r represents the distance between coordinated water protons and unpaired electron spins and τ_M the water molecule residence time. The figure shown below illustrates the concepts of the inner sphere relaxation mechanism [87]:-

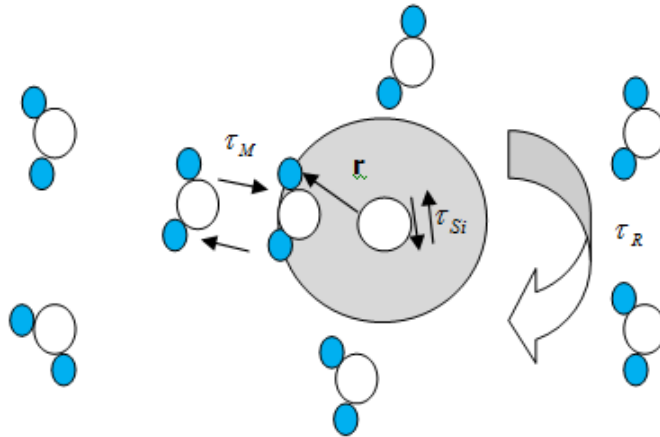


Figure 20: the above figure illustrates the interaction between the paramagnetic complex and water protons.

In the above figure τ_{Si} (where $i=1, 2$ corresponds to longitudinal and transverse relaxation respectively) represents the relaxation time of the electron. The outer sphere relaxation mechanism is the second contribution to the paramagnetic relaxation. The long distance dipolar interaction between the spin of the paramagnetic substance and the water proton spins

induces relaxation. This mechanism is modulated by the translational correlation time (τ_D) which takes into account the relative diffusion of the paramagnetic centre and the solvent molecule, in addition to their distance of closest approach (d) and the relative diffusion of the paramagnetic centre (D).

$$[41] \quad \tau_D = \frac{d^2}{D}$$

The relaxation contribution from the magnetic dipole-dipole interactions between protons is given in the equation below:

$$[42] \quad \frac{1}{T_1} = G \sum_i P_i \left(\frac{\tau_{ci}}{(1 + \omega_0^2 \tau_{ci}^2)} + 4 \frac{\tau_{ci}}{(1 + 4 \omega_0^2 \tau_{ci}^2)} \right)$$

Where in the above

$$[43] \quad \sum_i P_i = 1$$

τ_{ci} represents the various correlation times (dependent upon the rates of molecular motions), G is an interaction constant and ω_0 represents the Larmor frequency. The dipole-dipole interaction depends upon the distances between protons in a pair, the orientation of the proton pair in the magnetic field (B_0) and on the time dependence of all of these quantities. The proton-electron spin dipole-dipole interaction and isotropic proton-electron spin exchange are combined in the equation shown below, to detail the respective contributions to proton spin relaxation, in the presence of a contrast agent [88]:

$$\frac{1}{NT_1} = \left(\frac{4}{30} \right) S(S+1) g^2 \beta^2 \gamma_I^2 \left(\frac{n_h}{N_p} \right) r^{-6} [3 \tau_c + 7 \tau_c (1 + \omega_s^2 \tau_c^2)^{-1}] + \left(\frac{2}{3} \right) S(S+1) A^2 \hbar^{-2} \left(\frac{n_h}{N_p} \right) [\tau_e (1 + \omega_s^2 \tau_e^2)^{-1}]$$

$$[44]$$

In the above equation, indexes I and S refer to proton and electron spins, respectively; r, the ion-proton internuclear distance; A, the spin exchange constant; τ_c and τ_e , the correlation times for dipolar and spin exchange interactions respectively; n_h the number of protons in the hydration sphere of the ion; N_p the molar concentration of water protons in the solution and N , the molar concentration of paramagnetic ions. Additional symbols have their usual meanings.

2.3.3 Materials and Methods

2.3.3.1 PRESS Sequence details

A PRESS (point resolved spectroscopy) single voxel spectroscopic sequence with variable repetition time $TR = 50, 100, 200, 400, 800, 1600, 3200, 5000\text{ms}$ and $TE = 10\text{ms}$, number of averages = 10 and a total scan time for the TR of 5 sec of 55 sec ($10 \times 5 + 5$ (dummy scan) = 55 secs) was performed.

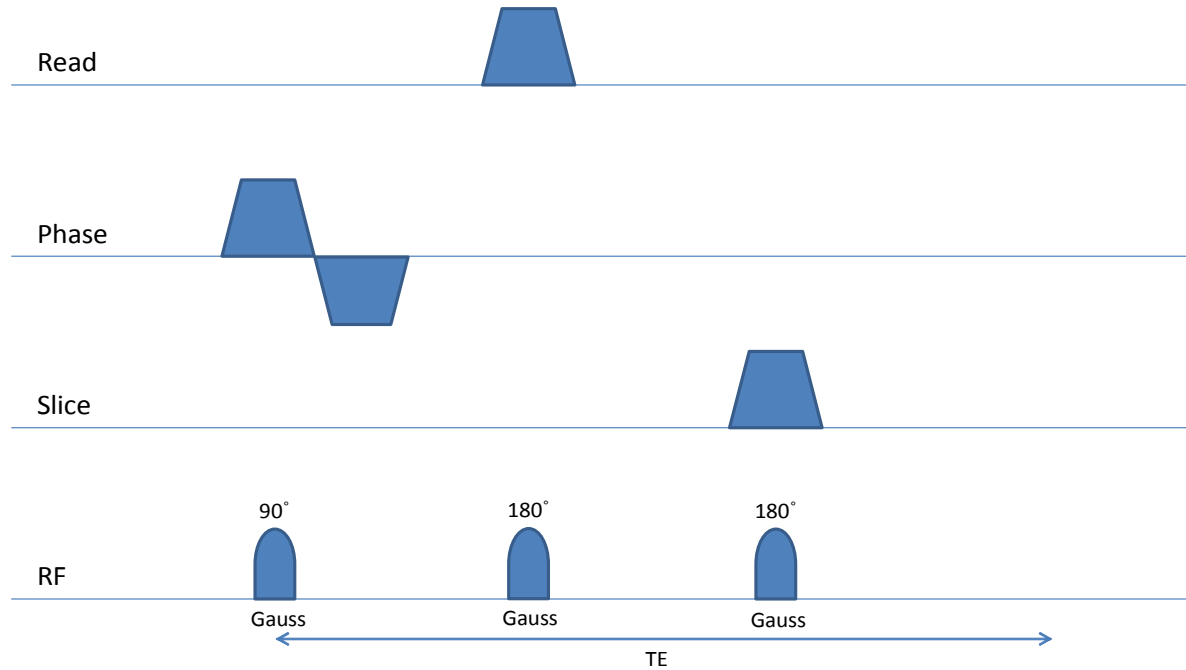


Figure 21: the above figure illustrates the PRESS sequence performed in the experiment.

2.3.3.3 Simulation of Saturation Recovery Curve for Spectroscopic Saturation Recovery Experiment

The simulation of the saturation recovery for phantoms of differing T_1 values representative of physiologic values one would encounter in vivo was performed to determine the optimum sequence parameters. The range of T_1 values in an in vivo experiment is between 600 and 1600 ms. A T_1 of 1000 ms was simulated according to equation 40.

2.3.3.4 PRESS Saturation Recovery Experiment 1

The PRESS sequence as detailed above was performed on phantoms of differing concentrations of gadopentetate and deionised water to determine the accuracy of the sequence.

2.3.3.5 Saturation Recovery Imaging Sequence

The saturation recovery experiment was performed using a multishot RARE (Rapid Acquisition with Refocused Echoes) 3D imaging sequence with variable repetition time. This is a CPMG (Carr-Purcell-Meiboom-Gill) sequence, generating multiple

spin echoes with slice selective rf pulses. A 90° slice selective rf pulse is applied concurrently with a slice selection gradient. A slice rephasing gradient is applied after the excitation pulse to refocus spins. A prephasing readout gradient is applied in the frequency encode direction to centre the echo in the first readout window. Subsequent to this, an identical readout gradient lobe is applied to frequency encode each echo of the echo train. A phase encoding gradient is implemented after each refocusing pulse. Assignment of phase-encoding values to the echoes in the echo train determines the image contrast and influences the extent of image artefacts. The saturation recovery experiment is performed by varying the repetition time of the sequence. The sequence used a 2.56 x 2.56 cm FOV with 128 x 64 matrix size and 15 slices of 0.6cm thickness, TR/TE= 119.349,1000,2000 and 5000/8.764 ms with a RARE factor of 13. As illustrated in the pulse sequence diagram below, each echo is separately phase encoded and the phase encoding is incremented within one echo train to accelerate the acquisition.

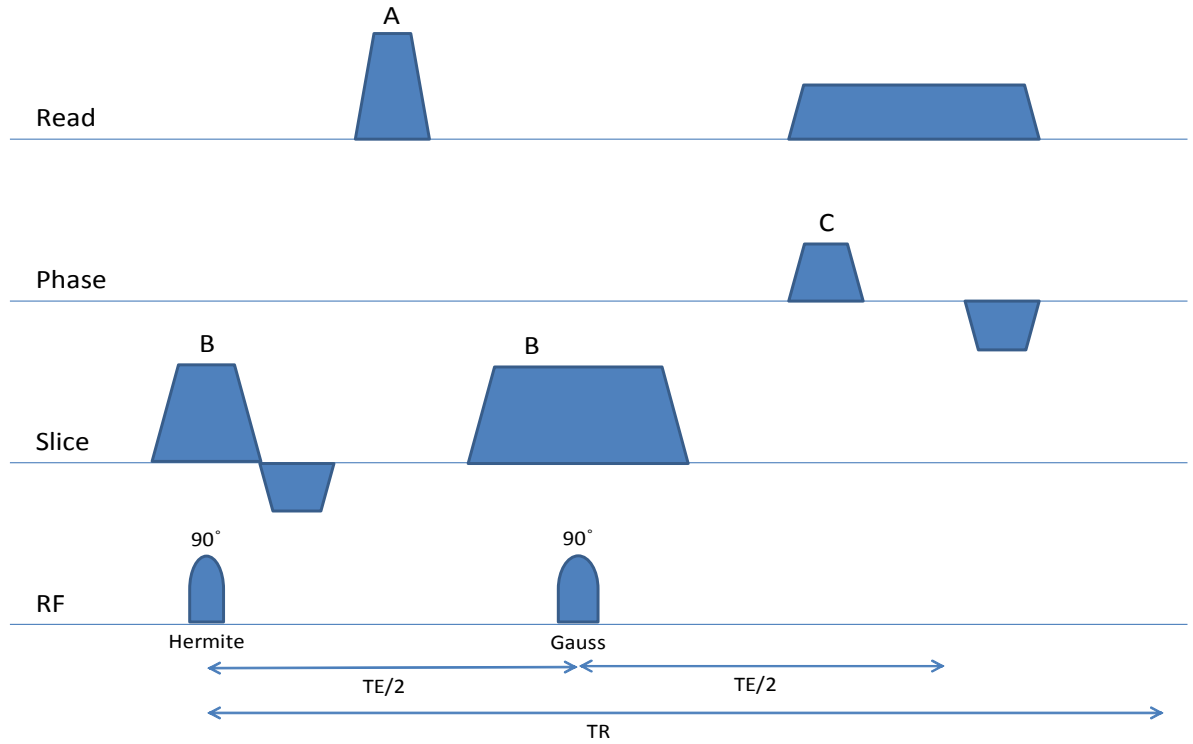


Figure 22: the pulse sequence for the RARE-VTR sequence is illustrated above. “A” represents the slice refocusing duration which determines the minimum slice thickness and the minimum FOV in the read direction. “B” represents the slice spoiler required to remove residual FID signals from the refocusing pulses. “C” represents the phase gradient which is subsequently rewound to obtain a coherent superposition of all signal components with non-180° refocusing pulses.

The echo time (time between centres of refocusing pulses) was 8.764ms and the effective echo time (delay between the excitation pulse and central phase-encoding step) 43.82ms. To obtain T₁ weighting in an image earlier echoes in the echo train are used to sample the central k-space data such that TE_{eff} takes its minimal value i.e. TE_{eff} = t_{esp} with later echoes used to fill the remainder of k-space. The mathematical relationship between these parameters is illustrated below:

$$[45] \quad I_n \propto M_0 \left(1 - F e^{\frac{-T_D}{T_1}} \right) e^{\frac{-TE_n}{T_2}}$$

Where n is the “nth” echo time,

$$[46] \quad T_D = TR - 2N_\tau$$

Where represents the total number of refocusing pulses, τ the time between the excitation pulse and the first refocusing pulse and

$$[47] \quad TE_N = 2n \tau$$

Is the “nth” echo time for and F represents a geometric series that describes the intensity of multiple echoes repeated by 2τ . It can be inferred from equation 45 that long echo times will increase the T_2 weighting of the image. The number of echoes used in this sequence (10) was a compromise between temporal resolution and reducing the T_2 weighing of the sequence.

2.3.3.6 Stimulated Echoes in a CPMG sequence

To minimise the effect of stimulated echoes in the RARE-VTR experiment crusher gradients were applied along the slice select direction (“B” in figure 22 above).

2.3.3.7 K space Filling for the RARE-VTR Sequence

The RARE factor of 13 as used with this sequence indicates that each cycle of the sequence has 13 phase encoding steps (with the sequence looped until the desired number of phase encoding steps is obtained). The first excitation fills the first line in k space; the second line is filled by the second excitation and so on until all of k space has been filled.

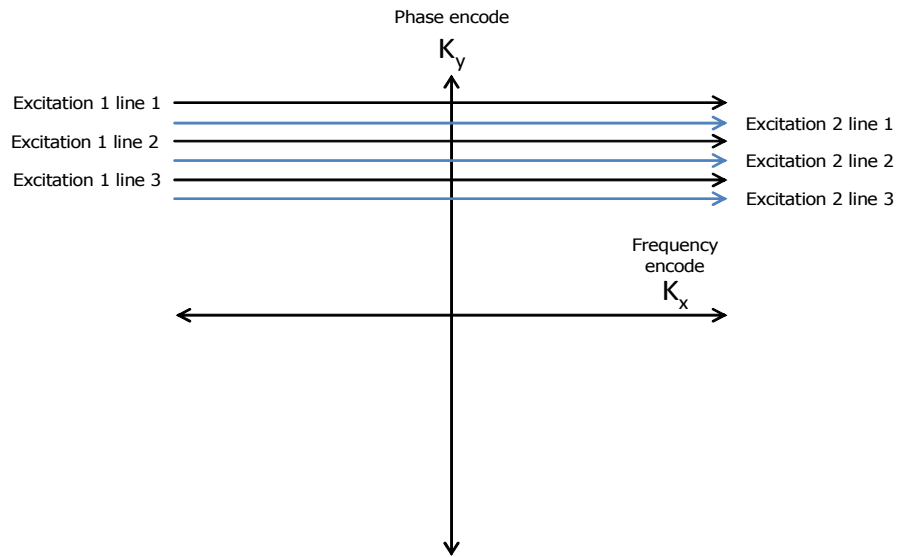


Figure 23: the above figure illustrates the trajectory of the k space vector with a line in k space filled from each excitation. The black line represents the first excitation and the blue the second.

The time taken to fill the entirety of k space is thus reduced by a factor of 13 improving the temporal resolution of the sequence.

2.3.3.8 Simulation of Saturation Recovery Curve for Imaging Saturation Recovery Experiment

The simulation of a saturation recovery experiment as shown below illustrates the recovery to equilibrium of the magnetisation for the RARE-VTR sequence with four TR's.

2.3.3.9 RARE-VTR Experiment 1

The RARE-VTR sequence as detailed above was performed on phantoms of differing concentrations of gadopentetate to determine the accuracy of the sequence.

2.3.3.10 RARE-VTR Experiment 2

To determine the stability of the R_1 values produced by the sequence over time the sequence was repeated 15 times.

2.3.3.11 FLASH (Fast Low Angle Shot) Imaging Sequence

The high temporal resolution required to perform DCE-MRI studies cannot be obtained with the saturation recovery sequence discussed. Rapid calculation of the T_1 relaxation time can be obtained through use of variable flip angle gradient refocused imaging [89]. The mathematical description of the signal intensity obtained in such a sequence as a function of the applied rf pulse flip angle is presented below:

$$[48] \quad S(t) = S_0 \sin(\alpha) \frac{1 - e^{-TR/T_1}}{1 - \cos(\alpha) e^{-TR/T_1}} e^{-TE/T_2^*}$$

In the above equation, S represents the signal intensity as a function of time defined by TR (ms), T_1 the longitudinal relaxation time of the sample, α the flip angle of the rf pulse and S_0 the signal intensity prior to the application of the pulse (incorporates various factors including proton density and receiver gain).

$$[49] \quad e^{-TE/T_2^*}$$

The above term approaches 1 for the short TE and physiologic T_2^* one would encounter in vivo and as such is excluded from the model fitting. The flip angle at which the optimum signal intensity is obtained [90] shown below is known as the Ernst angle:

$$[50] \quad \cos(\alpha) = e^{-TR/T_1}$$

Solving the Ernst equation with the TR of 6.7ms and for a physiologic T_1 (1 sec) yields a flip angle for maximum signal intensity of 6.6° . The errors associated with the variable flip angle approach are reduced when three flip angles located on either side of the Ernst angle are selected. The FLASH sequence implemented had a FOV of 2.56×2.56 cm, matrix of 128×64 , TR/TE=6.7/2.4 ms, 15 slices and flip angles of 2.6° and 14° . For the dynamic sequence a single flip angle of 6° with the same imaging parameters was used. Transposing equation 48 enables a linear fit to be performed upon the data for a starting estimate of T_1 from equation 51 shown below:

$$[51] \quad \frac{S_i}{\sin(\alpha_i)} = E_1 \frac{S_i}{\tan(\alpha_i)} + M_0(1 - E_1)$$

Where

$$[52] \quad E_1 = e^{-TR/T_1}$$

This equation is the equation of a straight line where

$$[53] \quad y = mx + c$$

As such the T_1 value can be determined from

$$[54] \quad T_1 = \frac{-TR}{\ln(m)}$$

This T_1 value can be used as a starting value for the subsequent non-linear fitting process. The pulse sequence diagram for the FLASH sequence is presented below.

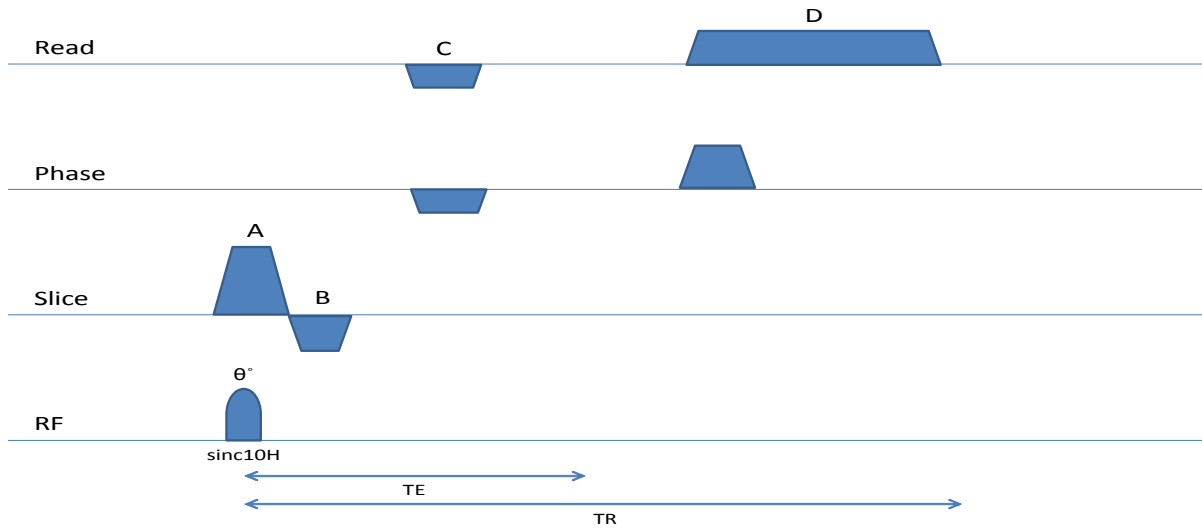


Figure 24: the above figure illustrates the pulse sequence diagram used for the FLASH sequence. “A” represents the slice spoiler used to remove incoherent components of the steady state signal which might generate interference artefacts. “B” represents the slice rephasing which determines the minimum TE, minimum slice thickness and the amplitude of slice rephasing. “C” represents the time for phase encoding which determines the minimum TE, minimum FOV and the amplitude of phase encoding/rewinding. “D” represents the read spoiler strength which adds to the effect of the slice spoiler.

2.3.3.12 K Space Filling for the FLASH Sequence

The simultaneous application of read and phase gradients results in translation from the centre of k space to the top left (from A to B) and subsequently followed by frequency encoding via the centre of k space to the top right (from B to C). This process is then repeated for different phase encode gradient strengths. A schematic illustration of the k space trajectory is shown below:

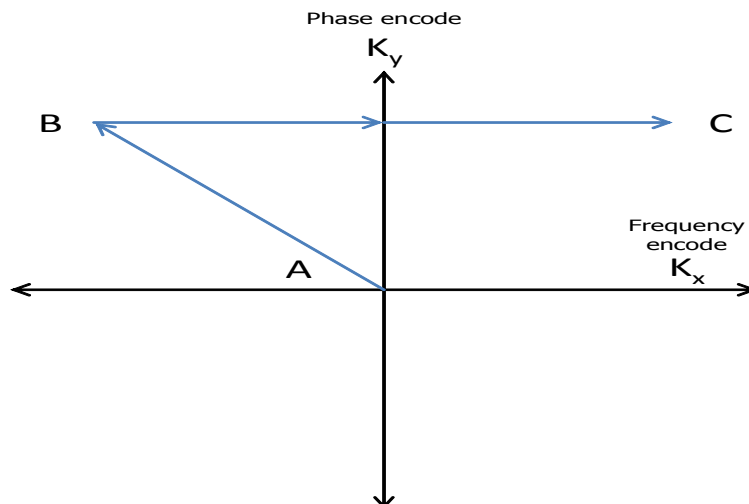


Figure 25: the above figure illustrates the k space trajectory for a FLASH sequence.

2.3.3.13 FLASH Experiment 1

Equation 48 was simulated for a TR of 6.7ms and a T_1 of 1000ms.

2.3.3.14 FLASH Experiment 2

The FLASH sequence as detailed above was performed on phantoms of differing concentrations of to determine the accuracy of the sequence.

2.3.3.15 Calculating Contrast Agent Concentration

The T_1 value can subsequently be converted into an R_1 value (sec^{-1}) representing the relaxation rate due to the identity between the two

$$[55] \quad R_1(t) \equiv \frac{1}{T_1}$$

The relaxation rate can be shown to be related to the contrast agent concentration by the linear relationship [56];

$$[56] \quad R_1(t) = R_{10} + rC_t(t)$$

Where the relaxivity of the contrast agent is represented by r ($4.85 \text{ mM}^{-1}\text{s}^{-1}$ for gadopentetate), R_{10} represents the relaxation rate in the absence of contrast agent and R_1 the relaxation rate after the administration of contrast. Thus the change in the relaxation rate from a baseline value can be used to compute the contrast agent (mM) in tissue. Thus if the baseline relaxation rate in voxel “i” of “N” voxels is known before and after contrast agent administration, the concentration can be determined over all “N” voxels of volume “V” (voxels of the same volume) at time “t” from

$$[57] \quad C_t(t) = \sum_{i=1}^N \left(\frac{R_{(i)t} - R_{(i)0}}{r} \right)$$

The amount of gadopentetate in units of mM can thus be compared to that obtained from ICP-AES by multiplying the above concentration by the volume within which it is contained.

2.3.3.16 Combination of errors

Error analysis upon measured concentrations was performed through use of the combination of errors formula. The linear relationship between relaxation rate and contrast agent concentration in conjunction with an assumed constant relaxivity of gadopentetate between scans enables the error in the relaxation rate to be deduced. Thus the error in the relaxation rate may be measured as:

$$[58] \quad \sigma_{R1} = r \sigma_C$$

Where σ_{R1} represents the error on the relaxation rate, r the relaxivity and σ_C the error on the measurement of the concentration of contrast agent administered in a phantom.

2.3.3.17 Additional Sources of Error

The error associated with inaccurate measurements of the concentration of gadopentetate used in the doping of phantoms is not a single source of error. Rician noise becomes a significant confound when the SNR ratio of an image becomes less than 3.

This is a similar confound as is encountered in diffusion MRI.

2.3.4 Results

2.3.4.1 PRESS Spectroscopic Saturation Recovery Simulation

The figure below simulates the saturation recovery experiment performed on a water phantom with a T_1 of 1 sec.

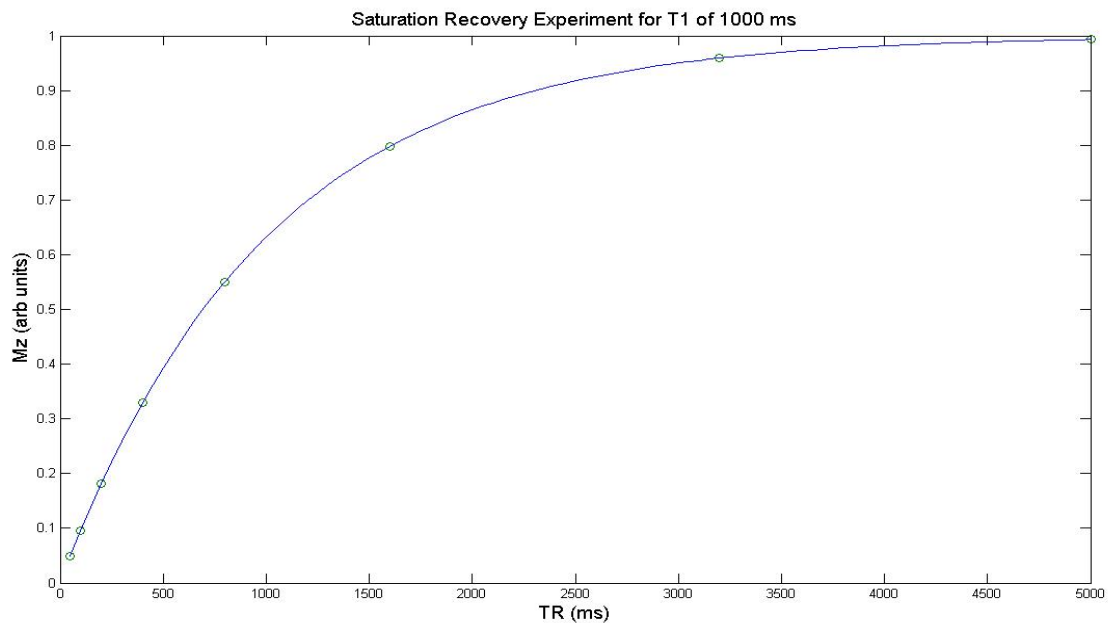


Figure 26: the above simulation illustrates the curve produced from a saturation recovery experiment with eight TR's (50, 100, 200, 400, 800, 1600, 3200 and 5000ms).

2.3.4.2 PRESS Spectroscopic Saturation Recovery Experiment 1

The figure below illustrates the saturation recovery curve obtained for a doped deionised water phantom.

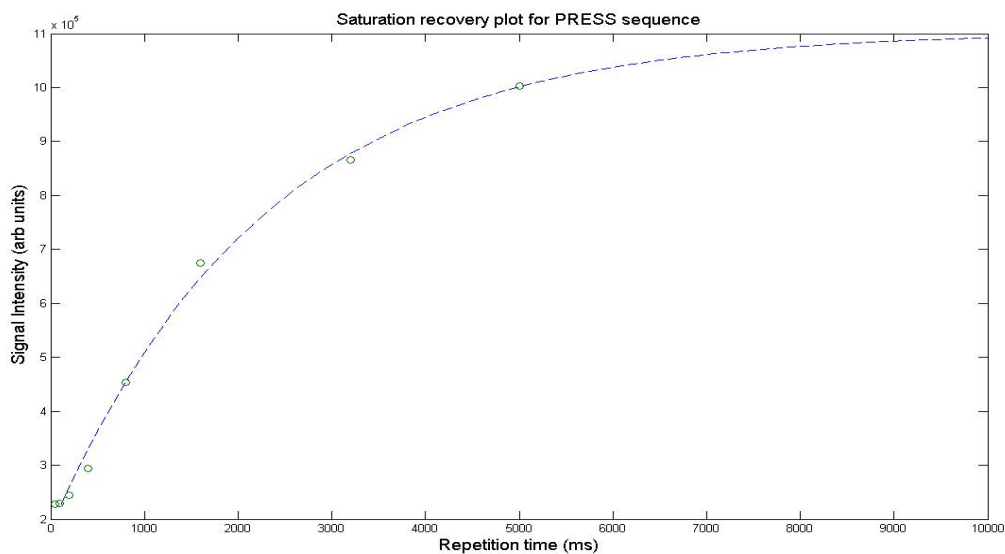


Figure 27: the saturation recovery curve obtained above is a fit from one voxel in a doped deionised water phantom. This curve produced a T_1 of 1.14 sec.

The table presented below exhibits the R_1 determined for the different scans and the R_1 which should be obtained from the amount of gadopentetate (Concentration) which was added to the solution (R_1 from mM added).

Concentration (mM)	R_1 (sec ⁻¹) at P1	R_1 (sec ⁻¹) at P2	R_1 from mM added
0	0.31	0.36	0.36(±0.12)
0.33(±0.025)	2.41	2.51	2.00(±0.12)
0.18(±0.025)	1.50	1.37	1.25(±0.12)
0.0756(±0.025)	1.54	1.01	0.74 (±0.12)

Table 2: in the table above the different R_1 times for the doped phantoms are presented.

2.3.4.3 Bland-Altman Analysis

The figure below presents the Bland-Altman plot [91] for the spectroscopic saturation recovery R_1 values obtained at the beginning of a scanning session (P1) and those obtained at the end (P2; after two RARE-VTR sequences had been performed).

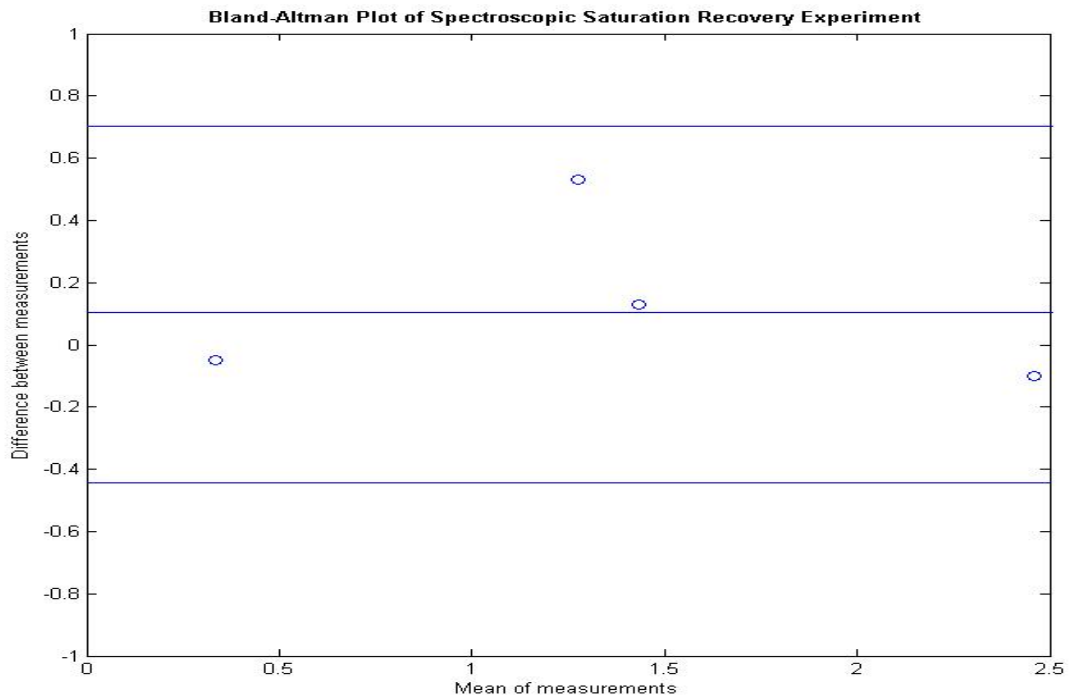


Figure 28: the figure above illustrates the agreement seen for the R_1 measurements made using the spectroscopic PRESS measurement at P1 and P2 for phantoms doped with different concentrations of gadopentetate. The black line represents the mean difference for measurements and the upper and lower blue lines are the mean difference + 2 times the standard deviation of the differences and the lower blue line the mean difference – 2 times the standard deviation.

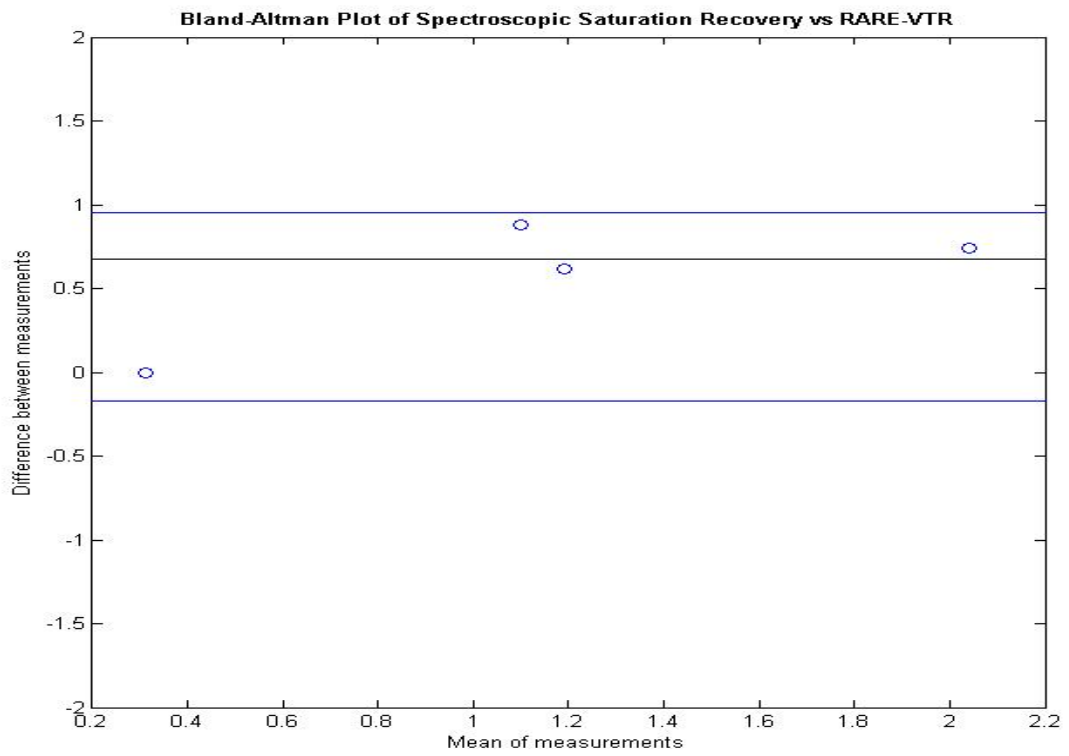


Figure 29: the figure above illustrates the Bland-Altman plot obtained for the spectroscopic saturation recovery at P2 against that obtained with the RARE-VTR sequence.

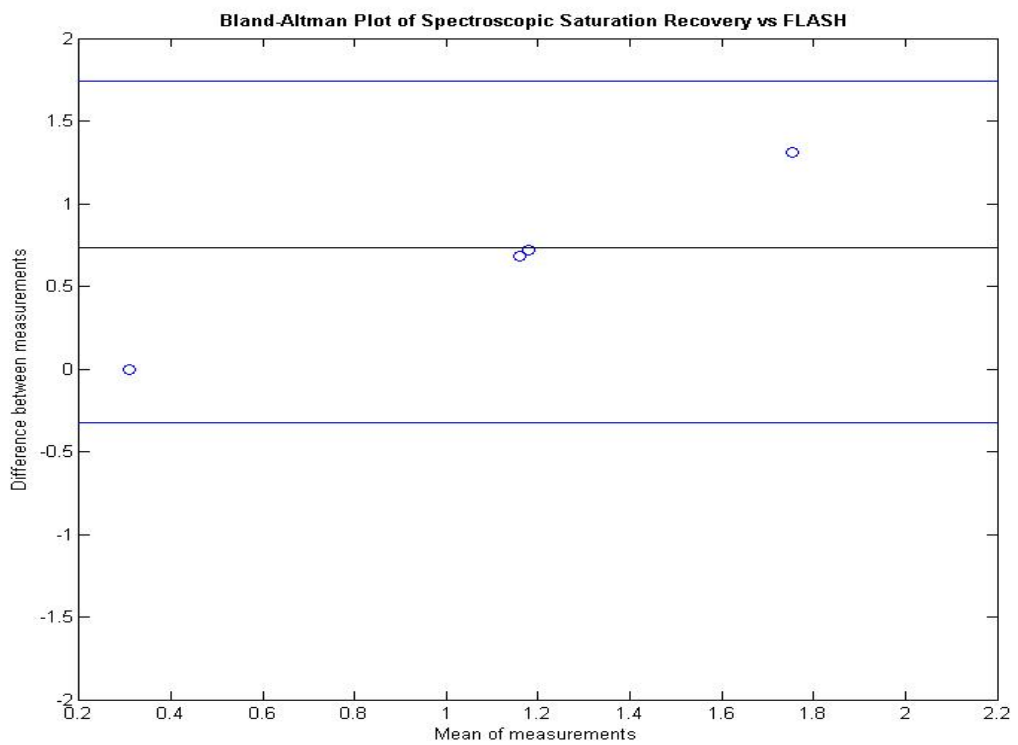


Figure 30: the figure above illustrates the Bland-Altman plot of the spectroscopic saturation recovery at P2 against the FLASH sequence with three flip angles.

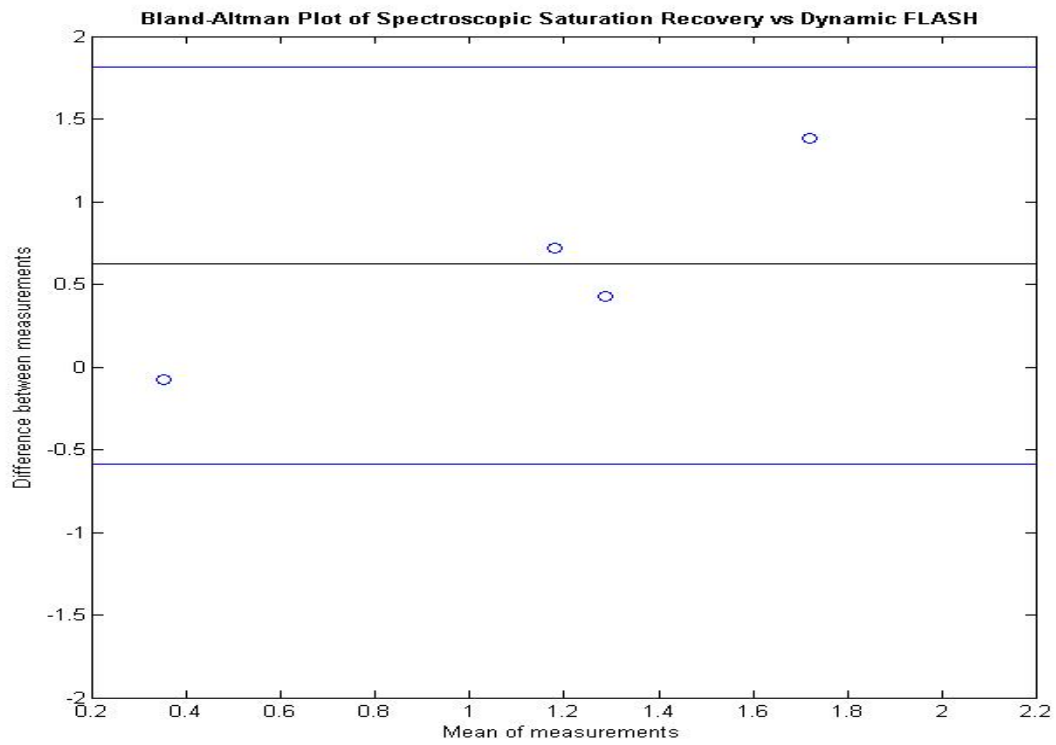


Figure 31: Bland-Altman plot of the spectroscopic saturation recovery R_1 measurements at P2 against the dynamic FLASH.

2.3.4.4 RARE-VTR Saturation Recovery Simulation

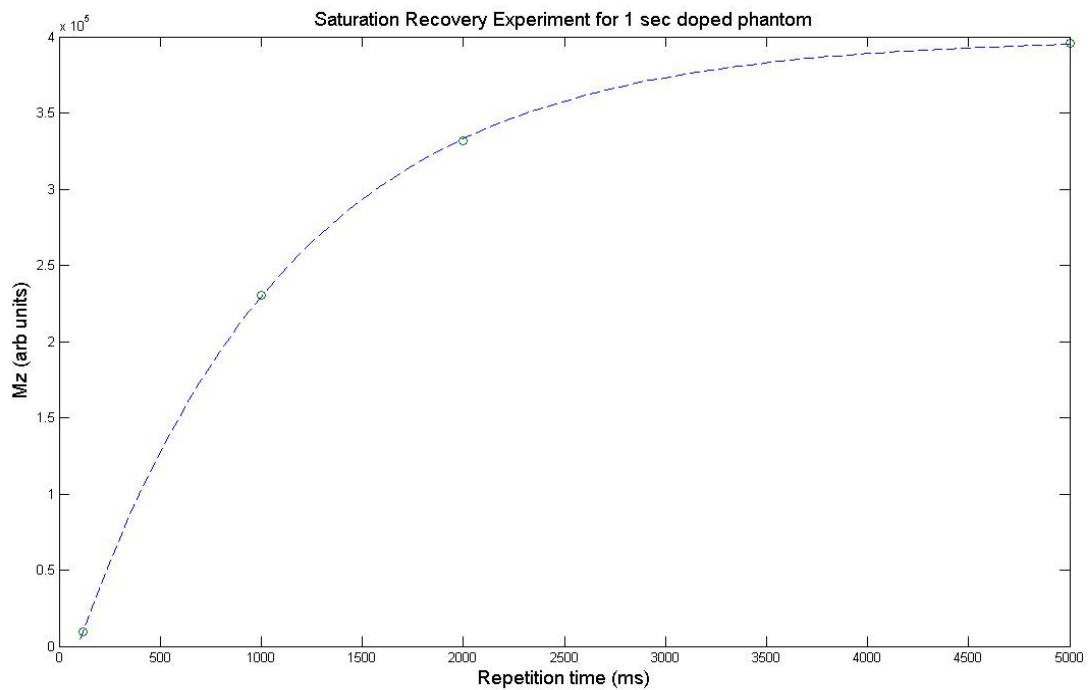


Figure 32: the simulated plot above shows a saturation recovery experiment for a T_1 of 1000 ms with four TR's of 119.349, 1000, 2000 and 5000 ms.

It can be observed that the circles on the curve representing the different TR's sample over a wide dynamic range. This enables good characterisation of the curve and thus an accurate measurement of the representative T_1 value. At the longest TR of 5000ms it would appear that the curve is approximately horizontal, indicative of complete relaxation of the longitudinal magnetisation to its equilibrium value.

2.3.4.5 RARE-VTR Saturation Recovery Experiment 1

Figure 33 below illustrates the saturation recovery curve obtained for a doped deionised water phantom.

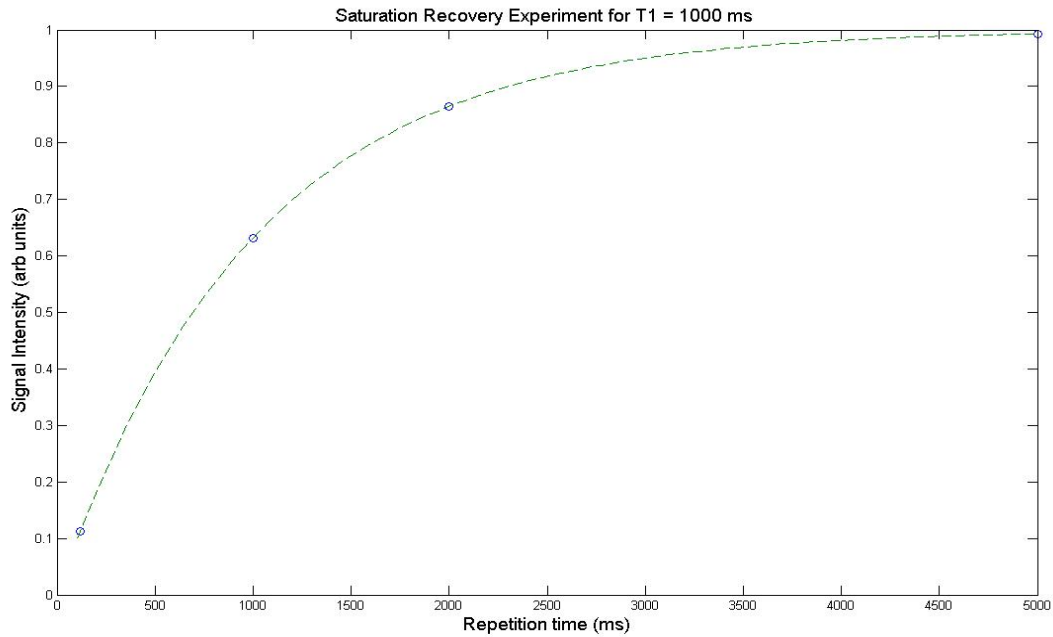


Figure 33: the above curve illustrates the recovery of the longitudinal magnetisation to equilibrium in the RARE-VTR sequence for a deionised water phantom doped with gadopentetate to a T_1 of approximately 1 sec.

The table presented below exhibits the R_1 time determined for the different scans and the R_1 which should be obtained from the amount of gadopentetic acid which was added to the solution.

Concentration (mM)	Imaging R_1 (sec ⁻¹)	Imaging R_1 (sec ⁻¹)	R_1 from mM added
0	0.31(±0.04)	0.32(±0.04)	0.36(±0.12)
0.33(±0.025)	1.67(±0.04)	1.66(±0.04)	2.00(±0.12)
0.18(±0.025)	0.88(±0.03)	0.89(±0.03)	1.25(±0.12)
0.0756(±0.025)	0.66(±0.02)	0.66(±0.02)	0.74 (±0.12)

Table 3: in the table above the different R_1 times for the doped phantoms are presented.

2.3.4.6 Bland-Altman Analysis

A Bland-Altman plot of the R_1 values obtained for the two saturation recovery experiments performed on each phantom is presented to assess the agreement between these experiments.

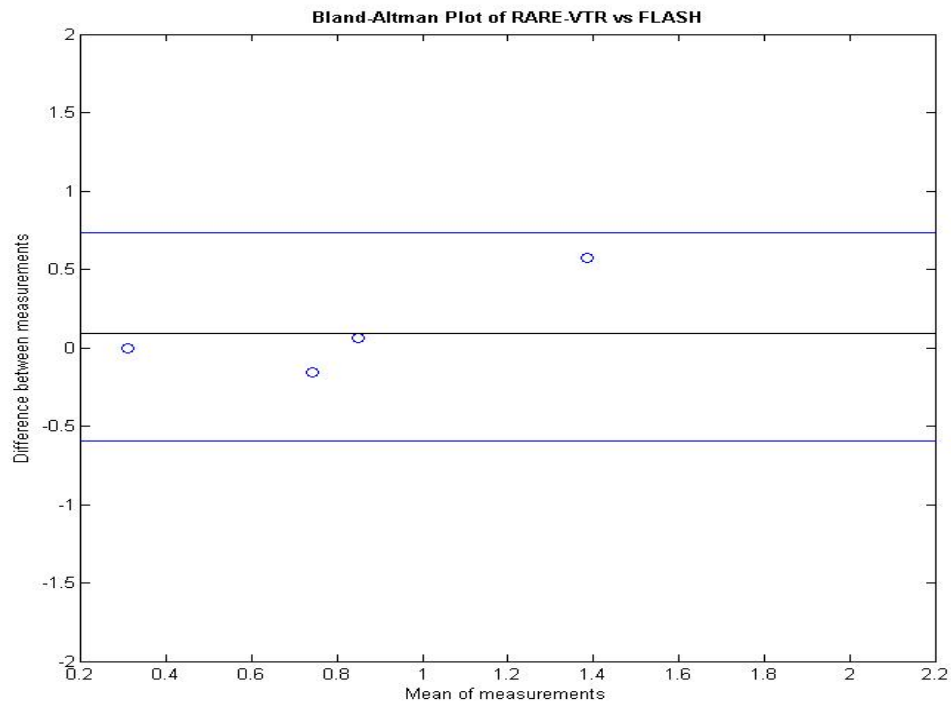


Figure 34: the figure above illustrates the agreement seen for the measurements of R_1 made using the RARE-VTR and FLASH sequences.

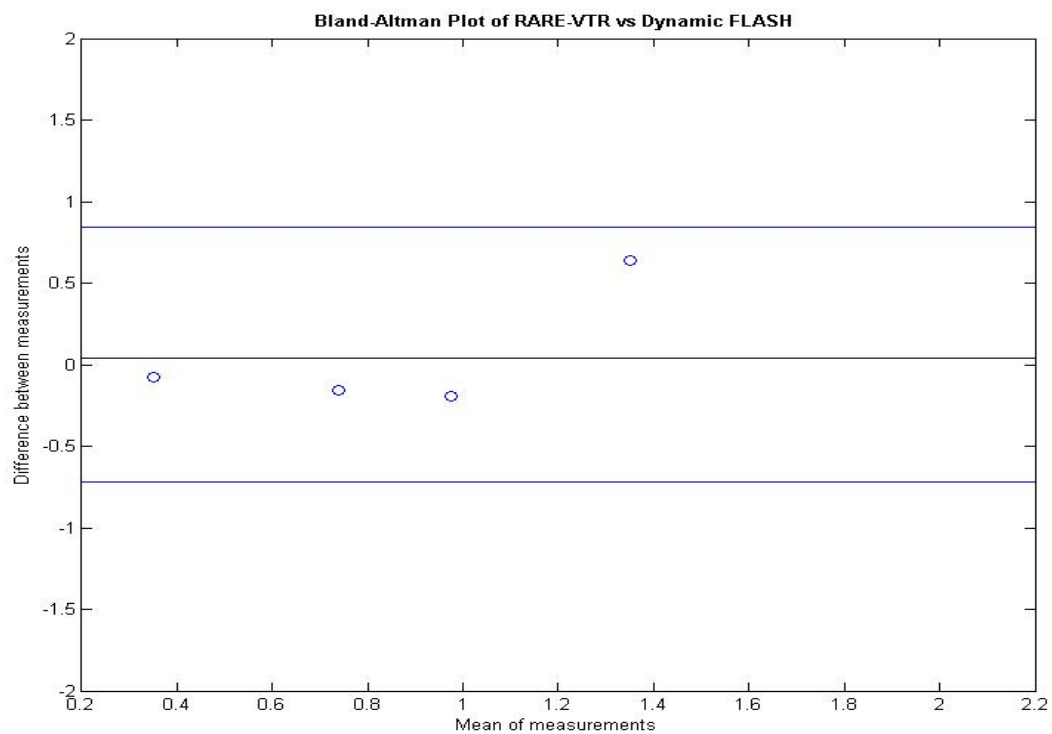


Figure 35: Bland-Altman for RARE-VTR against Dynamic FLASH is presented.

2.3.4.7 RARE-VTR Saturation Recovery Experiment 2

The figure below illustrates the R_1 values computed for each sequence that was run (x15) on a deionised water phantom doped to an R_1 of approximately 1 sec (table 3, column 4 and row 4).

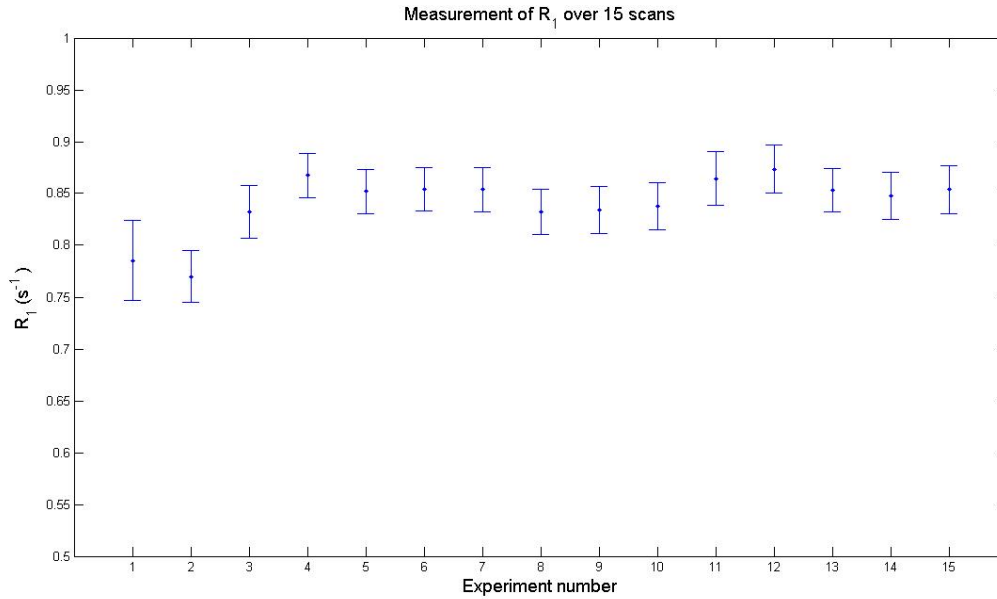


Figure 36: the above figure illustrates the consistency obtained for the R_1 measurements made as a function of time. Error bars represent the standard deviation over the entire volume for each scan.

The figure above illustrates that the R_1 measurements appear to vary little over 15 scans. It is however evident that the first two scans have R_1 values lower than the rest of the data presented. The temperature increases which occur in the bore of the magnet as a function of time can be hypothesised to cause the R_1 to increase as the scans are run. The coefficient of variation obtained over all scans is 0.034; indicating that the R_1 measured appears to be consistent.

2.3.4.8 FLASH Variable Flip Angle Experiment 1

Figure 37 below illustrates the linear curve fitting obtained for a 1sec doped deionised water phantom. Three flip angles were used to determine T_1 (2, 14 and 24°).

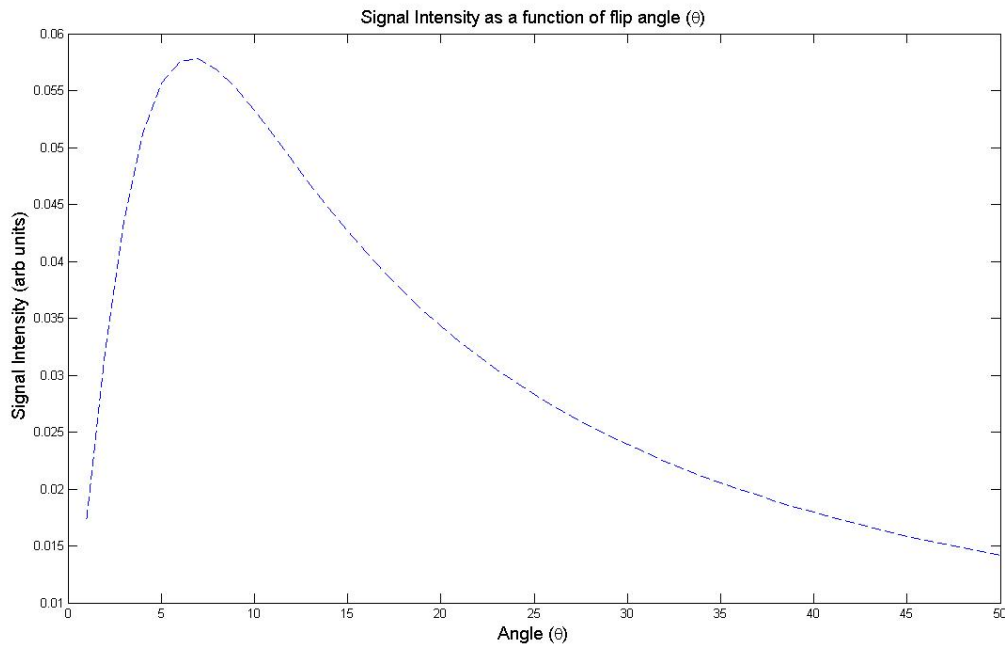


Figure 37: the above figure illustrates the linear fit for a T_1 of 1sec and a TR of 6.7ms obtained from equation 48.

2.3.4.9 FLASH Variable Flip Angle Experiment 2

The table presented below exhibits the R_1 time determined for the different scans and the R_1 which should be obtained from the amount of gadopentetate which was added to the solution.

Concentration (mM)	Imaging R_1 (sec^{-1})	R_1 from mM added (sec^{-1})
0	0.31(± 0.05)	0.36(± 0.12)
0.33(± 0.025)	1.1(± 0.11)	2.00(± 0.12)
0.18(± 0.025)	0.82(± 0.12)	1.25(± 0.12)
0.0756(± 0.025)	0.82(± 0.1)	0.74 (± 0.12)

Table 4: in the table above the different R_1 times for the doped phantoms are presented.

2.3.4.10 Bland-Altman Analysis

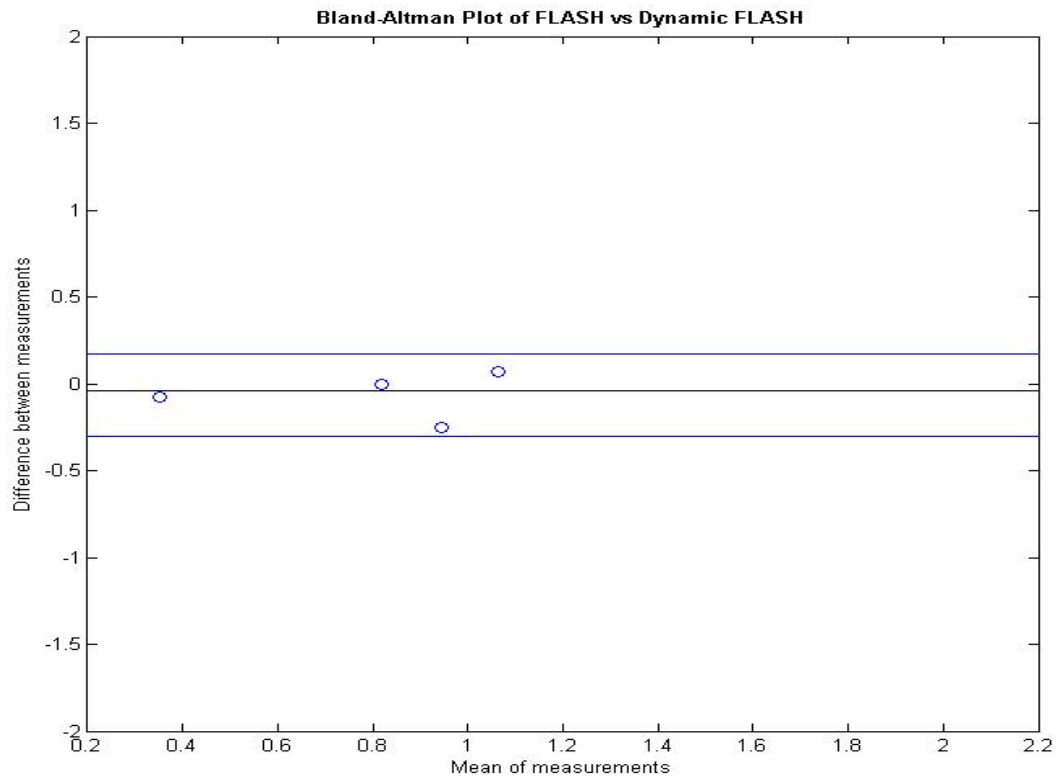


Figure 38: the figure above illustrates the agreement seen for the measurements of R_1 made using the FLASH and dynamic FLASH sequences.

2.3.4.11 Validation of Imaging Sequence Table

The table below presents the R_1 values obtained for each imaging sequence (“Imaging R_1 measured by”). The concentration of gadopentetate added to each phantom is defined as “Magnevist Concentration/mM”, the R_1 value such a concentration should produce is represented by “ R_1 measured from know relaxivity of Magnevist/s⁻¹”. The PRESS sequence is taken as the “gold standard” R_1 measurement from which the error in the R_1 for the RARE-VTR and FLASH sequences is determined (percentage difference in R_1 values). This is represented by “Error in concentration measured by”. The concentration of gadopentetate required to produce the observed R_1 values produced for each phantom is also presented as “Magnevist concentration/mM measured by”. The coefficient of variation is computed over 15 repetitions of the Dynamic FLASH sequence for each phantom and is represented by “CoV % Magnevist Concentration measured by dynamic FLASH”. The table illustrates the dissimilar values for R_1 produced by each sequence for the different phantoms.

2.3.4.11 Validation of Imaging Sequences Table

Magnevist concentration / mM \pm probable error (from propagation of errors)	R_1 estimated from known relaxivity of Magnevist /sec ⁻¹ \pm probable error (from propagation of errors)	“Gold standard” R_1 measured by PRESS /sec ⁻¹	Imaging R_1 measured by SR /sec ⁻¹ \pm SD	Imaging R_1 measured by PN /sec ⁻¹ \pm SD	Imaging R_1 as measured by PN with variability exhibited by dynamic FLASH /sec ⁻¹ \pm SD	Magnevist conc/mM measured by PRESS	Magnevist conc/mM measured by SR \pm SD	Magnevist conc/mM measured by PN \pm SD	Magnevist conc/mM measured by PN with variability exhibited by dynamic FLASH /sec ⁻¹ \pm SD	Error in conc measured by SR %	Error in concentration measured by PN %	CoV % in Magnevist concentration measured by dynamic FLASH
0.18 \pm 0.025	1.25 \pm 0.12	1.37	0.89 \pm 0.03	0.82 \pm 0.12	1.0708 \pm 0.13	0.20	0.11 \pm 0.07	0.093 \pm 0.05	0.14 \pm 0.05	39%	48%	0.002
0.0756 \pm 0.025	0.74 \pm 0.12	1.01	0.66 \pm 0.02	0.82 \pm 0.1	0.82 \pm 0.1	0.13	0.06 \pm 0.07	0.06 \pm 0.05	0.09 \pm 0.05	21%	21%	0.003
0.33 \pm 0.025	2.00 \pm 0.12	2.50	1.66 \pm 0.04	1.1 \pm 0.11	1.03 \pm 0.11	0.43	0.26 \pm 0.06	0.15 \pm 0.05	0.14 \pm 0.05	21%	55%	0.001
0	0.36 \pm 0.12	0.36	0.32 \pm 0.04	0.31 \pm 0.05	0.39 \pm 0.06	NA	NA	NA	NA	NA	NA	NA

Table 5: the above table illustrates the R_1 values measured by the different sequences. SD represents the standard deviation and NA not applicable. SR represents saturation recovery, PN pulsed nutation (FLASH), and PN with variability exhibited by dynamic FLASH, the FLASH sequence performed with one flip angle. “Conc” is a truncation of concentration.

2.3.4.12 Validation of Imaging Sequences Graphs

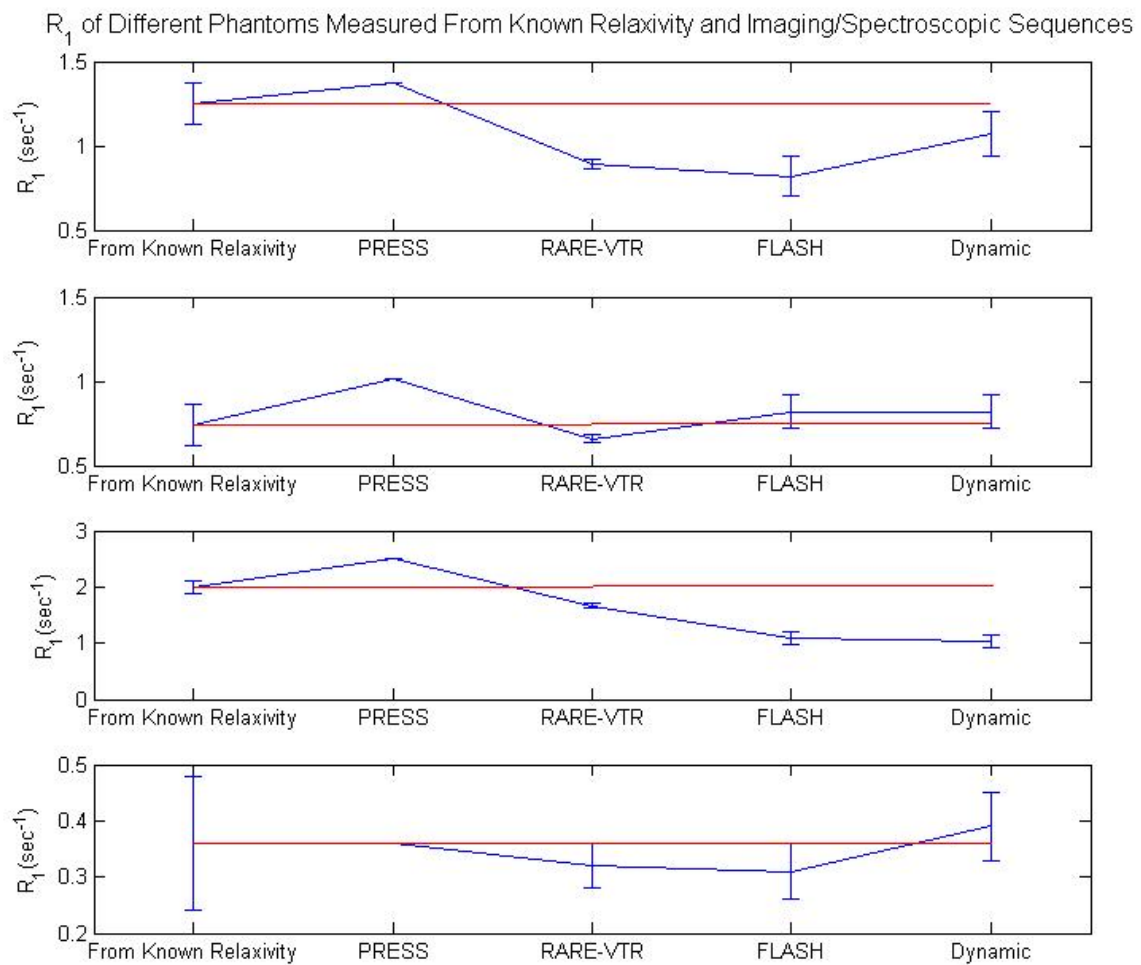


Figure 39: the figure above plots the R_1 measured for each sequence and that from the known relaxivity of gadopentetate. The red line corresponds to the R_1 from the known relaxivity plotted longitudinally against those obtained from imaging. Error bars represent standard deviations.

2.3.5 Discussion

Validation of the imaging sequences to be used in a study is of fundamental importance if the values are to be interpreted with confidence. The Bland-Altman plot enables the agreement between the different measurement techniques to be assessed [73]. The results above indicate discrepancies between the different methods used to measure T_1 . The experimental method undertaken may explain the disagreement observed. As discussed previously, gradient induced temperature changes are a negligible effect. The increase in R_1 after two RARE-VTR experiments in evidence from tables 2,3 and 4 may be a result of the phantom equilibrating inside the bore of the magnet. The literature indicates that an increase in temperature results in an increase in T_1 and hence an decrease in R_1 [92], this is opposite to that observed in the experiments above. One possible means of mitigating the effect of temperature upon the measured R_1 values is to use an ice water phantom as used for the validation of ADC measurements. An ice water phantom would enable a range of R_1 's to be measured at approximately 0°C, thus negating the effect of temperature upon the measured R_1 values.

The disagreement in evidence across the spectrum of sequences indicates that further methods development should be undertaken to investigate the source of this bias. The development of a B_1 mapping sequence is discussed in the future work section of this document (6.2). The use of the above sequences in an in vivo study is unacceptable due to this difference in sensitivity to R_1 which would limit the interpretation of contrast agent concentration calculations, fundamental for the DCE-MRI post processing procedure. Pharmacokinetic modelling requires a measurement of the baseline R_1 and subsequent R_1 values, which enable the concentration of contrast agent to be calculated for the duration of the experiment. If the sequence measures an inaccurate baseline R_1 , yet the change in R_1 due to the contrast agent is a linear function of contrast agent concentration on a voxelwise basis, the concentrations deduced from the change in R_1 could be input into the subsequent pharmacokinetic analysis. The results presented above in figure 39 and in tables 2-5, indicate that different concentrations of contrast agent do not result in a linear change in R_1 , across all sequences. This precludes the use of the above sequences in a DCE-MRI study.

2.4 Inductively Coupled Plasma Mass Spectrometry

2.4.1 Introduction

The ability to determine the quantity of a particular atomic isotope is of importance in a wide variety of scientific disciplines. The ICP-MS system offers advantages due to its high sensitivity to low atomic mass isotopes, in addition to its high specificity [93]. Gadolinium has an atomic mass of 157, well within the detection capability of the ICP-MS system. Determining the concentration of gadolinium in a tumour sample enables comparisons to be made with the concentrations as deduced from imaging experiments.

2.4.2 Materials and Methods

2.4.2.1 Experimental Protocol

Calibration

The machine is calibrated using serial dilutions from a certified concentration standard. A different standard is then run as an unknown to verify the calibration. ICP-MS has a detection sensitivity of 0.5ppb. The results of the analysis will yield the quantity of Gadolinium in parts per million or mg/l.

Pilot Study

A pilot study was performed to determine the sensitivity of the ICP-MS system to Gd. As such 2ml (± 0.1 ml) or alternatively 1 mmol (± 0.05 mmol) of gadopentetate was diluted in 10ml of deionised water ($64\text{mg/L} \pm 3.2\text{mg/L}$ or $100\text{mM} \pm 5\text{mM}$). This sample was transferred immediately to the ICP-MS laboratory for analysis.

2.4.2.2 Calculation of Gadolinium in Whole Tumour Volume

The method presented is as follows: To determine the amount of gadolinium that is present within a whole tumour the Gd concentration in mg/ml is converted into the quantity of Gd in units of mmol. As there is 0.32mg Gd in 1ml of gadopentetate, knowledge of the amount of Gd in mg can yield the volume of gadopentetate in ml. This can then be converted into the amount of gadopentetate in mmol as it is a 0.5mmol/ml solution. The tumour is weighed and then placed in concentrated acid. There will be an increase in volume ΔV before and after digestion. The concentration of Gd in the tumour can be determined as shown below:

$$[59] \quad Q_{Gd} = V_s \times C_s$$

Where V_s is the volume of the sample submitted for analysis (ml), C_s the concentration of the sample returned from ICP-MS (mg/ml) and Q_{Gd} the quantity in mg. Thus for 0.32mg Gd per ml of gadopentetate:

$$[60] \quad V_{Magnevist} = \left(\frac{Q_{Gd}}{0.32} \right)$$

As there is 0.5 mmol per ml gadopentetate:

$$[61] \quad Q_{mmol} = (0.5 \times V_{Magnevist})$$

The Gd concentration in a tumour can be determined from:

$$[62] \quad C_{Gd} = \left(\frac{Q_{mmol}}{(\Delta V)} \right)$$

Worked example:

ICP-MS returns 0.002mg/ml from a 10ml sample. The volume change ΔV was 1ml (9ml pre and 10ml post digestion). This corresponds to 0.02mg of gadolinium in the sample volume.

$$[63] \quad Q_{Gd} = 0.02$$

$$[64] \quad V_{Magnevist} = \left(\frac{0.02}{0.32} \right) = 0.0625$$

$$[65] \quad Q_{mmol} = (0.0625 \times 0.5) = 0.031$$

$$[66] \quad C_{Gd} = \frac{Q_{mmol}}{(\Delta V)} = 0.031$$

Thus the concentration can be compared to that derived from DCE-MRI.

2.4.3 Results

The ICP-MS returned a concentration of 64.3mg/L for the sample submitted for analysis. This shows good agreement with the value measured from the syringe. The error on the volume measurement made is ± 0.1 ml, corresponding to a concentration of 3.2mg/L. This indicates that the value obtained by the ICP-MS is well within the error on the experimental measurements.

2.4.4 Discussion

The experiment showed agreement between the two methodologies. The concentration submitted for analysis was however large compared to that which one would anticipate to observe in vivo. The maximum dose that gadopentetate is administered at is 0.6ml/kg or . Assuming the average weight of a mouse to be approximately 20g would indicate that 0.012ml would be the maximum volume administered to a mouse. This differs considerably from the volume used in the presented experiment. As this was the first known measurement of gadolinium on the ICP-MS system a high volume was required to confirm sensitivity to the isotope. A more accurate validation method would have entailed investigating doses representative of that received by a mouse in a preclinical experiment. Measuring the sample volume change due to tumour digestion suffers from the confound that both intracellular and extracellular materials contribute. Weighing the sample does not appear to obviate this problem, as neither dry nor wet weight will allow the actual water content of the extracellular compartment to be uniquely determined [94]. This is an important consideration in the preparation and analysis of ICP-MS data from tumour samples.

3. The Effect of Radiotherapy Upon the Apparent Diffusion Coefficient in a Preclinical Cancer Model

3.1 Introduction

The use of radiotherapy in the treatment of solid tumours is a common therapeutic intervention given to approximately 50% of all cancer patients [95]. There are a significant number of preclinical studies looking at the effect of chemotherapy upon cell death and the corresponding change in ADC values [96], [97]. However, there are fewer papers concerning radiotherapy as a therapeutic intervention [98]. Clinical studies have looked at the effect of radiotherapy on ADC values in tumours; many clinical studies are concerned with chemoradiation as this is the most common treatment given to cancer patients [99–101]. As cell death is hypothesised to increase the non-viable cell fraction the diffusion of water molecules should become less restricted due to a decrease in the number of cell membrane boundaries encountered by the water proton spin. Cross correlating the ADC changes with histology would enable one to determine the pathophysiologic basis of ADC change. The change in tumour volume was also measured to enable a comparison between this conventional technique used to assess response to therapy and ADC.

The LoVo cell line is a human colon adenocarcinoma cell line with morphological and physiological characteristics which are in agreement with a type 1 classification of colorectal carcinoma lines [102–104]. Although in vitro results have shown a positive response to radiotherapy, in vivo studies have failed to show a similar positive outcome. In particular radiation therapy of the colon has been associated with a poor response to therapy [105]. To improve the effectiveness of radiation therapy a number of studies have incorporated the use of radiosensitising drugs [102], [106]. Previous in vitro work with the LoVo cell line has studied radiosensitivity and shown a degree of radioresistance amongst the cells which increases with fractionation of the dose. As many cancers exhibit a degree of radioresistance there is significant scientific value in determining the efficacy of a single dose of radiotherapy as a therapeutic intervention.

3.1.1 Experimental Hypothesis

The experimental hypothesis was that the net ADC value computed over a tumour volume would increase after treatment with 10Gy of radiotherapy.

3.2 Materials and Methods

3.2.1 Study Design

Animal studies were performed in compliance with the NCRI Guidelines for the welfare and use of animals in cancer research and UK Animals (Scientific Procedures) Act after local Ethical Committee review [107]. Tumour xenografts were initiated from LoVo colorectal tumour cells (5×10^6 per mouse) and implanted in female nu/nu CBA mice aged 10 weeks old. Tumours were grown orthotopically on the lower back of the mice to reduce respiratory motion artefacts. When tumours reached 300-400 mm³ in size, mice were randomised to a control group (sham; n=9) or to tumour localised radiotherapy (10Gy; n=10) administered under ambient conditions to restrained non-anaesthetised mice. Imaging was performed at 1 hour post and 72 hours post radiotherapy along with measurement of the tumour volume using callipers. To ensure consistency in calliper measurements the same individual performed the measurements throughout the experiment. Following the second MRI scan mice received the perfusion marker Hoechst 33342 (0.1ml of a 6mg/ml solution). Tumours were excised 1 minute later and rapidly snap frozen for histology.

3.2.2 Image Acquisition and Analysis

Imaging was performed on a 7T Bruker preclinical scanner with a volume transceiver coil. A T₂ weighted sequence was provided anatomical localisation of the tumour for the diffusion scan with the following parameters: - TR/TE 2410.1/50 ms, matrix size 256 x 256, FOV = 2.56cm x 2.56 cm, slice thickness = 6mm, interslice distance = 6mm, number of slices = 15, averages = 2. After this scan a diffusion weighted spin echo sequence was then run with the following parameters: - TR/TE =2250/20 ms; b values of 150,500 and 1000 s/mm² (Δ = 9ms and δ = 4.5ms); 15 contiguous slices of 6mm thickness; matrix 128 x 128 and FOV 2.56cm x 2.56cm. The b values were chosen in accordance with recent guidelines set out for the use of diffusion imaging in cancer [108]. Voxelwise values of ADC were calculated in *Matlab* (Mathworks) within a region of interest of the tumour using a least squares fitting algorithm and assuming Rician noise. The number of slices, slice thickness and field of view enabled complete coverage of the tumour volume (experiment run by J. O'Connor).

3.2.3 Animal Monitoring and Setup

Animals were kept at a constant temperature throughout the imaging session through the use of a heated water bed. The respiration rate was monitored through use of an electronic respiratory monitor.

3.2.4 Histological Analysis

Histological analysis was performed on all animals. The extent of necrosis was evaluated by Haematoxylin and Eosin staining of the sections. These were subsequently imaged using an *Axiovision* snapshot wide field microscope (Axis Observer A1). The percentage of tumour apoptosis was determined by using a fluorometric terminal transferase dUTP nick end labelling (TUNEL) assay that detects DNA degradation in apoptotic cells (DeadEnd™, Promega) in conjunction with a DAPI (4',6-diamidino-2-phenylindole) counterstain to determine the total cell density. An *Olympus* snapshot wide field fluorescent microscope (Olympus BX51) was used to image the TUNEL/DAPI stained sections. The percentage apoptosis was calculated from a minimum of twenty (x20 magnification) images per section for each animal. The number of TUNEL positive cells in each field was counted as was the total number of cells in the same field ("DAPI"). The percentage of apoptosis was thus determined on a per tumour basis from:

$$[67] \quad \%Apop = \frac{1}{S} \sum_{j=1}^S \left(\frac{1}{N} \sum_{i=1}^N \left(\frac{A_i}{T_i} \right) \right)$$

For percentage apoptosis "A_i" represents the total number of TUNEL positive stained cells and T_i the total number of cells in the field of view (i.e. apoptotic and non-apoptotic) over "N" fields of view in "S" sections. The percentage necrosis was determined by segmentation of the imaged sections and quantified by the ratio of non-viable to viable tissue:

$$[68] \quad \%Nec = \left(\frac{1}{N} \sum_{i=1}^N \left(\frac{A_i}{T_i} \right) \right)$$

The total area of necrosis is represented by "A_i" and the total tissue area by "T_i". The percentage necrosis is thus calculated for "N" sections on a per tumour basis.

Mice received the perfusion marker Hoechst 33342 (0.1ml of a 6mg/ml solution in PBS) via the tail vein after the second MRI scan. Mice were killed 2 minutes later and tumours excised. Sections were cut at 5µm thickness using a cryostat and stored at -80°C prior to histological staining. The perfused vessel density was determined by using an Olympus snapshot wide field fluorescent microscope (Olympus BX51) to detect the number of Hoechst 33342 stained vessels in a 5 µm cryostat section ("Hoechst"). Total vessel density was obtained by then fixing the sections in acetone and staining the tumour endothelial cells using rat anti-CD31 and relevant secondary antibodies ("CD31"). The

perfused and total vessel densities were determined by counting the number of vessels per viable tissue area on a per section basis;

$$[69] \quad \%Perfused / Total = \left(\frac{1}{N} \sum_{i=1}^N \left(\frac{A_i}{T_i} \right) \right)$$

The number of vessels is represented by “ A_i ” and the total viable tissue area “ T_i ”. “ N ” represents the number of sections per tumour which were analysed. All images were processed offline using *ImageJ*.

3.2.5 Statistical Analysis

Change in tumour size (from calliper measurement), ADC (mean value at 1 hour post and 72 hours post and interquartile range) and histological parameters between 1 hour and 72 hours post radiotherapy were compared with the control group using a Student’s t test, performed in *SPSS 16.0*. All tests were unpaired and one sided except for tumour volume at 1 hour post and 72 hours post treatment and the change in tumour volume between the groups, which employed a paired two tailed Student’s t test. The CD31 and Hoechst 33342 percentages perfused and total vessel densities at 72 hours were compared using an unpaired two tailed Student’s t test. A threshold of $p < 0.05$ was considered to indicate statistical significance. While numerous previous studies suggest that ADC increases as viable cell fraction decreases, we are unaware of any algorithm to transform a specific ADC value into a viable cell fraction. However, we reasoned that if ADC is a proxy for necrosis, then those tumours with a high percentage of necrosis (measured by histology) should also have a similarly high percentage of voxels with elevated ADC.

Specifically, if the i^{th} tumour has pathological percentage necrosis $(\%H\&E)_i$ and N_i voxels, giving a weighted mean percentage necrosis T , we can create a “fictitious threshold”, the T^{th} percentile of ADC across all voxels in all tumours at 72 hours, where

$$[70] \quad T = \frac{\left(\sum_{i=1}^N (\%H \wedge E)_i N_i \right)}{\sum_{i=1}^N N_i}$$

Once the threshold value T is produced from the calculation above, the ADC values from the treated group are used to generate a histogram with a bin width of $0.001 \text{ mm}^2/\text{s}$. The ADC value corresponding to the T^{th} percentile was then used to define a threshold. The number of voxels with ADC values exceeding this threshold at 1 and 72 hours post treatment

was used to generate a percentage change in ADC, corresponding to the increase in the number of voxels above the fictitious threshold at 72 hours post treatment. If ADC is a proxy for necrosis, the proportion of voxels in each tumour with ADC exceeding T should correlate with the percentage necrosis (H&E%n) measured on pathological sections on a per tumour basis. This analysis approach has the advantage of expressing both the MRI and histology biomarkers as percentages, enabling direct and meaningful correlation (suggested by J. Waterton). Regression analysis was performed (*Matlab*) with H&E, TUNEL, Hoechst 33342, and CD31 as explanatory variables with their respective coefficients (

$\hat{\beta}_1, \hat{\beta}_2, \hat{\beta}_3, \hat{\beta}_4$) and the percentage of voxels above the fictitious threshold (T) as the predicted response. Four different

models were implemented. Interaction terms were included in models three and four to account for any possible relationship between the predictor variables (interaction predictor variables represented by x_5, x_6, x_7, x_8, x_9 and x_{10} with

coefficients $\hat{\beta}_5$ to $\hat{\beta}_{10}$). The regression model can be represented as:

$$[72] \quad \hat{y} = const + \hat{\beta}_1 x_1 + \hat{\beta}_2 x_2 + \hat{\beta}_3 x_3 + \hat{\beta}_4 x_4 + \hat{\beta}_5 x_1 x_2 + \hat{\beta}_6 x_1 x_3 + \hat{\beta}_7 x_1 x_4 + \hat{\beta}_8 x_2 x_3 + \hat{\beta}_9 x_2 x_4 + \hat{\beta}_{10} x_3 x_4$$

Models one and two contained one predictor variable (H&E staining and TUNEL respectively; with either $\hat{\beta}_1$ or

$\hat{\beta}_2$ set to zero and then $\hat{\beta}_3$ to $\hat{\beta}_{10}$ all set to zero) while model three contained two predictor variables (H&E

and TUNEL; $\hat{\beta}_3$, $\hat{\beta}_4$, $\hat{\beta}_6$, $\hat{\beta}_7$, $\hat{\beta}_8$, $\hat{\beta}_9$ and $\hat{\beta}_{10}$ set to zero) and model four contained four

predictor variables (H&E, TUNEL, CD31 and Hoechst 33342) along with their respective interaction terms. The reproducibility of the histopathological measurements was determined by calculating the coefficient of variation for the four histopathological techniques used where the coefficient of variation is defined as

$$[73] \quad COV = \frac{\sigma}{\mu}$$

Where μ represents the mean and σ the standard deviation over the different sections of a per tumour basis.

3.3 Results

3.3.1 Fictitious Threshold

This method produced a fictitious threshold, T of 0.902 mm²/s.

3.3.2 Summary Table

The table below summarises the results obtained from all animals. The 38 tumour datasets yielded 310,269 voxels from 397 slices. Of these, 253 voxels were set to 0 as they failed to satisfy the R^2 or signal to noise threshold.

Parameter		Sham (n=9)	Treated (n=10)	<i>p</i> value
Volume (mm ³)	1 hr post	365 ± 73	398 ± 66	0.53
	72 hr post	501 ± 108	455 ± 101	0.34
	Change 1-72 hr	136 ± 40	57 ± 56	0.005
Mean ADC ± SD (mm ² s ⁻¹)	1 hr post	0.745 ± 0.125	0.743 ± 0.079	0.483
	72 hr post	0.747 ± 0.139	0.856 ± 0.105	0.003
	Change 1-72 hr	0.002 ± 0.083	0.109 ± 0.067	<0.001
ADC IQR (mm ² s ⁻¹)	1 hr post	0.286 ± 0.073	0.283 ± 0.058	0.498
	72 hr post	0.309 ± 0.139	0.359 ± 0.076	0.013
	Change 1-72 hr	0.024 ± 0.099	0.076 ± 0.078	0.221
Haematoxylin and Eosin (% necrosis)		22 ± 4	30.6 ± 6	0.001
TUNEL (% apoptosis)		22.8 ± 5	28.2 ± 10	0.09
Hoechst (perfused vessel density)		62 ± 55	57 ± 57	0.56
CD31 (total vessel density)		56 ± 21	50 ± 25	0.59

Table 6: Summary of parameter values for sham and treated groups of animals. Statistically significant ($p < 0.05$) p values are highlighted in bold (\pm represents the standard deviation).

3.3.2.1 Diffusion weighted, ADC and R^2 Maps

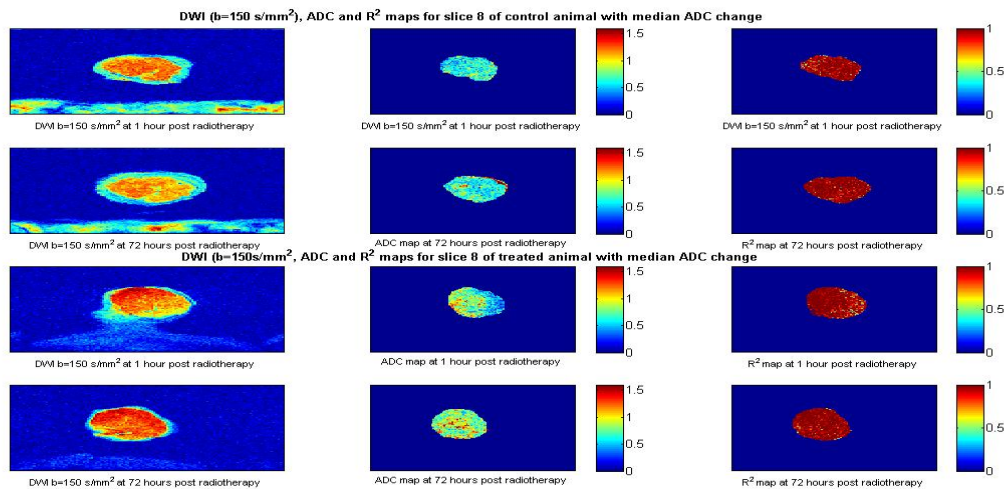


Figure 40: the above panels illustrate the diffusion weighted image, ADC map and R^2 fits obtained for representative animals.

3.3.2.2 Fictitious Threshold Analysis

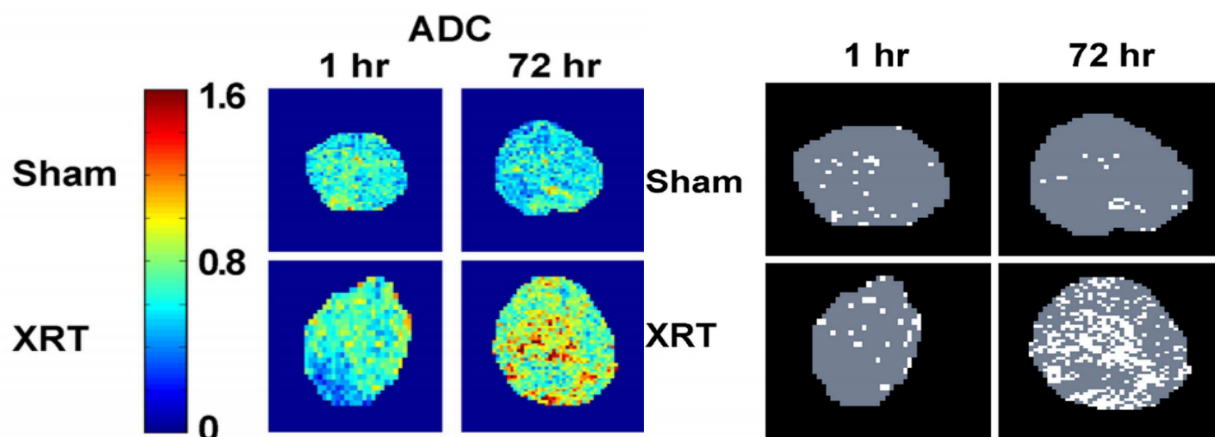


Figure 41: the fictitious threshold applied to the ADC maps on the left of the figure is shown in the right hand panels.

3.3.3 Regression Analysis

The table below summarises the results of the linear regression analysis.

Model	$\hat{\beta}_1$	$\hat{\beta}_2$	$\hat{\beta}_3$	$\hat{\beta}_4$	$\hat{\beta}_5$	$\hat{\beta}_6$	$\hat{\beta}_7$	$\hat{\beta}_8$	$\hat{\beta}_9$	$\hat{\beta}_{10}$	P value	R ²	adjR ²
1	1.1	NA	NA	NA	NA	NA	NA	NA	NA	NA	0.0059	0.37	NA
2	0.21	NA	NA	NA	NA	NA	NA	NA	NA	NA	0.56	0.02	NA
3	2.2	-0.031	NA	NA	-0.02	NA	NA	NA	NA	NA	0.07,0.98,0.62	0.49	0.39
4	0.74	0.41	0.35	0.60	0.72	0.82	0.22	0.85	0.42	0.36	All p>0.20	0.70	0.34

Table 7: Summary of multivariate regression analysis performed where the coefficients $\hat{\beta}_1$ to $\hat{\beta}_{10}$ correspond to the coefficients for necrosis, apoptosis, CD31, Hoechst 33342 and the interaction terms between each respective predictor variable. Significant p values are highlighted in bold. NA = not applicable.

3.3.4 Histological Analysis

3.3.4.1 Quantification of the Percentage Necrosis

As detailed previously the percentage necrosis was computed from equation 68. Figure 42 below illustrates a tissue section cut to $5\ \mu m$ thickness and stained with H&E. The regions of necrosis are indicated by the positive stained of Eosin (NV) and that of viable cells (V) by the purple staining of Haematoxylin. In addition areas of the tissue section which have been damaged in the preparation process are indicated. Such areas were excluded from the subsequent analysis as they cannot be distinctly classified as viable or non-viable tissue (X).

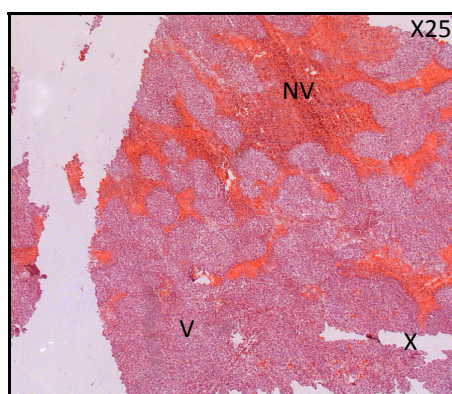
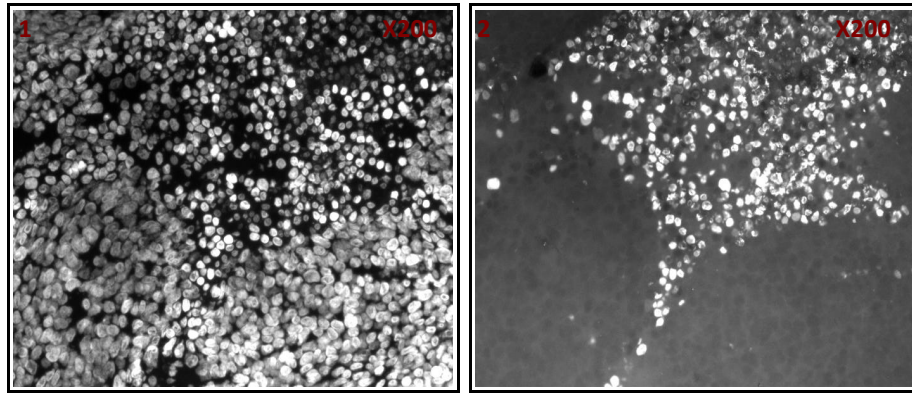


Figure 42: the image above is that of a H&E stained section.

Regions of interest were drawn around the areas representing necrosis and the total tissue section area (excluding areas marked as X). From this the % Necrosis could be determined on a per section basis. The mean value over 4 sections was used to calculate the final value.

3.3.4.2 Quantification of the Percentage Apoptosis

The TUNEL staining technique (protocol provided by *Promega Life Sciences*) requires a positive and a negative control to be developed as a means of validating the subsequently stained sections. A positive control is obtained by staining a section with DNase I which results in a significant number of double stranded breaks and as a result a strongly emitting TUNEL fluorescent signal. The negative control is created by omitting the rTdT (Terminal Deoxynucleotidyl Transferase) enzyme which is responsible for chemically bonding the fluorescein-12-dUTP (fluorescein-12-deoxyuridine triphosphate) to the 3'-hydroxyl termini of single or double stranded DNA. As such the tissue section should not produce a TUNEL signal. Figures 43 and 44 below illustrates a TUNEL stained section with the different fluorescent signals emanating from the apoptotic or non-apoptotic cells present in the section.

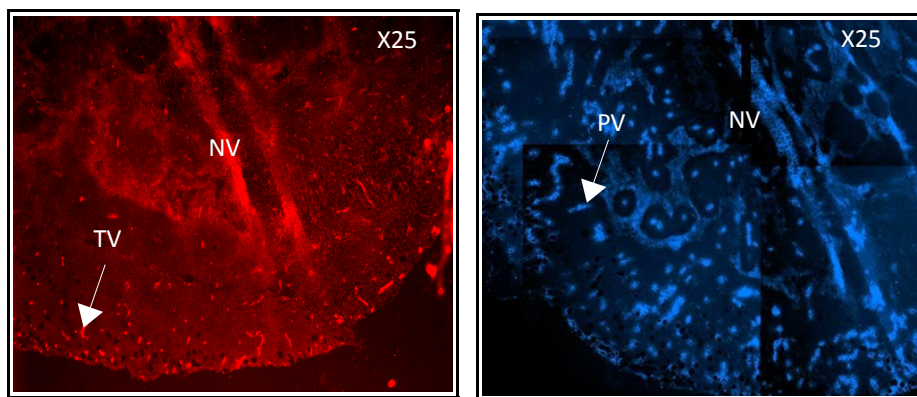


Figures 43 (left) and 44 (right): the two figures illustrate a DAPI (left) and TUNEL (right) stained section.

The two figures (43 and 44) shown above represent the DAPI counterstaining (460 nm) of the same region on the section (figure 43) and the same section for TUNEL (520nm) (figure 44). It is evident that all cell nuclei appear to stain positively for DAPI whereas only those cells with the shruken morphology characteristic of apoptotic cells stain positively for TUNEL.

3.3.4.3 Quantification of the Perfused and Total Vessel Densities

The total vessel density of a tissue section was determined by counting the number of vessels which had stained positively for CD31 on a per section basis (TV). Areas of non-viable (NV) tissue which evinced a high signal intensity were omitted from the analysis for both the perfused and total vessel density.



Figures 45 (left) and 46 (right): the figures illustrate CD31 (left) and Hoechst 3342 (right) stained sections.

The perfused vessel density was determined by identifying and counting vessels which had stained positively for Hoechst 33342 (PV) on a per section basis. The above figures illustrate the total and perfused vessel densities obtained for a region of a representative section. The actual animal from which this section was taken is not of importance as it is merely to illustrate the method for quantitation of the immunohistochemistry.

3.3.5 Results of Histopathology and Histochemical Analysis

3.3.5.1 Percentage Necrosis

The table below presents the percentage necrosis for both control and treated groups on a per animal basis.

% Necrosis	
Treated	Control
21	23
37	28
31	19
29	23
25	23
28	28
35	20
42	19
32	16
26	NA
p value = 0.001	

Table 8: the above table contains the percentage necrosis on a per animal basis.

3.3.5.1.1 Statistical Analysis for the Percentage Necrosis

A one tailed heteroskedastic t test was performed based on the premise that the % necrosis would increase after radiotherapy. This produced the p value shown in the table above.

3.3.5.2 Percentage Apoptosis

The table below presents the percentage apoptosis obtained on a per animal basis for each group of animals.

% Apoptosis	
Treated	Control
26	15
17	22
16	26
26	31
43	23
28	24
33	26
19	16
47	22
27	NA
p value = 0.09	

Table 9: the above table contains the percentage apoptosis on a per animal basis.

3.3.5.2.1 Statistical Analysis for the Percentage Apoptosis

A one tailed heteroskedastic t test was performed based on the premise that the % necrosis would increase after radiotherapy. This produced the p value shown in the table above.

3.3.5.3 Total Vessel Density

The table below presents the Total Vessel Density obtained on a per animal basis for each group of animals.

Total Vessel Density	
Treated	Control
49	79
32	32
92	77
86	35
35	39
42	65
32	48
74	85
26	46
32	NA
p value = 0.59	

Table 10: the table above contains the total vessel densities on a per animal basis for both treated and control.

3.3.5.3.1 Statistical Analysis for the Total Vessel Density

A two tailed heteroskedastic t test was performed based on the premise that the total vessel density could increase or decrease after radiotherapy. This produced the p value shown in the table above.

3.3.5.4 Perfused Vessel Density

The table below presents the Perfused Vessel Density obtained on a per animal basis for each group of animals.

Perfused Vessel Density	
Treated	Control
90	10
163	18
45	148
22	32
29	15
140	157
91	50
36	73
145	53
10	NA
p value = 0.56	

Table 11: the above table contains the perfused vessel density of a per animal basis.

3.3.5.4.1 Statistical Analysis for the Perfused Vessel Density

A two tailed heteroskedastic t test was performed based on the premise that the perfused vessel density could increase or decrease after radiotherapy. This produced the p value shown in the table above.

3.3.6 Discussion

Radiotherapy remains an effective anti-cancer treatment for a variety of disease types when used in combination with chemotherapy (chemoradiation) or in isolation. There is significant interest in the application of imaging biomarkers, such as ADC, for monitoring treatment efficacy and tumour response. Investigators have sought to explain the underlying driver of ADC changes post radiotherapy. There is a significant variability among the results obtained, with correlations between ADC and necrosis, ADC and apoptosis and a temporal dependence of these relations [106]. There is a dose dependency in the increases in ADC [109], which can be related to in vitro studies reporting increases in cell kill dependent upon the dose received. The results of this study indicate that the post radiotherapy increases in ADC can in part be explained by a high percentage necrosis at 72 hours. A fictitious threshold was introduced to explore any possible causal link between elevated ADC values and histopathological measures of necrosis, apoptosis, total vessel density and perfused vessel density. Our results suggest that there is no clear causal link between ADC rise and the percentage necrosis, significant variability in the data remains unexplained.

The fictitious threshold method is predicated upon the assumption that elevated ADC values on a voxelwise basis result from a high percentage necrosis. A large tumour with a high percentage necrosis will weight the percentile threshold more than a small tumour with intermediate necrosis, a potential source of bias. The growth of a solid tumour is associated with the development of a necrotic core as rapidly dividing cells outstrip their vascular network and develop regions of hypoxia and necrosis. The threshold method may not enable an accurate delineation between radiation induced necrosis and that resulting from solid tumour growth. The threshold applied to the representative animal data indicate that voxels with ADC values above threshold are present at baseline in both treated and control. There does not appear to be a preference for any particular region of the tumour.

The treated animal at 72 hours displays an increase over the whole of the section in voxels exceeding the threshold value. As the radiation dose was delivered across the entire tumour volume one would anticipate changes throughout, not localised to one specific region. The difference in the interquartile range at 72 hours occurs without a significant difference in the change in interquartile range between groups, 1 hour post and 72 hours post treatment. This could indicate that ADC changes taking place within the control group due to necrosis and proliferation occur in conjunction with the increases in ADC for the treated group.

The results of the linear regression indicate that the a best fit is obtained with necrosis as a single explanatory variable. The R^2 (0.37) indicates that there is significant variability in the data which requires explanation. Such

variability is unlikely to be entirely due to physiologic variation or noise. Cell proliferation is a non-linear process, the relationship between a percentage ADC and any histological measure is unlikely to be linear. Performing a non-linear regression may offer an improved explanation of the relationship between ADC above threshold and histology. Studies citing apoptosis as the dominant mechanism of cell death and ADC increase in a similar colorectal carcinoma model suffer from the confound of failing to report a percentage necrosis from H&E [110]. The lack of a baseline ADC measurement pre radiotherapy represents a possible confound. The experimental hypothesis was that radiotherapy would induce ADC increases on a voxelwise basis. A baseline ADC measurement would be expected to possess a lower mean ADC compared to 1 hour post treatment, if acute effects of radiotherapy are present. A comparison between baseline ADC values and those obtained at 72 hours can be postulated to produce a greater disparity, than that present between 1 and 72 hours post treatment.

Tumour response to radiotherapy has shown a sensitivity to radiation induced endothelial cell apoptosis [95]. The results obtained for CD31 and Hoechst 3342 don't provide evidence for such a relationship, at the dose and time period selected in this study. This study indicates that ADC increases occur in tissue sections with a high percentage necrosis at 72 hours. There does not appear to be any evidence that apoptosis, total vessel density or perfused vessel density influence the observed ADC values. The means of quantitating the percentages necrosis and apoptosis may explain some of the differences in histological results observed. Further validation work is required to enable a complete understanding of the ADC changes post radiotherapy.

4. The Effect of 5-FU Chemotherapy upon the Apparent Diffusion Coefficient in a Preclinical Cancer Model

4.1 Introduction

The mechanism of action of 5-FU (5-Fluorouracil) is through its metabolism to fluorodeoxyuridine monophosphate (FdUMP) and fluorouridine triphosphate (FUTP). FdUMP is an inhibitor of thymidylate synthase, an enzyme used to generate thymidine monophosphate (dTMP), a compound which is phosphorylated to thymidine triphosphate for use in DNA synthesis and repair [111]. Studies investigating the relationship between treatment with 5-FU, ADC and cell death in preclinical models have indicated that rises in ADC occur in response to treatment [77]. The aim of this study was to investigate the relationship between ADC changes pre and post chemotherapy with histopathological measures of cell death in a preclinical model of colorectal carcinoma (LoVo cell line).

4.1.1 Experimental Hypothesis

The experimental hypothesis was that the net ADC value computed over a tumour volume would increase after treatment with 50mg/kg of chemotherapy.

4.2 Materials and Methods

4.2.1 Study Design

Animal studies were performed in compliance with the NCRI Guidelines for the welfare and use of animals in cancer research and UK Animals (Scientific Procedures) Act after local Ethical Committee review. Tumour xenografts were initiated from LoVo colorectal tumour cells (5×10^6 per mouse) implanted in female nu/nu CBA mice aged 10 weeks old. When tumours reached 300-400 mm³ in size, mice were randomised to a control group (sham; n=6 saline) or to treatment (5-FU 50mg/kg in DMSO ip; n=6 for chemotherapy).

4.2.2 Imaging Acquisition and Analysis

Imaging was performed at 1 hour pre and 72 hours post chemotherapy on a 7T Bruker scanner with a volume transceiver coil. Diffusion-weighted imaging (spin-echo sequence; TR/TE =2250/20ms; b values 150, 500 and 1000

s/mm² ($\Delta = 9\text{ms}$ and $\delta = 4.5\text{ms}$); 15 contiguous slices of 6mm thickness; matrix 128 x 128 and FOV 2.56cm x 2.56cm) was performed after localisation with a T₂-weighted anatomical sequence. Voxel-wise values of ADC were calculated in *Matlab* (Mathworks) across the tumour using a least squares fitting algorithm and assuming Rician noise. Mean ADC was computed for both time points.

4.2.3 Animal Monitoring and Setup

Animals were kept at a constant temperature throughout the imaging session through the use of a heated water bed. The respiration rate was monitored through use of an electronic respiratory monitor.

4.2.4 Histological Analysis

At the conclusion of imaging animals were euthanised and the tumours rapidly excised and snap frozen in liquid nitrogen. The 5 μm sections for histological analysis were prepared using a cryostat. Necrosis was estimated by H&E staining sections and the degree of apoptosis using a fluorometric terminal transferase dUTP nick end labelling (TUNEL) assay that detects DNA degradation in apoptotic cells (DeadEndTM, Promega). Percentages of necrosis and apoptosis were determined by analysis of the stained sections as detailed previously.

4.2.5 Statistical Analysis

Changes in tumour volume and tumour volume at 1 hour pre and 72 hours post chemotherapy were compared by a two tailed, paired Student's t test. ADC at 1 hour pre and 72 hours post chemotherapy were compared between the two groups with an unpaired heteroskedastic one tailed Student's t test. This test was also used to compare absolute ADC changes in the two groups and % Necrosis and % Apoptosis at 72 hours. The change in ADC was plotted against percentage necrosis and apoptosis for both groups, with a Pearson's rho performed to test for significance. Statistical analysis was performed in *Matlab*.

4.3 Results

4.3.1 ADC Results

The changes in ADC observed on a per animal basis in both the treated and control groups is illustrated in the table below for all animals.

Control Group			Treated Group		
ADC baseline	ADC 72 hours	Delta ADC	ADC baseline	ADC 72 hours	Delta ADC
0.626	0.647	0.02	0.624	0.535	-0.090
0.646	0.603	-0.043	0.627	0.549	-0.078
0.600	0.602	0.003	0.641	0.563	-0.078
0.650	0.650	0.0003	0.607	0.584	-0.023
0.667	0.648	-0.019	0.681	0.603	-0.078
0.701	0.658	-0.043	0.632	0.608	-0.024

Table 12: the mean ADC values and changes on a per animal basis at 1 hour pre and 72 hours post chemotherapy.

4.3.1.1 Summary Table of Results

Parameter		Sham (n=6)	Treated (n=6)	<i>p</i> value
Volume (mm ³)	1 hr	317 ± 84	431 ± 83	0.03
	72 hr	577 ± 148	482 ± 95	0.16
	Change 1-72 hr	261 ± 127	52 ± 70	0.004
Mean ADC ± SD (mm ² s ⁻¹)	1 hr	0.65 ± 0.035	0.64 ± 0.025	0.23
	72 hr	0.63 ± 0.025	0.57 ± 0.03	0.001
	Change 1-72 hr	-0.01 ± 0.026	-0.06 ± 0.03	0.007
Haematoxylin and Eosin (% necrosis)		14.5 ± 9.98	11.75 ± 7.75	0.3
TUNEL (% apoptosis)		15.25 ± 9.32	12 ± 9.1	0.28

Table 13: the above table summarises the changes in tumour volume, ADC and histology observed on a per animal basis.

4.3.1.2 ADC Maps

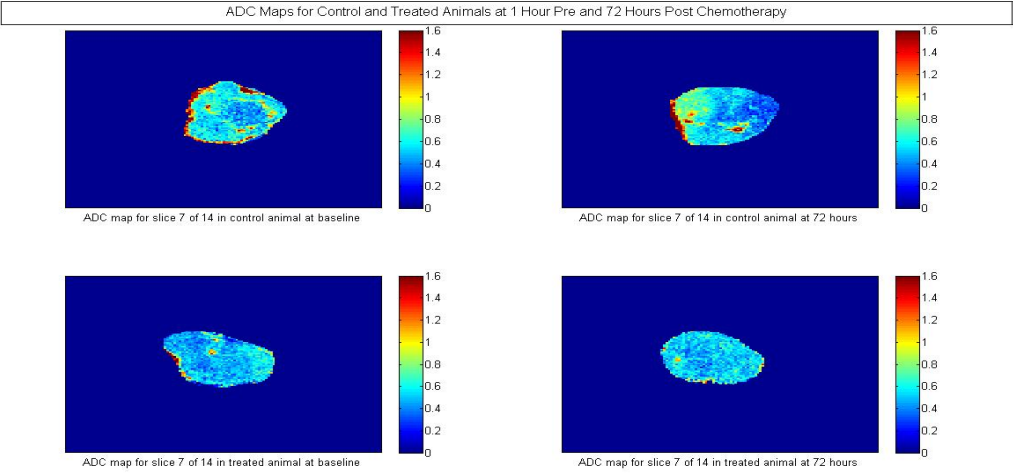


Figure 47: the ADC maps obtained for representative animals in both control and treated groups is shown above.

4.3.2 Histological Results

4.3.2.1 Percentage Necrosis

The table below presents the percentage necrosis for both control and treated groups.

% Necrosis	
Control	Treated
6	11
25	7
28	5.5
12.6	26.7
3.4	12.3
12	8
p value = 0.30	

Table 14: the table above contains the % necrosis obtained in both treated and control groups.

4.3.2.1.1 Statistical Analysis for the Percentage Necrosis

A one tailed heteroskedastic t test was performed based on the premise that the % necrosis would increase after chemotherapy. This produced the p value shown in the table above.

4.3.2.2 Percentage Apoptosis

The table below presents the percentage apoptosis obtained on a per animal basis for each group of animals.

% Apoptosis	
Control	Treated
8.6	6.4
28.4	21
22.2	11.6
19	25
4.8	4.3
8.5	3.7
p value = 0.28	

Table 15: the table above contains the results obtained for the % apoptosis between treated and control groups.

4.3.2.2.1 Statistical Analysis for the Percentage Apoptosis

A one tailed heteroskedastic t test was performed based on the premise that the % apoptosis would increase after chemotherapy. This produced the p value shown in the table above.

4.3.3 Statistical Results

The change in ADC between 1 and 72 hours was compared by means of a one tailed heteroskedastic Student's t-test.

This test was predicated upon the assumption that the percentage necrosis or apoptosis would increase in response to the chemotherapy. The change in ADC observed in each group was also compared by a one tailed heteroskedastic Student's t test. The percentages necrosis and apoptosis were statistically compared predicated on the assumption that the percentage necrosis or apoptosis increases in response to chemotherapy. The tumour volume at 1 hour pre and 72 hours post chemotherapy and the change in tumour volume were compared between the two groups using a two tailed paired Student's t test. This was predicated on the assumption that the tumour volume could increase or decrease in response to chemotherapy. These results are summarised in table 13. The Pearson's rho produced p values and correlation coefficients as shown in the table below.

Group	Variables	p value	Correlation Coefficient
Control	Δ ADC vs % Necrosis	0.70	-0.20
	Δ ADC vs % Apoptosis	0.77	-0.16
Treated	Δ ADC vs % Necrosis	0.27	0.54
	Δ ADC vs % Apoptosis	0.64	0.25

Table 16: the above table summarised the results of a Pearson's rho test.

4.4 Discussion

The preclinical literature indicates that 5-FU treatment induces increases in the ADC across the whole tumour volume [77]. The increases in ADC post chemotherapy have been attributed to necrosis in a number of studies [112], although 5-FU treated tumours have been shown to exhibit histological swelling, but no necrosis. The dependence of the ADC upon physiologic variables is in evidence from the results above. The administration of DMSO to the treated group represents a significant confound in the experimental method, resulting in decreases in ADC in all animals due to chronic dehydration. The lack of correlation between ADC and histology indicates that neither necrosis nor apoptosis drive the observed ADC changes. Confounding physiologic variables induced by either chemotherapy or other treatments will influence the ADC values observed within a patient population. Cancer treatment seldom involves one particular regimen but combinations.

The lack of any significant difference in histopathological measures between the two groups indicates that any possible relationship between ADC increases and percentage necrosis remains valid. The fictitious threshold was not applied to the above dataset as it is predicated upon the assumption that tumours with a high percentage necrosis also have elevated ADC values. A flaw in the method is that it does not validate histology or ADC values, it constrains ADC and necrosis into a linear relationship. The application of this method to the 5-FU dataset would require increases in ADC at 72 hours and % necrosis, as is not evident from the results. Any applied threshold and regression analysis would not offer additional scientific value.

The high ADC values in evidence at the corners of the control ADC map at 1 hour pre and 72 hours post treatment appear to indicate the presence of oedema. The sensitivity of ADC to oedema and lack of any histological method for validation represents a significant confound in the interpretation of ADC values. Investigators have examined T_2 as a means of assessing oedema, although this method is not fully validated. The results of this study are contrary to those encountered in the literature plausibly due to the administration of DMSO to the control group. These data also suggest that decreases in ADC occur concurrently with tumour growth as has been indicated in previous studies. Treatment with 50 mg/kg of 5-FU and 10Gy of radiotherapy (each administered as a single dose) results in cell death, with evidence supporting both apoptosis and necrosis as viable cell death pathways for each treatment.

The sensitivity of TUNEL to double stranded breaks in DNA results in similar areas of a tumour section staining positive for both techniques. The difference in absolute percentages could be due to the methods, drawing an ROI in an eosin stained portion of the section compared to summing over the TUNEL positive cells. The methods used

may differ between different imaging centres, providing additional variability to the results. Improvement upon the above method could be achieved through absolute cell counting across all sections using both H&E and TUNEL. The results above indicate that ADC requires further preclinical validation until a complete understanding of the complex interaction between cell death, oedema, interstitial pressure and perfusion is made.

5. Future Work

5.1 Mapping of the B_1 field

Offsets in the transmitted B_1 field from an RF coil will result in the magnetisation vector being flipped below or above the desired angle. A transmitted field which varies spatially throughout the sample will result in an inhomogeneous flip angle profile. There are a number of possibilities which exist to map the B_1 field [113], [114]. For the SPGR sequence (FLASH) used in dynamic studies the VAFI sequence (variable flip angle actual flip angle imaging) would enable simultaneous measurement of T_1 and the flip angle produced by the B_1 field. The VAFI method appears robust to the short T_1 values one would anticipate to be encountered in a dynamic study after administration of contrast agent. The application of AFI for short T_1 values appears to suffer from an error greater than 2.5 degrees for large flip angles. The development of a sequence for mapping of the B_1 field will improve the accuracy of T_1 measurements made using the FLASH sequence.

5.2 Probabilistic Model for DCE-MRI data analysis

The probabilistic methodology involves measuring the distribution of the contrast agent and water proton spins in terms of a probability distribution. This method reconciles shutter speed effects, errors propagated through response functions and confounds associated with the temporal and spatial resolution available in MRI experiments.

6. Bibliography

- [1] R. Damadian, K. Zaner, D. Hor, T. DiMaio, L. Minkoff, and M. Goldsmith, "Nuclear magnetic resonance as a new tool in cancer research: human tumors by NMR," *Ann N Y Acad Sci*, vol. 222, pp. 1048–1076, 1973.
- [2] P. G. Braunschweiger, L. M. Schiffer, and P. Furmanski, "1H-NMR relaxation times and water compartmentalization in experimental tumor models," *Magn Reson Imaging*, vol. 4, no. 4. pp. 335–342, 1986.
- [3] P. G. Braunschweiger, K. Reynolds, T. R. Nelson, and E. Maring, "The effect of dexamethasone on tissue water distribution and proton relaxation in Panc02 tumors," *Magn Reson Imaging*, vol. 5, no. 6. pp. 483–492, 1987.
- [4] C. F. Hazlewood, D. C. Chang, B. L. Nichols, and D. E. Woessner, "Nuclear magnetic resonance transverse relaxation times of water protons in skeletal muscle," *Biophys.J*, vol. 14, no. 8. pp. 583–606, 1974.
- [5] P. G. Braunschweiger, L. Schiffer, and P. Furmanski, "The measurement of extracellular water volumes in tissues by gadolinium modification of 1H-NMR spin lattice (T1) relaxation," *Magn Reson Imaging*, vol. 4, no. 4. pp. 285–291, 1986.
- [6] P. S. Tofts, "Modeling tracer kinetics in dynamic Gd-DTPA MR imaging," *J Magn Reson Imaging*, vol. 7, no. 1. pp. 91–101, 1997.
- [7] E. B. Schelbert, S. M. Testa, C. G. Meier, W. J. Ceyrolles, J. E. Levenson, A. J. Blair, P. Kellman, B. L. Jones, D. R. Ludwig, D. Schwartzman, S. G. Shroff, and T. C. Wong, "Myocardial extravascular extracellular volume fraction measurement by gadolinium cardiovascular magnetic resonance in humans: slow infusion versus bolus1," *J Cardiovasc.Magn Reson*, vol. 13. pp. 13–16, 2011.
- [8] C. H. Sotak, "Nuclear magnetic resonance (NMR) measurement of the apparent diffusion coefficient (ADC) of tissue water and its relationship to cell volume changes in pathological states," *Neurochem Int*, vol. 45, no. 4. pp. 569–582, 2004.

- [9] A. Szafer, J. Zhong, and J. C. Gore, "Theoretical model for water diffusion in tissues," *Magn Reson Med*, vol. 33, no. 5. pp. 697–712, 2005.
- [10] S. J. Mills, C. Soh, C. J. Rose, S. Cheung, S. Zhao, G. J. Parker, and A. Jackson, "Candidate biomarkers of extravascular extracellular space: a direct comparison of apparent diffusion coefficient and dynamic contrast-enhanced MR imaging--derived measurement of the volume of the extravascular extracellular space in glioblastoma multiform," *AJNR Am J Neuroradiol*, vol. 31, no. 3. pp. 549–553, 2009.
- [11] K. Bruynseels, N. Gillis, H. P. Van, and F. Vanstapel, "Phosphonates as ^{31}P -NMR markers of extra- and intracellular space and pH in perfused rat liver," *NMR Biomed*, vol. 10, no. 6. pp. 263–270, 1997.
- [12] M. J. Fisher and P. F. Dillon, "Phenylphosphonate: a ^{31}P -NMR indicator of extracellular pH and volume in the isolated perfused rabbit bladder," *Circ.Res*, vol. 60, no. 4. pp. 472–477, 1987.
- [13] D. Kanduc, A. Mittelman, R. Serpico, E. Sinigaglia, A. A. Sinha, C. Natale, R. Santacroce, M. G. Di Corcia, A. Lucchese, L. Dini, P. Pani, S. Santacroce, S. Simone, R. Bucci, and E. Farber, "Cell death: apoptosis versus necrosis (review)," *Int J Oncol*, vol. 21, no. 1. pp. 165–170, 2002.
- [14] G. J. Cannon and J. A. Swanson, "The macrophage capacity for phagocytosis," *J Cell Sci*, vol. 101 (Pt 4. pp. 907–913, 1992.
- [15] J. S. Taylor and W. E. Reddick, "Evolution from empirical dynamic contrast-enhanced magnetic resonance imaging to pharmacokinetic MRI," *Adv Drug Deliv Rev*, vol. 41, no. 1. pp. 91–110, 2000.
- [16] L. R. Arlinghaus, X. Li, A. R. Rahman, E. B. Welch, L. Xu, J. C. Gore, and T. E. Yankeelov, "On the relationship between the apparent diffusion coefficient and extravascular extracellular volume fraction in human breast cancer," *Magn Reson Imaging*, vol. 29, no. 5, pp. 630–638, 2011.
- [17] G. Majno and I. Joris, "Apoptosis, oncosis, and necrosis. An overview of cell death," *Am J Pathol.*, vol. 146, no. 1. pp. 3–15, 1995.

- [18] W. E. Mesker, J. M. Junggeburgt, K. Szuhai, H. P. De, H. Morreau, H. J. Tanke, and R. A. Tollenaar, "The carcinoma-stromal ratio of colon carcinoma is an independent factor for survival compared to lymph node status and tumor stage," *Cell Oncol*, vol. 29, no. 5. pp. 387–398, 2007.
- [19] P. J. Koelink, C. F. Sier, D. W. Hommes, C. B. Lamers, and H. W. Verspaget, "Clinical significance of stromal apoptosis in colorectal cancer," *Br J Cancer*, vol. 101, no. 5. pp. 765–773, 2009.
- [20] T. Aoyagi, K. Shuto, S. Okazumi, K. Hayano, A. Satoh, H. Saitoh, H. Shimada, Y. Nabeya, T. Kazama, and H. Matsubara, "Apparent diffusion coefficient correlation with oesophageal tumour stroma and angiogenesis," *Eur Radiol*, vol. 22, no. 6. pp. 1172–1177, 2012.
- [21] H. Jarvelainen, A. Sainio, M. Koulu, T. N. Wight, and R. Penttinen, "Extracellular matrix molecules: potential targets in pharmacotherapy," *Pharmacol Rev*, vol. 61, no. 2. pp. 198–223, 2009.
- [22] R. O. Hynes, "The extracellular matrix: not just pretty fibrils," *Science*, vol. 326, no. 5957. pp. 1216–1219, 2009.
- [23] D. E. Birk and R. L. Trelstad, "Extracellular compartments in matrix morphogenesis: collagen fibril, bundle, and lamellar formation by corneal fibroblasts," *J Cell Biol*, vol. 99, no. 6. pp. 2024–2033, 1984.
- [24] J. Zamecnik, L. Vargova, A. Homola, R. Kodet, and E. Sykova, "Extracellular matrix glycoproteins and diffusion barriers in human astrocytic tumours," *Neuropathol.Appl.Neurobiol.*, vol. 30, no. 4. pp. 338–350, 2004.
- [25] F. G. Ottaviano, D. E. Handy, and J. Loscalzo, "Redox regulation in the extracellular environment," *Circ.J*, vol. 72, no. 1. pp. 1–16, 2008.
- [26] M. J. Trotter, D. J. Chaplin, R. E. Durand, and P. L. Olive, "The use of fluorescent probes to identify regions of transient perfusion in murine tumors," *Int J Radiat.Oncol Biol Phys*, vol. 16, no. 4. pp. 931–934, 1989.

- [27] C. Burz, I. Berindan-Neagoe, O. Balacescu, and A. Irimie, "Apoptosis in cancer: key molecular signaling pathways and therapy targets," *Acta Oncol*, vol. 48, no. 6. pp. 811–821, 2009.
- [28] D. Hanahan and R. A. Weinberg, "Hallmarks of cancer: the next generation," *Cell*, vol. 144, no. 5. pp. 646–674, 2011.
- [29] K. Ohno, K. D. Pettigrew, and S. I. Rapoport, "Lower limits of cerebrovascular permeability to nonelectrolytes in the conscious rat.," *The American journal of physiology*, vol. 235, no. 3, pp. H299–307, Sep. 1978.
- [30] S. P. Sourbron and D. L. Buckley, "On the scope and interpretation of the Tofts models for DCE-MRI," *Magn Reson Med*, vol. 66, no. 3, pp. 735–745, 2011.
- [31] S. P. Sourbron and D. L. Buckley, "Tracer kinetic modelling in MRI: estimating perfusion and capillary permeability," *Phys Med Biol*, vol. 57, no. 2. pp. R1–33, 2011.
- [32] T. E. Yankeelov, W. D. Rooney, X. Li, and C. S. Springer Jr., "Variation of the relaxographic 'shutter-speed' for transcytolemmal water exchange affects the CR bolus-tracking curve shape," *Magn Reson Med*, vol. 50, no. 6. pp. 1151–1169, 2003.
- [33] S. S. Kety, "The theory and applications of the exchange of inert gas at the lungs and tissues," *Pharmacol Rev*, vol. 3, no. 1. pp. 1–41.
- [34] P. S. Tofts and A. G. Kermode, "Measurement of the blood-brain barrier permeability and leakage space using dynamic MR imaging. 1. Fundamental concepts," *Magn Reson Med*, vol. 17, no. 2. pp. 357–367.
- [35] S. Sourbron, M. Ingrisch, A. Siefert, M. Reiser, and K. Herrmann, "Quantification of cerebral blood flow, cerebral blood volume, and blood-brain-barrier leakage with DCE-MRI.," *Magnetic resonance in medicine* : official journal of the Society of Magnetic Resonance in Medicine / Society of Magnetic Resonance in Medicine, vol. 62, no. 1, pp. 205–17, Jul. 2009.

- [36] C. S. Patlak, R. G. Blasberg, and J. D. Fenstermacher, "Graphical evaluation of blood-to-brain transfer constants from multiple-time uptake data.," *Journal of cerebral blood flow and metabolism* : official journal of the International Society of Cerebral Blood Flow and Metabolism, vol. 3, no. 1, pp. 1–7, Mar. 1983.
- [37] C. S. Landis, X. Li, F. W. Telang, J. A. Coderre, P. L. Micca, W. D. Rooney, L. L. Latour, G. Vetek, I. Palyka, and C. S. Springer Jr., "Determination of the MRI contrast agent concentration time course in vivo following bolus injection: effect of equilibrium transcytolemmal water exchange," *Magn Reson Med*, vol. 44, no. 4. pp. 563–574.
- [38] G. Brix, F. Kiessling, R. Lucht, S. Darai, K. Wasser, S. Delorme, and J. Griebel, "Microcirculation and microvasculature in breast tumors: pharmacokinetic analysis of dynamic MR image series," *Magn Reson Med*, vol. 52, no. 2. pp. 420–429, 2004.
- [39] H. L. Cheng, "Investigation and optimization of parameter accuracy in dynamic contrast-enhanced MRI," *J Magn Reson Imaging*, vol. 28, no. 3. pp. 736–743, 2008.
- [40] A. Banerji, J. H. Naish, Y. Watson, G. C. Jayson, G. A. Buonaccorsi, and G. J. M. Parker, "DCE-MRI model selection for investigating disruption of microvascular function in livers with metastatic disease.," *J Magn Reson Imaging*, vol. 35, no. 1, pp. 196–203, Jan. 2012.
- [41] E. Porcel, S. Liehn, H. Remita, N. Usami, K. Kobayashi, Y. Furusawa, S. C. Le, and S. Lacombe, "Platinum nanoparticles: a promising material for future cancer therapy?," *Nanotechnology.*, vol. 21, no. 8. p. 085103, 2010.
- [42] M. Bruehlmeier, U. Roelcke, P. Blauenstein, J. Missimer, P. A. Schubiger, J. T. Locher, R. Pellikka, and S. M. Ametamey, "Measurement of the extracellular space in brain tumors using ⁷⁶Br-bromide and PET," *J Nucl Med*, vol. 44, no. 8. pp. 1210–1218, 2003.

- [43] V. Dedieu, F. Finat-Duclos, J. P. Renou, F. Joffre, and D. Vincensini, "In vivo tissue extracellular volume fraction measurement by dynamic spin-lattice MRI relaxometry: application to the characterization of muscle fiber types," *Invest Radiol*, vol. 34, no. 3. pp. 185–189, 1999.
- [44] J. H. Zdolsek, B. Lisander, and R. G. Hahn, "Measuring the size of the extracellular fluid space using bromide, iohexol, and sodium dilution," *Anesth. Analg.*, vol. 101, no. 6. pp. 1770–1777, 2005.
- [45] B. A. Graff, I. Bjornaes, and E. K. Rofstad, "Macromolecule uptake in human melanoma xenografts. relationships to blood supply, vascular density, microvessel permeability and extracellular volume fraction," *Eur J Cancer*, vol. 36, no. 11. pp. 1433–1440, 2000.
- [46] K. M. Donahue, D. Burstein, W. J. Manning, and M. L. Gray, "Studies of Gd-DTPA relaxivity and proton exchange rates in tissue," *Magn Reson Med*, vol. 32, no. 1. pp. 66–76, 1994.
- [47] T. E. Yankeelov and J. C. Gore, "Dynamic Contrast Enhanced Magnetic Resonance Imaging in Oncology: Theory, Data Acquisition, Analysis, and Examples," *Curr. Med Imaging Rev*, vol. 3, no. 2. pp. 91–107, 2009.
- [48] X. Fan and G. S. Karczmar, "A new approach to analysis of the impulse response function (IRF) in dynamic contrast-enhanced MRI (DCEMRI): a simulation study.," *Magn Reson Med*, vol. 62, no. 1, pp. 229–39, Jul. 2009.
- [49] F. Pain, P. Lanièce, R. Matrippolito, P. Gervais, P. Hantraye, and L. Besret, "Arterial input function measurement without blood sampling using a beta-microprobe in rats.," *Journal of nuclear medicine* : official publication, vol. 45, no. 9, pp. 1577–82, Sep. 2004.
- [50] E. Cheever, "The Convolution Integral," 2012. [Online]. Available: <http://lpsa.swarthmore.edu/Convolution/Convolution.html>.
- [51] A. Erik, "On the Problem of Identification in Compartment Analysis," *Modeling, Identification and Control*, vol. 1, no. 2, pp. 93–103, 1980.

- [52] W. Li, R. Scheidegger, Y. Wu, R. R. Edelman, M. Farley, N. Krishnan, D. Burstein, and P. V Prasad, "Delayed contrast-enhanced MRI of cartilage: comparison of nonionic and ionic contrast agents," *Magn Reson Med*, vol. 64, no. 5. pp. 1267–1273, 2010.
- [53] M. C. Schabel and D. L. Parker, "Uncertainty and bias in contrast concentration measurements using spoiled gradient echo pulse sequences," *Physics in medicine and biology*, vol. 53, no. 9, pp. 2345–73, May 2008.
- [54] J. S. Lowengrub, H. B. Frieboes, F. Jin, Y.-L. Chuang, X. Li, P. Macklin, S. M. Wise, and V. Cristini, "Nonlinear modelling of cancer: bridging the gap between cells and tumours," *Nonlinearity*, vol. 23, no. 1, pp. R1–R9, Jan. 2010.
- [55] X. Li, W. D. Rooney, and C. S. Springer Jr., "A unified magnetic resonance imaging pharmacokinetic theory: intravascular and extracellular contrast reagents," *Magn Reson Med*, vol. 54, no. 6. pp. 1351–1359, 2005.
- [56] T. E. Yankeelov, J. J. Luci, L. M. DeBusk, P. C. Lin, and J. C. Gore, "Incorporating the effects of transcytolemmal water exchange in a reference region model for DCE-MRI analysis: theory, simulations, and experimental results," *Magn Reson Med*, vol. 59, no. 2. pp. 326–335, 2008.
- [57] P. S. Tofts, G. Brix, D. L. Buckley, J. L. Evelhoch, E. Henderson, M. V Knopp, H. B. Larsson, T. Y. Lee, N. A. Mayr, G. J. Parker, R. E. Port, J. Taylor, and R. M. Weisskoff, "Estimating kinetic parameters from dynamic contrast-enhanced T(1)-weighted MRI of a diffusable tracer: standardized quantities and symbols," *J Magn Reson Imaging*, vol. 10, no. 3. pp. 223–232, 1999.
- [58] D. P. Barboriak, J. R. MacFall, B. L. Viglianti, and M. W. Whirst Dvm, "Comparison of three physiologically-based pharmacokinetic models for the prediction of contrast agent distribution measured by dynamic MR imaging," *J Magn Reson Imaging*, vol. 27, no. 6. pp. 1388–1398, 2008.

- [59] G. R. Moran and F. S. Prato, "Modeling (1H) exchange: an estimate of the error introduced in MRI by assuming the fast exchange limit in bolus tracking," *Magn Reson Med*, vol. 51, no. 4. pp. 816–827, 2004.
- [60] D. L. Buckley, "Uncertainty in the analysis of tracer kinetics using dynamic contrast-enhanced T1-weighted MRI," *Magn Reson Med*, vol. 47, no. 3. pp. 601–606, 2002.
- [61] X. Li, R. A. Priest, W. J. Woodward, F. Siddiqui, T. M. Beer, M. G. Garzotto, W. D. Rooney, and C. S. Springer Jr., "Cell membrane water exchange effects in prostate DCE-MRI," *J Magn Reson*, vol. 218. pp. 77–85, 2012.
- [62] T. S. Koh, S. Hartono, C. H. Thng, T. K. Lim, L. Martarello, and Q. S. Ng, "In vivo measurement of gadolinium diffusivity by dynamic contrast-enhanced MRI: A preclinical study of human xenografts," *Magn Reson Med*. pp. 269–276, 2012.
- [63] D. M. McGrath, D. P. Bradley, J. L. Tessier, T. Lacey, C. J. Taylor, and G. J. M. Parker, "Comparison of model-based arterial input functions for dynamic contrast-enhanced MRI in tumor bearing rats," *Magn Reson Med*, vol. 61, no. 5, pp. 1173–84, May 2009.
- [64] J. P. B. O'Connor, A. Jackson, G. J. M. Parker, C. Roberts, and G. C. Jayson, "Dynamic contrast-enhanced MRI in clinical trials of antivasular therapies," *Nature reviews. Clinical oncology*, vol. 9, no. 3, pp. 167–77, Mar. 2012.
- [65] D. L. Buckley, R. W. Kerslake, S. J. Blackband, and A. Horsman, "Quantitative analysis of multi-slice Gd-DTPA enhanced dynamic MR images using an automated simplex minimization procedure," *Magn Reson Med*, vol. 32, no. 5. pp. 646–651, 2005.
- [66] T. A. Egeland, K. Gulliksrud, J. V Gaustad, B. Mathiesen, and E. K. Rofstad, "Dynamic contrast-enhanced-MRI of tumor hypoxia," *Magn Reson Med*, vol. 67, no. 2, pp. 519–530, 2012.
- [67] M. Kopf, C. Corinth, O. Haferkamp, and T. F. Nonnenmacher, "Anomalous diffusion of water in biological tissues," *Biophys.J*, vol. 70, no. 6, pp. 2950–2958, 1996.

- [68] X. R. Li, L. Q. Cheng, M. Liu, Y. J. Zhang, J. D. Wang, A. L. Zhang, X. Song, J. Li, Y. Q. Zheng, and L. Liu, "DW-MRI ADC values can predict treatment response in patients with locally advanced breast cancer undergoing neoadjuvant chemotherapy," *Med Oncol*, vol. 29, no. 2, pp. 425–431, 2012.
- [69] H. Kobayashi and P. C. Lin, "Antiangiogenic and radiotherapy for cancer treatment," *Histol.Histopathol.*, vol. 21, no. 10, pp. 1125–1134, 2006.
- [70] E. C. Henning, C. Azuma, C. H. Sotak, and K. G. Helmer, "Multispectral tissue characterization in a RIF-1 tumor model: monitoring the ADC and T2 responses to single-dose radiotherapy. Part II," *Magn Reson Med*, vol. 57, no. 3, pp. 513–519, 2007.
- [71] E. C. Henning, C. Azuma, C. H. Sotak, and K. G. Helmer, "Multispectral quantification of tissue types in a RIF-1 tumor model with histological validation. Part I," *Magn Reson Med*, vol. 57, no. 3, pp. 501–512, 2007.
- [72] H. G. Goovaerts, T. J. Faes, G. W. de Valk-de Roo, M. ten Bolscher, J. C. Netelenbosch, W. J. van der Vijgh, and R. M. Heethaar, "Estimation of extracellular volume by a two-frequency measurement.," *Annals of the New York Academy of Sciences*, vol. 873, pp. 99–104, Apr. 1999.
- [73] M. Aref, M. Brechbiel, and E. C. Wiener, "Identifying tumor vascular permeability heterogeneity with magnetic resonance imaging contrast agents," *Invest Radiol*, vol. 37, no. 4, pp. 178–192, 2002.
- [74] C. Y. Tong, F. S. Prato, G. Wisenberg, T. Y. Lee, E. Carroll, D. Sandler, J. Wills, and D. Drost, "Measurement of the extraction efficiency and distribution volume for Gd-DTPA in normal and diseased canine myocardium," *Magnetic resonance in medicine* : official journal of the Society of Magnetic Resonance in Medicine / Society of Magnetic Resonance in Medicine, vol. 30, no. 3, pp. 337–46, Sep. 1993.
- [75] H. B. Larsson, S. Rosenbaum, and T. Fritz-Hansen, "Quantification of the effect of water exchange in dynamic contrast MRI perfusion measurements in the brain and heart," *Magn Reson Med*, vol. 46, no. 2, pp. 272–281, 2011.

- [76] J. E. Tanner, "Intracellular diffusion of water," *Arch. Biochem Biophys.*, vol. 224, no. 2, pp. 416–428, 1983.
- [77] B. A. Moffat, D. E. Hall, J. Stojanovska, P. J. McConville, J. B. Moody, T. L. Chenevert, A. Rehemtulla, and B. D. Ross, "Diffusion imaging for evaluation of tumor therapies in preclinical animal models," *MAGMA.*, vol. 17, no. 3–6, pp. 249–259, 2004.
- [78] P. S. Tofts, D. Lloyd, C. A. Clark, G. J. Barker, G. J. Parker, P. McConville, C. Baldock, and J. M. Pope, "Test liquids for quantitative MRI measurements of self-diffusion coefficient in vivo," *Magn Reson Med*, vol. 43, no. 3, pp. 368–374, 2000.
- [79] M. Holz, S. R. Heil, and A. Sacco, "Temperature-dependent self-diffusion coefficients of water and six selected molecular liquids for calibration in accurate ^1H NMR PFG measurements," *Journal of Chemical Physics*, vol. 2, no. 20, pp. 4740–4742, 2000.
- [80] T. L. Chenevert, C. J. Galban, M. K. Ivancevic, S. E. Rohrer, F. J. Londy, T. C. Kwee, C. R. Meyer, T. D. Johnson, A. Rehemtulla, and B. D. Ross, "Diffusion coefficient measurement using a temperature-controlled fluid for quality control in multicenter studies," *J Magn Reson Imaging*, vol. 34, no. 4, pp. 983–987, 2011.
- [81] R. M. Henkelman, "Measurement of signal intensities in the presence of noise in MR images," *Med Phys*, vol. 12, no. 2, pp. 232–233, 1985.
- [82] M. Ivancevic, C. Meyer, C. Galban, B. Hoff, T. Kwee, B. Ross, and T. Chenevert, "Simple, universal phantom for multi-center apparent diffusion coefficient (ADC) measurement," in *Proceedings 17th Scientific Meeting, International Society for Magnetic Resonance in Medicine*, 2009, vol. 7, p. 4166.
- [83] P. T. Callaghan, "Principles of Nuclear Magnetic Resonance Microscopy," in *Principles of Nuclear Magnetic Resonance Microscopy*, Oxford Science Publications, 1991, pp. 25–91.
- [84] L. Bains, "Assessing the effects of water exchange on contrast enhanced dynamic MRI." p. -, 2010.

- [85] I. L. Pykett, B. R. Rosen, F. S. Buonanno, and T. J. Brady, "Measurement of spin-lattice relaxation times in nuclear magnetic resonance imaging," *Phys Med Biol*, vol. 28, no. 6, pp. 723–729, 2000.
- [86] D. I. Hoult and N. S. Ginsberg, "The quantum origins of the free induction decay signal and spin noise," *J Magn Reson*, vol. 148, no. 1, pp. 182–199.
- [87] C. Burtea, S. Laurent, L. Vander Elst, and R. N. Muller, "Contrast agents: magnetic resonance," *Handb Exp Pharmacol*, no. 185 Pt 1, pp. 135–165, 2008.
- [88] N. Bloembergen and L. O. Morgan, "Proton Relaxation Times in Paramagnetic Solutions. Effects of Electron Spin Relaxation," *The Journal of Chemical Physics*, vol. 34, no. 3, p. 842, Mar. 1961.
- [89] J. A. Brookes, T. W. Redpath, F. J. Gilbert, G. Needham, and A. D. Murray, "Measurement of spin-lattice relaxation times with FLASH for dynamic MRI of the breast," *Br J Radiol*, vol. 69, no. 819, pp. 206–214, 1996.
- [90] R. R. Ernst, "Nobel Lecture. Nuclear magnetic resonance Fourier transform spectroscopy," *Biosci.Rep.*, vol. 12, no. 3, pp. 143–187, 1992.
- [91] J. M. Bland and D. G. Altman, "Statistical methods for assessing agreement between two methods of clinical measurement," *Lancet*, vol. 1, no. 8476, pp. 307–310, 1986.
- [92] T. R. Nelson and S. M. Tung, "Temperature dependence of proton relaxation times in vitro.," *Magnetic resonance imaging*, vol. 5, no. 3, pp. 189–99, Jan. 1987.
- [93] K. E. Jarvis, A.L.Gray, and and R.S.Houk, "Handbook of Inductively Coupled Plasma Mass Spectrometry." p. -, 1992.
- [94] P. J. Haar, W. C. Broaddus, Z. J. Chen, P. P. Fatouros, G. T. Gillies, and F. D. Corwin, "Gd-DTPA T1 relaxivity in brain tissue obtained by convection-enhanced delivery, magnetic resonance imaging and emission spectroscopy," *Phys Med Biol*, vol. 55, no. 12, pp. 3451–3465, 2010.

- [95] M. Garcia-Barros, F. Paris, C. Cordon-Cardo, D. Lyden, S. Rafii, A. Haimovitz-Friedman, Z. Fuks, and R. Kolesnick, "Tumor response to radiotherapy regulated by endothelial cell apoptosis," *Science*, vol. 300, no. 5622, pp. 1155–1159, 2003.
- [96] B. D. Ross, Y. J. Zhao, E. R. Neal, L. D. Stegman, M. Ercolani, O. Ben-Yoseph, and T. L. Chenevert, "Contributions of cell kill and posttreatment tumor growth rates to the repopulation of intracerebral 9L tumors after chemotherapy: an MRI study," *Proc Natl Acad Sci U S A*, vol. 95, no. 12, pp. 7012–7017, 1998.
- [97] T. L. Chenevert, P. E. McKeever, and B. D. Ross, "Monitoring early response of experimental brain tumors to therapy using diffusion magnetic resonance imaging," *Clin Cancer Res*, vol. 3, no. 9, pp. 1457–1466, 1997.
- [98] F. Peeters, D. Rommel, J. Barca-Quinones, V. Gregoire, and T. Duprez, "Early (72-Hour) detection of radiotherapy-induced changes in an experimental tumor model using diffusion-weighted imaging, diffusion tensor imaging, and Q-space imaging parameters: A comparative study," *J Magn Reson Imaging*, vol. 35, no. 2, pp. 409–417, 2012.
- [99] V. N. Harry, S. I. Semple, F. J. Gilbert, and D. E. Parkin, "Diffusion-weighted magnetic resonance imaging in the early detection of response to chemoradiation in cervical cancer," *Gynecol.Oncol*, vol. 111, no. 2, pp. 213–220, 2008.
- [100] S. Kim, L. Loevner, H. Quon, E. Sherman, G. Weinstein, A. Kilger, and H. Poptani, "Diffusion-weighted magnetic resonance imaging for predicting and detecting early response to chemoradiation therapy of squamous cell carcinomas of the head and neck," *Clin Cancer Res*, vol. 15, no. 3, pp. 986–994, 2009.
- [101] S. Kim, L. A. Loevner, H. Quon, A. Kilger, E. Sherman, G. Weinstein, A. Chalian, and H. Poptani, "Prediction of response to chemoradiation therapy in squamous cell carcinomas of the head and neck using dynamic contrast-enhanced MR imaging," *AJNR Am J Neuroradiol*, vol. 31, no. 2, pp. 262–268, 2010.

- [102] P. Wachsberger, R. Burd, A. Ryan, C. Daskalakis, and A. P. Dicker, "Combination of vandetanib, radiotherapy, and irinotecan in the LoVo human colorectal cancer xenograft model," *Int J Radiat.Oncol Biol Phys*, vol. 75, no. 3, pp. 854–861, 2009.
- [103] A. Leibovitz, J. C. Stinson, W. B. McCombs III, C. E. McCoy, K. C. Mazur, and N. D. Mabry, "Classification of human colorectal adenocarcinoma cell lines," *Cancer Res*, vol. 36, no. 12, pp. 4562–4569, 1976.
- [104] D. L. Trainer, T. Kline, F. L. McCabe, L. F. Faucette, J. Feild, M. Chaikin, M. Anzano, D. Rieman, S. Hoffstein, D. J. Li, and ., "Biological characterization and oncogene expression in human colorectal carcinoma cell lines," *Int J Cancer*, vol. 41, no. 2, pp. 287–296, 1988.
- [105] K. J. Williams, B. A. Telfer, I. J. Stratford, and S. R. Wedge, "ZD1839 ('Iressa'), a specific oral epidermal growth factor receptor-tyrosine kinase inhibitor, potentiates radiotherapy in a human colorectal cancer xenograft model," *Br J Cancer*, vol. 86, no. 7, pp. 1157–1161, 2002.
- [106] W. Ceelen, P. Smeets, W. Backes, D. N. Van, T. Boterberg, P. Demetter, I. Bouckennooghe, V. M. De, M. Peeters, and P. Pattyn, "Noninvasive monitoring of radiotherapy-induced microvascular changes using dynamic contrast enhanced magnetic resonance imaging (DCE-MRI) in a colorectal tumor model," *Int J Radiat.Oncol Biol Phys*, vol. 64, no. 4, pp. 1188–1196, 2006.
- [107] P. Workman, E. O. Aboagye, F. Balkwill, A. Balmain, G. Bruder, D. J. Chaplin, J. A. Double, J. Everitt, D. A. Farningham, M. J. Glennie, L. R. Kelland, V. Robinson, I. J. Stratford, G. M. Tozer, S. Watson, S. R. Wedge, and S. A. Eccles, "Guidelines for the welfare and use of animals in cancer research," *Br J Cancer*, vol. 102, no. 11, pp. 1555–1577, 2010.
- [108] A. R. Padhani, G. Liu, D. M. Koh, T. L. Chenevert, H. C. Thoeny, T. Takahara, A. Dzik-Jurasz, B. D. Ross, M. Van Cauteren, D. Collins, D. A. Hammoud, G. J. Rustin, B. Taouli, and P. L. Choyke, "Diffusion-weighted magnetic resonance imaging as a cancer biomarker: consensus and recommendations," *Neoplasia*, vol. 11, no. 2, pp. 102–125, 2009.

- [109] M. P. Larocque, A. Syme, A. Yahya, K. Wachowicz, J. Lalunis-Turner, and B. G. Fallone, "Monitoring T2 and ADC at 9.4 T following fractionated external beam radiation therapy in a mouse model," *Phys Med Biol*, vol. 55, no. 5, pp. 1381–1393, 2010.
- [110] X. Y. Zhang, Y. S. Sun, L. Tang, W. C. Xue, and X. P. Zhang, "Correlation of diffusion-weighted imaging data with apoptotic and proliferation indexes in CT26 colorectal tumor homografts in balb/c mouse," *J Magn Reson Imaging*, vol. 33, no. 5, pp. 1171–1176, 2011.
- [111] D. B. Longley, D. P. Harkin, and P. G. Johnston, "5-fluorouracil: mechanisms of action and clinical strategies," *Nature reviews. Cancer*, vol. 3, no. 5, pp. 330–8, May 2003.
- [112] T. Seierstad, S. Folkvord, K. Roe, K. Flatmark, A. Skretting, and D. R. Olsen, "Early changes in apparent diffusion coefficient predict the quantitative antitumoral activity of capecitabine, oxaliplatin, and irradiation in HT29 xenografts in athymic nude mice," *Neoplasia*, vol. 9, no. 5, pp. 392–400, 2007.
- [113] V. L. Yarnykh, "Actual flip-angle imaging in the pulsed steady state: a method for rapid three-dimensional mapping of the transmitted radiofrequency field," *Magn Reson Med*, vol. 57, no. 1, pp. 192–200, 2007.
- [114] V. L. Yarnykh, "Optimal radiofrequency and gradient spoiling for improved accuracy of T1 and B1 measurements using fast steady-state techniques," *Magn Reson Med*, vol. 63, no. 6, pp. 1610–1626, 2010.